Time-Series Spectroscopy of Pulsating Stars

Ivan Karim Baldry

A thesis
submitted for the degree of
Doctor of Philosophy
at the
University of Sydney

25th March 1999

Declaration of Originality

This thesis contains no material which has been presented for a degree at this or any other university and, to the best of my knowledge and belief, contains no copy or paraphrase of work published by another person, except where duly acknowledged in the text.

Note that Chapters 4–7 are written in the third person, because they are based on MNRAS papers produced in collaboration with other astronomers (Baldry et al. 1997, 1998b, 1998c, 1999). Nevertheless, they are a valid part of my thesis because the majority of the work can be credited as my own. The division of work is explained at the beginning of each of these chapters.

Ivan K. Baldry

Summary

Time-series spectroscopy of pulsating stars

The study of pulsating stars adds an extra dimension to stellar astrophysics. In addition to intensity measurements of a stellar spectrum, pulsational variations of a spectrum can be studied. These variations can be described by frequencies, amplitudes and phases of oscillations in various quantities derived from the spectrum. The frequencies of acoustic oscillations depend on the sound speed throughout the star, while the amplitudes depend on the excitation and damping processes. For spectroscopy, the observable quantities include Doppler shifts, equivalent widths and profile measurements of spectral lines. The variations of these observables are mainly related to velocity and temperature changes in the atmosphere of the star. In this thesis, spectral variations of the Cepheid ℓ Car and two rapidly oscillating Ap stars (roAp stars), α Cir and HR 3831, are analysed.

CCD non-linearity

For the roAp star spectra, the signal-to-noise ratios were sufficiently high that it was worth making a non-linearity correction to the CCD data. Non-linearity measurements of two CCDs at Mt. Stromlo Observatory are presented.

A ratio method is developed which involves measuring the intensity ratio between two regions on the CCD (after bias correction), using a flat-field lamp for illumination. In order to determine the non-linearity, the ratio is measured for exposures of varying length. For a linear CCD, the measured ratio should be the same for all exposures. This method can provide an accurate non-linearity curve because it is unaffected by uncertainties in the exposure time, and it is less affected by changes in the lamp's flux than for other methods.

ℓ Carinae

ℓ Car is a Cepheid with a pulsation period of 35.5 days. The variation of the Hα profile is presented, using 33 high-resolution echelle spectra obtained between February 1994 and April 1995.

A weak Hα emission feature is present at nearly all phases, which is unusual for classical Cepheids. This emission appears both redward and blueward of the absorption feature at different phases. The origin of the emission feature may be a shock front or may be the upper atmosphere of the star.

α Circini

α Cir is an roAp star with one dominant pulsation period of around 6.8 minutes. Over 6000 spectra of the wavelength region 6000–7000Å were obtained, from dual-site observations with medium-dispersion spectrographs during two weeks in May 1996. Several different measurements are presented, including velocities of different spectral lines and line-profile measurements of the Hα line.

The velocity amplitude and phase of the principal pulsation mode vary significantly, depending on which line is being measured. The amplitude is observed to be as high as $1000\,\mathrm{m\,s^{-1}}$ in some wavelength bands, despite a previous upper limit of $36\,\mathrm{m\,s^{-1}}$. Furthermore, some lines are apparently pulsating in anti-phase with others. This may indicate a high-overtone standing wave with a velocity node in the atmosphere of the star.

Additionally, the bisector-velocity amplitude and phase vary significantly, depending on the height in the Hα line, including a phase reversal between the core and the wings of the line. This supports the theory of a radial pulsational node in the atmosphere of the star. Blending with metal lines partially affects the Hα bisector results but probably not enough to explain the phase reversal.

Changes in the equivalent-width of the line during the pulsation, and the oscillatory signal as a function of wavelength across the Hα region, are also presented.

HR 3831 (IM Velorum)

HR 3831 is an roAp star with a pulsation period of around 11.7 minutes. 1400 medium-resolution spectra of the wavelength region 6100–7100Å were obtained, during one week in March 1997. Similar measurements to those made on α Cir are presented.

The Hα velocity amplitude of HR 3831 is modulated with rotation phase. Such a modulation was predicted by the oblique pulsator model, and rules out the spotted pulsator model. However, further analysis of the Hα line and other spectral lines suggests that there are rotational modulations which cannot easily be explained using the oblique pulsator model.

The variation of the Hα bisector shows a very similar pattern to that observed in α Cir. This argues against the radial node interpretation since HR 3831 has a longer period and therefore the pulsation is expected to have a longer vertical wavelength in the atmosphere of the star, unless the structure of the atmosphere is somewhat different between the two stars. Alternatively, the bisector variation is a signature of the degree ℓ of the mode and not the overtone value n.

High-resolution studies of the metal lines in roAp stars are needed to understand fully the form of the pulsation in the atmosphere.

Acknowledgements

First and foremost, I would like to thank my parents, Mum and Dad, Liz and Allan, for always supporting me in my education and my interest in astronomy.

Before coming to Sydney, I studied at King's College in Cambridge for four years and worked at the Isaac Newton Group on La Palma over two summers. I am grateful to all who helped me at these institutions, in particular, to those who provided the references for my PhD application, Chris Gilligan at King's and Mike Breare at the ING. Oh and how could I forget to mention Ju, Stu, Mark, Gez and Sam for plenty of moral support.

During my PhD, I was part of the Chatterton Astronomy Department in the School of Physics at the University of Sydney. I am very grateful to Tim Bedding for being a jolly good supervisor and to John Davis for giving me the opportunity to do a PhD. I would also like to thank Andrew Booth, Siou-Gek Chew, Sonia Cianci, David Dawes, Andrew Jacob, Andreas Kelz, Alberto Mendez, Anna Moore, Melinda Taylor, Erik Thorvaldson and the rest of the Astronomy Department. Other people in the School of Physics have also been helpful throughout the course of my thesis: Lawrence Cram, Gene Davidson, Bryan Gaensler, Tanya Hill, Alex Merchant and many others.

The observations for my thesis were obtained at Mt. Stromlo Observatory. I am very grateful to Mike Bessell and other staff at MSO for their help and advice.

During 1996, I spent three months at the Institut for Physik og Astronomi, University of Aarhus. This really kick-started my PhD, working closely with Jörgen Christensen-Dalsgaard, Sören Frandsen, Hans Kjeldsen and Michael Viskum. Hans has effectively been my co-supervisor. After these three months, in October 1996, I went to the conference in Nice on 'Sounding Solar and Stellar Interiors'. Here, I met some of the experts on roAp and Ap stars. In particular, I would like to thank Jaymie Matthews, Thebe Medupe, Don Kurtz and Friedrich Kupka for many discussions.

That covers nearly everyone, but there are some other people that I would like to thank: my relatives in Perth for accommodation and support when I arrived in Oz in 1995; Wendy Page and her family for the same when I arrived in Sydney; Felicity Baldry, Michael Barnes, Tracy Bryan, Andrew Harrison, Stefan Keller, Glenn Mitchell, Eileen O'Hely, Stefanie Sander, Eliza Skinner, Kelly Tsoi and other friends in Sydney; bushwalking, climbing and squash club members for recreation.

Thanks to all those co-authors who contributed to producing my first publication, a song about the Winter ASA (Baldry et al. 1996). Admittedly, I wrote none of the lines and only gave moral support but, because of alphabetical order, I get to be first author. I mention it here because this is the only chance that I'll get to cite it.

Financial assistance was obtained from the Australian Postgraduate Award, Australian Research Council and the Danish Natural Science Research Council.

Contents

List of Figures

List of Tables

Chapter 1

Pulsating stars

1.1 Introduction

Pulsating stars: vibrating, oscillating, resonating — or, for a more official definition, "pulsating variables are stars showing periodic expansion and contraction of their surface layers" (General Catalogue of Variable Stars, GCVS). They also change temperature and luminosity in a periodic or quasi-periodic way. This is not an unusual phenomenon amongst stars, and known types of pulsating stars cover a large range of stellar masses and ages. It is possible that all stars are oscillating or pulsating to some extent but that most have amplitudes that are too low to detect with present technology. For instance, the Sun has oscillations with periods around five minutes and with very small amplitudes, which are only detectable because of our proximity. However, when astronomers use the term *pulsating stars*, they are usually referring to stars where the oscillations are driven by a feedback mechanism within the star[1]. In these stars, one or more oscillation modes are intrinsically unstable (self-excited), and the star is observed as being singly- or multi-periodic. Known pulsation periods range from about one minute in some white dwarfs up to about five years in some supergiants.

The observational challenges of studying pulsating stars involve answering the question: in what way is the spectrum or radiation from a star changing? In particular, what are the frequencies and amplitudes of the vibrations, and how are the amplitudes and phases of different measurements (e.g., magnitudes, Doppler shifts) related to each other? The theoretical challenges involve answering the question: how and why is a star pulsating? In particular, what are the temperature, velocity and density changes during the pulsation, as a function of position in the star, and what causes the star to oscillate (pulsation mechanism)?

Apart from being interesting astrophysical objects in their own right, pulsating stars are of importance to other fields, for example: (i) stellar atmospheres and interiors, (ii) stellar evolution, (iii) the distance scale. The next three paragraphs briefly describe some aspects of these cases.

In the first case, the frequencies of acoustic oscillations are related to the sound-speeds within a star, and measuring these frequencies provides an excellent test of stellar models. For this purpose, it is important to determine the type of mode for each observed frequency. Modelling atmospheres and interiors is closely related to modelling pulsations, since knowledge of the temperature and density structure within a star is essential to understanding causes and effects of the pulsation.

In the second case, evolution, oscillation frequencies can be measured more accurately than any other stellar property (radius, luminosity, etc.), and therefore it is possible to: (a) accurately define evolutionary states, ages and masses within a class of pulsating stars, and (b) measure changes in some stars over time periods of years. For example, a few pulsating white dwarfs have been observed to change very slightly in period over several years (Sullivan 1998). This is possibly due to changes in the oscillation frequencies of a white dwarf as it cools over an evolutionary time scale.

[1] Under this definition, the Sun and other stars, with similar low-amplitude oscillations, are not included since their oscillations are excited randomly by convection.

In the third case, the distance scale, many classes of pulsating stars have a relationship between their period and luminosity. Generally the bigger and brighter a star is, within a class, the longer the pulsation period. The best known case is for classical Cepheids, where there is a close period-luminosity relationship. Therefore, in order to estimate a Cepheid's absolute luminosity, it is only necessary to measure its period. Then, by measuring the star's apparent luminosity, an estimate of the distance to the star can be obtained. Using the Hubble telescope, the distance can be obtained to Cepheids up to 20 Megaparsecs away, which provides a major step in the extra-galactic distance scale.

In the rest of this chapter, I give a broad picture of pulsating stars, in terms of different types of oscillation modes (asteroseismology) and different types of stars. The following chapters (2–3) give some technical details of observing, data reduction and CCD non-linearity.

In the chapters presenting the scientific results of this thesis (4–7), I quantitatively analyse the spectral changes in three pulsating stars: the long-period Cepheid ℓ Carinae and two rapidly oscillating Ap stars (roAp stars), α Circini and IM Velorum (better known as HR 3831), mainly looking at changes around the Balmer line Hα. Qualitative analysis is given for the form of the pulsation in the atmospheres of the stars.

1.2 Asteroseismology

The study of the oscillation modes in multi-periodic stars is called asteroseismology. In this section, the classification of the different types of modes is explained.

All stars have eigenmodes with associated frequencies at which they can vibrate (analogous to the modes on the membrane of a drum). The surface variation of these modes can be closely described using spherical harmonic functions, $Y_{\ell m}$, which are well known from the quantum mechanical description of the hydrogen atom. Modes with $\ell = 0$ are radial (because the motion is entirely in the radial direction), and with $\ell \geq 1$ are non-radial. The frequencies of modes with the same 'angular degree' ℓ can be split by rotation into $2\ell + 1$ different frequencies, with the 'azimuthal order' m taking values between $-\ell$ and $+\ell$. The ℓ value is equal to the number of nodal lines on the surface, with $|m|$ indicating how many nodal lines pass through the poles of some axis[2] of physical symmetry in the star. Additionally, there is a quantum number n which is the overtone value of the pulsation. The 'radial order' n is equal to the number of nodes on a radial line between the surface and the centre of the star (called *radial nodes* in this thesis).

The eigenmodes of a star are often divided into p, f and g modes. For p-modes, the restoring force is gas and radiation pressure. These are basically standing sound waves within the star, for which the frequency of the oscillations increases with increasing overtone. The g-modes vibrate at lower frequencies and the restoring forces are gravity and buoyancy force. These have mostly horizontal motions and the frequency decreases with increasing overtone. There are only non-radial g-modes. The intermediate f-modes or fundamentals have no nodes in the radial direction ($n = 0$), and are generally considered

[2]Usually the rotation axis, but in the case of roAp stars the magnetic axis is the relevant axis in the oblique pulsator model.

to be the lowest frequency p-modes. The $\ell = n = 0$ mode is the fundamental radial mode seen, for example, in classical Cepheids. Note that the fundamental dipole mode ($\ell = 1$, $n = 0$) is forbidden because it violates conservation of momentum.

The roAp stars pulsate in high-overtone p-modes. For these mode frequencies ($n \gg \ell$), there is a useful 'asymptotic theory' approximation to the frequencies (Christensen-Dalsgaard 1988; Brown & Gilliland 1994):

$$\nu_{n,\ell} \simeq \Delta\nu_0(n + \ell/2 + \epsilon) - \ell(\ell+1)D_0 + ..., \tag{1.1}$$

where $\Delta\nu_0$, ϵ and D_0 are constants which depend on the structure of the star. Modes with the same degree ℓ but different n are separated in frequency by multiples of $\Delta\nu_0$, which is called the 'large separation'. This parameter is related to the sound travel time through the star and, using the virial theorem, it can be shown that it is simply related to the mean density of the star (Brown & Gilliland 1994):

$$\nu_{n,\ell} - \nu_{n-1,l} \simeq \Delta\nu_0 \approx 135\sqrt{\frac{M/M_\odot}{(R/R_\odot)^3}}\,\mu\mathrm{Hz}. \tag{1.2}$$

This equation is expected to hold for stars of various masses along the main-sequence. There is also a relationship between the frequencies of modes differing by two in degree, which can be written as:

$$\delta\nu_{n\ell} = \nu_{n,\ell} - \nu_{n-1,\ell+2} \approx (4\ell+6)D_0. \tag{1.3}$$

$\delta\nu$ is called the 'small separation' and is about a factor of ten smaller than the large separation (Christensen-Dalsgaard 1988), between modes of $\ell = 0$ and 2. This parameter is related to the sound-speed in the core and is therefore sensitive to the age of the star because, as hydrogen burns to form helium, the sound-speed in the core changes.

Modes with $\ell \leq 3$ are of the most significance to observational asteroseismology, since modes with higher ℓ values are extremely hard to detect in integrated light or velocity. This is because observed light variations are an integral over the surface of the star, and high-degree modes have many phase changes across a stellar hemisphere.

Considering high-overtone p-modes obeying the asymptotic theory: (a) if $\ell = 0$ and 1 modes are observed in star, then the oscillation spectrum[3] would consist of peaks at roughly equally spaced frequencies separated by $\Delta\nu_0/2$, (b) if $\ell = 0$–3 modes are observed, then the oscillation spectrum would be similar except doublets would be present in place of single peaks. The oscillation spectrum can be further complicated by rotational splitting.

Many roAp stars have modes that are separated in frequency by multiples of $\Delta\nu_0/2$, because they pulsate in high-overtones with possibly $\ell = 1$ and 2 modes observed. A good example is the roAp star HR 1217 which has five equally-spaced modes, of which, four are rotationally split into triplets (Kurtz et al. 1989). α Cir has five known modes

[3]An 'oscillation spectrum' is a Fourier transform of the light or spectral variations in a star. It can be shown as an 'amplitude spectrum' or a 'power spectrum' (amplitude or amplitude squared versus frequency, respectively).

in the range 2250–2600 μHz, with one showing rotational splitting. Kurtz et al. (1994b) inferred a large separation of 50 μHz from the fact that the frequency spacings between the modes were all nearly integer multiples of 25 μHz.

1.3 Classification

There are many types of pulsating star and more types being discovered every decade. In this section, I briefly describe some of the classifications which are divided into three general groups in terms of their position in the H-R diagram: (i) stars evolved significantly above the zero-age main-sequence (ZAMS), which all pulsate radially in fundamental or low-overtone p-modes; (ii) stars on or near the main-sequence; (iii) stars evolved below the ZAMS.

Figure 1.1 shows the locations of some of these pulsating stars in the H-R diagram diagram (provided by J. Christensen-Dalsgaard). The shading is related to the excitation and the type of modes; (a) horizontal shading indicates stochastically excited p-modes, (b) NW-SE shading (like Cepheids) indicates self-excited (predominately) p-modes, (c) SW-NE shading (like DAV) indicates self-excited g-modes.

The zero-age main-sequence is represented by a single *dashed-line*, while the Cepheid-instability strip is confined by *parallel dashed-lines*. The evolution of various mass stars from the main-sequence to the giant and supergiant phases are represented by *solid lines* (initial masses of 1, 2, 3, 4, 7, 12 and 20 solar masses). After the red-giant phase, some low-mass stars (initial $M \lesssim 2M_{\odot}$) go through a stable phase of evolution where the star becomes condensed and blue. These stars form a 'horizontal branch' in the H-R diagram represented by the *dash-and-dotted line*. In the final stages of evolution, intermediate- and low-mass stars (initial $M \lesssim 7M_{\odot}$) shed most of their outer layers leaving a core, which firstly contracts and heats-up forming a pre-white dwarf (surrounded by a planetary nebula), before cooling to become a white dwarf. These stages are represented by the *dotted line*[4].

For the stars analysed in this thesis, their positions ($\log T_{\rm eff}, \log L/L_{\odot}$) in the H-R diagram are about: (3.7,4.2) for the classical Cepheid ℓ Car (mean position); (3.90,1.06) for the roAp star α Cir; and (3.90,1.13) for the roAp star HR 3831.

Several references were used to obtain the information on the pulsating stars described below. The general references were: (a) for classifications: Feast (1992), Becker (1998) and the GCVS (Kholopov et al. 1998); (b) for details on each class of pulsating stars: recent conference proceedings (Stobie & Whitelock 1995; Provost & Schmider 1997; Bradley & Guzik 1998; Deubner et al. 1998), review articles (Brown & Gilliland 1994; Gautschy & Saio 1995, 1996) and an astronomy encyclopedia (Marin 1992); (c) for periods of the white-dwarf and pre-white-dwarf stars: data tables by Bradley (1995).

Note that in these descriptions: (a) low-overtone modes have n less than about 5, and high-overtone modes have n greater than about 20; (b) all amplitudes quoted are full-range amplitudes.

[4]No star is actually seen crossing from the giant region to the planetary nebulae nuclei (PNN) region. When a giant star expands enough, the core shows through — there are no intermediate stages.

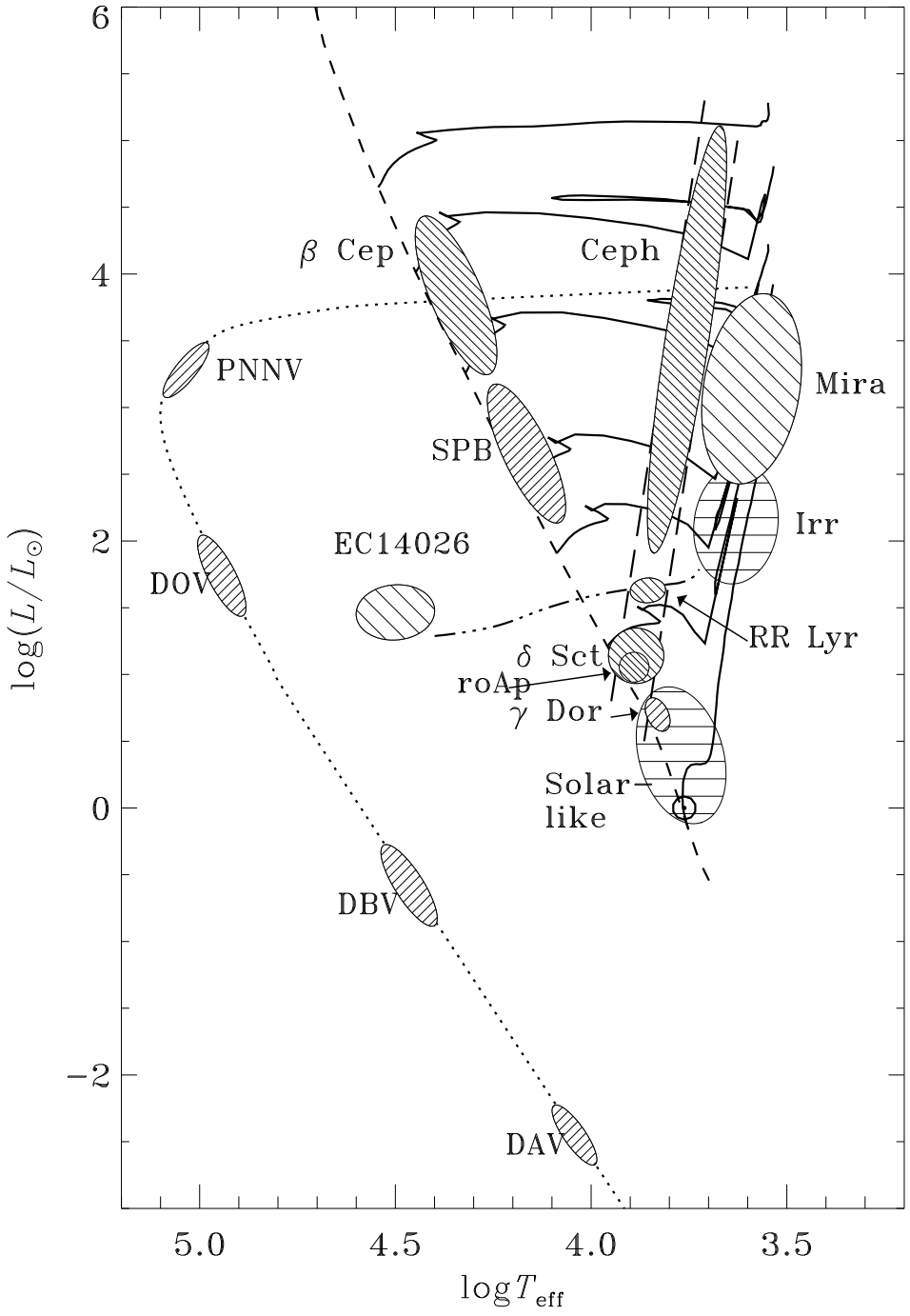

Figure 1.1 Schematic H-R diagram showing the location of several classes of pulsating stars, provided courtesy of Jørgen Christensen-Dalsgaard (private communication). The shading is related to the excitation and the type of modes, while the lines represent various evolutionary tracks and states. See text for details.

Group I: above the main-sequence, radial p-modes

- Miras — periods: 80–1000 days
  — Miras are pulsating red-giant stars with large amplitudes. They are 10 to 4000 times brighter in visible light at maximum than at minimum (amplitude 2.5–9 mag in V), and show considerable irregularity in the amplitude and shape of the light curve. There is some dispute as to whether they pulsate primarily in their fundamental or first overtone (Wood 1995), and there is evidence that some Miras switch between different modes on time scales of decades (Bedding et al. 1998).
- Irregular (Irr) and semi-regular (SR) variables — periods: 20–2000 days
  — These are similar to Miras but with poorly defined periods and generally lower amplitudes (< 2.5 mag in V). The term long-period variable (LPV) is often used to cover all pulsating red giants and supergiants (Whitelock 1990).
- Cepheids (δ Cephei stars) — periods: 1–70 days
  — Cepheids are pulsating yellow supergiants with luminosities 500 to 30 000 times larger than that of the Sun, but with similar effective temperatures. The light amplitudes are typically between 0.5 and 2 magnitudes. The classical Cepheids pulsate in the fundamental radial mode and have a close period-luminosity relationship, which has given them an important role in determining the distance to nearby galaxies. Other Cepheids pulsate in their first overtone, or simultaneously in their fundamental and first overtone (beat Cepheids).
- Type II Cepheids (RV Tau stars, W Vir stars, BL Her stars) — periods: 0.8–150 days
  — These are pulsating variables of the old spherical component (halo) of the galaxy. They are similar to classical Cepheids and they also obey a period-luminosity relationship. For a similar period, the Type II Cepheids are fainter by about 1–2 mag. They are often divided into three types based on their period; RV Tau ($P > 30$ d), W Vir (intermediate period) and BL Her ($P < 8$ d) stars.
- R Coronae Borealis (RCB) stars [5] — periods: 30–100 days
  — RCB stars are hydrogen-poor and carbon-rich giants. Many have been observed to have Cepheid-like pulsations.
- RR Lyrae stars — periods: 0.2–0.9 days (5–22 hours)
  — RR Lyr stars are old low-mass ($M \sim 0.7 M_\odot$) giant stars, with A to F spectral type. They pulsate radially in their fundamental or first overtone modes, with amplitudes between 0.2 and 2 mag in V. In the H-R diagram, they are located just below the Cepheids in the 'Cepheid instability strip'.

Group II: on or near the main-sequence

- β Cephei stars (β Canis Majoris stars) — periods: 0.1–0.3 days (2.5–7 hours)
  — These are pulsating early-type-B stars, which are multi-periodic with amplitudes less than 0.3 mag in V. Pulsational variability is common amongst O and B stars, of

[5] In the GCVS, classified under *eruptive variable stars*.

which, the β Cep stars were the first to be discovered. In the β Cep domain, radial and non-radial, fundamental and low-overtone p- and g-modes are expected to be unstable (Moskalik 1995).

- Slowly pulsating B (SPB) stars (53 Per stars) — periods: 0.5–4 days (12–96 hours) — SPB stars are mid-type-B to late-type-B stars, with variability on time-scales of about a day. The multi-periodic nature of these variations means that they can only be understood in terms of pulsations (Waelkens 1996). In particular, they must pulsate in non-radial g-modes, because their periods are significantly longer than the expected periods for fundamental modes.
- δ Scuti stars — periods: 0.5–8 hours
  — δ Sct stars are mostly main-sequence and sub-giant stars, of spectral class A and early-type-F. They pulsate in many modes, with amplitudes less than 0.8 mag. As with the β Cep stars, radial and non-radial, p- and g-modes are excited. The high-amplitude (> 0.1 mag) δ Scuti stars comprise less than 10% of the class, and are usually sub-giant to giant stars. On the main-sequence, they generally have small amplitudes of around 0.02 mag (Breger 1979).
- Rapidly oscillating Ap (roAp) stars [6] — periods: 0.08–0.25 hours (5–15 minutes)
  — roAp stars are a sub-group of the chemically peculiar magnetic stars that pulsate in high-overtone p-modes (pulsating CP2 stars), with amplitudes less than 0.02 mag. They occupy approximately the same region of the H-R diagram as the main-sequence δ Sct stars, but pulsate in much higher overtones. This is probably due to their strong magnetic fields.
- γ Doradus stars — periods: 0.5–3 days (12–72 hours)
  — γ Dor stars are main-sequence early-type-F stars. For similar reasons to the SPB stars, their variability has been associated with non-radial g-modes. They are a new class of pulsating stars, discovered this decade (Balona et al. 1994).
- Solar-like oscillators — periods: 0.08–0.33 hours (5–20 minutes)
  — These stars, late-type-F to G, are expected to oscillate in a similar way to the Sun, in which, many p-modes are excited by stochastic convection across a range of periods with amplitudes below 5×10^{-5} mag. The highest amplitude modes have periods of about 5 minutes in the Sun, and are expected to have periods of around 20 minutes in the sub-giants. No solar-like oscillations have been confirmed in a star other than the Sun.

Group III.a: below the main-sequence

- EC14026 stars — periods: 1.5–8 minutes
  — These are pulsating hot sub-dwarf B (sdB) stars, on the 'horizontal branch' of the H-R diagram, which are multi-periodic. They form a new class, and to date about 12 stars have been confirmed as members. One EC14026 star has been observed to have an amplitude of about 0.3 mag with a period of 8 minutes, but most have

[6] In the GCVS, classified under *rotating variable stars*: "ACVO – Rapidly oscillating α^2 CVn variables".

amplitudes of around 0.02 mag with periods less than 3 minutes. These stars were theoretically predicted to be p-mode pulsators (Fontaine et al. 1998).

Group III.b: below the main-sequence, non-radial g-modes

- Planetary nebula nuclei variables (PNNV) — periods: 10–35 minutes
  — PNNV are pre-white-dwarf stars situated in the centre of planetary nebula, which are multi-periodic pulsators. They have been observed to pulsate with amplitudes of around 0.1 mag.
- DO-type variables (DOV), PG 1159 stars, GW Vir stars — periods: 5–15 minutes
  — DOV are pulsating pre-white-dwarf stars, similar to the PNNV, but without a surrounding nebula. The DOV and PNNV are located in the 'GW Vir instability strip', and many have temperatures greater than 100 000 K.
- DB-type variables (DBV) — periods: 2–18 minutes
  — DBV are multi-periodic pulsating white-dwarfs with Helium atmospheres and temperatures of around 22 000 K.
- DA-type variables (DAV), ZZ Ceti stars — periods: 1.5–20 minutes
  — DAV are multi-periodic pulsating white-dwarfs with Hydrogen atmospheres and temperatures of around 12 000 K.

Cepheids, RR Lyrae, δ Scuti and roAp stars are located in the instability strip (parallel dashed-lines). Additionally, the DAV white-dwarfs can be regarded as being located where an extension of the instability strip crosses the white-dwarf evolution track (dotted line). This suggests that these classes of stars have a similar pulsation mechanism (e.g, Cox 1980, Unno et al. 1989). For the well-studied Cepheids, this mechanism is related to the ionization zones of Hydrogen and Helium.

For a star to be unstable to pulsation in a particular mode (self-excited), there must be a driving force applied at the appropriate moment during the pulsation in order to overcome damping mechanisms. A simple analogy is a person pushing a swing: a push must be applied just after the swing reaches its highest point, for maximum effect. With an ionization mechanism, regions in the midstages of ionization of an abundant element are absorbing heat when they are most compressed. Therefore, maximum pressure in the relevant regions occurs after maximum compression and pulsations can be driven. For a Cepheid, these regions are in the outer stellar layers where the pulsation amplitude is high and the driving can outweigh the damping from the inner regions where the amplitude is low. However, we would normally expect damping from above the ionization zone to cancel the driving. In Cepheids, this is not the case because the ionization zone straddles the transition region between the quasi-adiabatic interior and non-adiabatic exterior, and the damping is reduced in the non-adiabatic exterior (see Cox 1980 for details). It is because of this condition, that the instability strip covers a narrow range of temperatures in the H-R diagram.

For the roAp stars, the pulsation mechanism is not well-known. It may be related to the He^+ ionization zone, but this is currently a matter of debate and ongoing research (e.g., Dziembowski & Goode 1996, Gautschy et al. 1998).

Chapter 2

Time-series spectroscopy

2.1 Introduction

Observational study of pulsating stars usually involves measuring variations in quantities, called 'observables', derived from the light emitted from a star. Such measurements are made using time-series spectroscopy, photometry or interferometry (a relatively new possibility). A time series can range from taking an exposure every ten seconds for an hour, in the case of photometry of a rapid oscillator, to one measurement every few months for several years, in the case of studying long-period variables.

Depending on the observable, the measured variation can be related to variations in one or more of the properties of the star: luminosity, radius, temperature, velocity ($v = \mathrm{d}R/\mathrm{d}t$ for radial pulsation), etc.; see Table 2.1 for examples. In general, these properties are not uniquely defined and will depend on the spectral region or line being measured. This is because the light from a star is emitted from a range of depths in its atmosphere. Additionally, in the case of non-radial pulsation, the variation of these properties will be a function of position on the surface.

For spectroscopy using a narrow slit ($\lesssim 2$ arcsec wide), absolute intensity measure-

Table 2.1 Observables for pulsating stars

observable	technique	properties
magnitude	photometry[a]	L, T
angular diameter	interferometry[b]	R
Doppler shift	spectroscopy	v
equivalent width	spectroscopy	T
line profile	spectroscopy	T, v

[a] Usually using Johnson or Strömgren filters.
[b] It is only recently becoming possible to measure directly radius changes of pulsating stars (Cepheids and Miras).

ments can not be made, because the total light entering the spectrograph will vary significantly between exposures as the projection of a star on the slit moves. Therefore, this type of spectroscopy is generally used to study absorption and emission lines in a star.

The most easily interpretable measurement is the Doppler shift of a line. Ignoring relativistic effects, the observed shift is an integral of the projected line-of-sight velocities across and through the observable atmosphere of a star. Therefore, the pulsational velocity of the surface away from the centre is usually larger than the measured pulsational Doppler shift[1] by a 'projection factor', which is about 1.4 for the radial pulsations in Cepheids (Albrow & Cottrell 1994). For non-radial pulsations, the situation is more complicated, the projection factor depends on the mode and the angle between the pulsation pole and the line of sight.

The equivalent-width (EW) of a line is a measure of the strength of absorption or emission relative to the continuum (the EW is positive for absorption, and negative for emission). If a spectrum (intensity versus wavelength) is normalised so that the continuum emission has an intensity of 1, then the EW is defined as $(1 - I) \times W$ where I is the mean intensity across a spectral region of width W that includes the line only. Changes in the EW of a line during pulsation are mainly related to temperature changes at the formation depth of the line, but can also depend on pressure and density changes.

A spectral line may change in a complicated way that can not easily be quantified by two parameters (Doppler shift and EW), for instance: (i) a line may be asymmetrical, in which case, the value of the Doppler shift will depend on how it is measured; or (ii) there may be emission and absorption components to a spectral line. In these cases and others, it becomes relevant to investigate changes in the line profile as a whole. Line profile changes can be quantified using bisector or intensity measurements, i.e., resolving the line vertically or horizontally. Alternatively, they can be qualitatively studied by plotting the line profile as a function of pulsation phase.

2.2 Observing

There are many techniques for observing pulsating stars using spectroscopy depending on the pulsation period, brightness, what properties are being studied, etc. To determine a suitable method, it is necessary to consider the science requirements in terms of: resolution; signal-to-noise; wavelength range; instrument stability; frequency and number of observations. In this section, the observations of the three stars analysed in this thesis are explained.

Most of the observations were taken using the coudé spectrograph[2] on the 74-inch (188-cm) Telescope at Mt. Stromlo. A Schmidt camera, with a focal length of 32 inch

[1] To obtain the pulsational Doppler shift, the centre-of-mass velocity and other non-pulsational line shifts must be removed from the measurements. Other line shifts can be caused, for example, by convection where the integral of the velocities is weighted towards rising gas in the convective regions and the observed line will appear blue-shifted, even though there may be no net-motion of the surface.

[2] The light enters the spectrograph through a slit mounted at the coudé focus (situated below the telescope). The light is then collimated, dispersed and refocused onto a detector.

(81 cm), focuses the spectrum onto a Tektronix CCD, which was about 5 x 5 cm in size with 2000 x 2000 pixels.

Mt. Stromlo is a good site for studying bright pulsating stars because it is a poor site! To explain this comment — it is a poor site in terms of light pollution (from Canberra), seeing and weather, which means that it is less subscribed by astronomers studying faint objects or by those needing good seeing or photometric conditions. Therefore, more time is available for astronomers doing spectroscopy of bright stars. This is good for studying pulsations because large blocks of time can be obtained for observing projects (two or more weeks), which is important: (a) for good frequency-resolution in the oscillation spectrum of rapidly oscillating stars, or (b) for good phase-coverage of pulsations in Cepheids. In other words, the length of observing time is of high importance and, while good conditions will obviously improve results, observing conditions are less critical than in other areas of astronomy. Also, at low altitude sites such as Mt. Stromlo, absorption lines from the Earth's atmosphere are stronger and more stable. This can actually be an advantage if these telluric lines are being used as a velocity reference (see Section 5.5.1).

For the study of the Hα line in ℓ Car (Chapter 4), the observations[3] were part of a project to determine accurately the radial velocity curves of a few Cepheids, e.g., ℓ Car (Taylor et al. 1997) and β Dor (Taylor & Booth 1998). Several sets of observations were made in 1994 and 1995 (see Table 4.1) with good phase coverage of the pulsation in ℓ Car ($P = 35.5$ d), the largest gap being 0.085 of a cycle (3 days). The main project requirements were high resolution and a large wavelength range that included Hα, Hβ and many metal lines for accurate velocity analysis. For this purpose, the echelle setup was used. The light was first dispersed by a cross disperser grating (158 grooves/mm) and then by the echelle grating (31.6 grooves/mm). About 45 orders (different wavelength regions) were projected on to the CCD, with a total wavelength coverage from about 4800Å to 6800Å. The dispersion was about 2.2Å/mm (0.05Å/pixel) at 6000Å with a resolution of about 2 pixels (0.1Å). To calibrate the wavelength range for each order and to remove instrumental shifts, several Thorium-Argon arc spectra were taken during each observing night.

For α Cir (Chapters 5–6), the observations were part of a dual-site campaign[4] (at Stromlo and La Silla) to study this star and a δ Scuti star FG Virginis. The Stromlo observations covered two weeks in May 1996, with observing concentrated on α Cir in the second week (see Table 5.1). The main requirements were high frequency of exposures, high signal-to-noise and a wavelength range that included Hα and the telluric lines around 6900Å (to be used as a velocity fiducial). For this purpose, the light was dispersed using a single reflection grating, the B-grating, which had 600 grooves/mm. The grating was used to project 1st-order spectra on to the CCD, giving a dispersion of 20 Å/mm (0.49Å/pixel). A slit width of about 0.5 mm was used, giving a resolution of about 3 pixels (1.5Å). The total wavelength coverage was from 6000Å to 7000Å.

The observing of a single order spectrum allowed a small part of the CCD to be read-

[3]The observations were done mainly by Melinda Taylor.

[4]Multi-site campaigns are often organised to study pulsating stars ($P \lesssim 1$ day), because this reduces 1/day aliases in the oscillation spectrum.

out, a window of 2000 x 40. This produced a fast read-out time of 17 seconds which was important in obtaining a high frequency of exposures. Due to the way the CCD reads out data, a window of 40 x 2000 had a significantly longer read-out time (about 55 seconds), therefore, at the start of this observing run the CCD was rotated by 90 degrees from its usual position. This rotation allowed almost twice as many exposures to be taken (one per 45 s compared to one per 83 s), because the exposures of α Cir were limited to 28 seconds (on average) to avoid saturating the CCD.

For HR 3831 (Chapter 7), a similar setup to α Cir was used, essentially to apply the same techniques to a different roAp star. The differences were: (a) a slightly higher wavelength coverage, 6100-7100Å; and (b) a wider CCD window, 2000 x 80, to improve scattered light subtraction, with the read-out time only increased by 3 s to 20 s. The exposure time was chosen to be 100 seconds, using the calculation described below.

2.2.1 Calculation of optimum integration time

In this section, I look at the optimum strategy for observing a pulsating star in terms of the integration time per exposure. In particular, I am considering the case where the expected pulsations are rapid enough that phase smearing becomes an issue. Phase smearing is the reduction in the measured amplitude due to the effect of integrating over a significant fraction of a pulsation cycle. This will typically be an issue for pulsation periods of less than an hour or so.

The aim is to maximise the signal-to-noise ratio in the amplitude spectrum of a time series covering a given total observing time (A typical amplitude spectrum is shown in Figure 5.4). The two factors that I am considering are:

(i) fraction of time spent integrating light from the star (duty-cycle),

(ii) reduction in amplitude of a sine-wave due to integration (phase smearing).

The principal assumption, in this calculation, is that the final noise level will be proportional to $\sqrt{1/D}$, where D is the duty-cycle. For instance, this will be the case for measurements that are dominated by photon noise.

The important variables are:

- I — integration time per exposure,
- P — period of oscillation,
- R — read-out time or over-head time between exposures.

The duty-cycle can be written as

$$D = \frac{I}{I+R} \,. \tag{2.1}$$

Consider a sine wave of frequency $\omega = 2\pi/P$ and amplitude A . We wish to determine how the measured amplitude (A_m) is reduced with integration time. $V_m(t)$ is the measured observable at a time t (mid-time of the exposure):

$$V_m(t) = \frac{1}{I}\int_{t-I/2}^{t+I/2} A\,\sin(\omega t')\,\mathrm{d}t' = \frac{A}{\omega I}[\,\cos(\omega(t-\frac{I}{2})) - \cos(\omega(t+\frac{I}{2}))\,] \,. \tag{2.2}$$

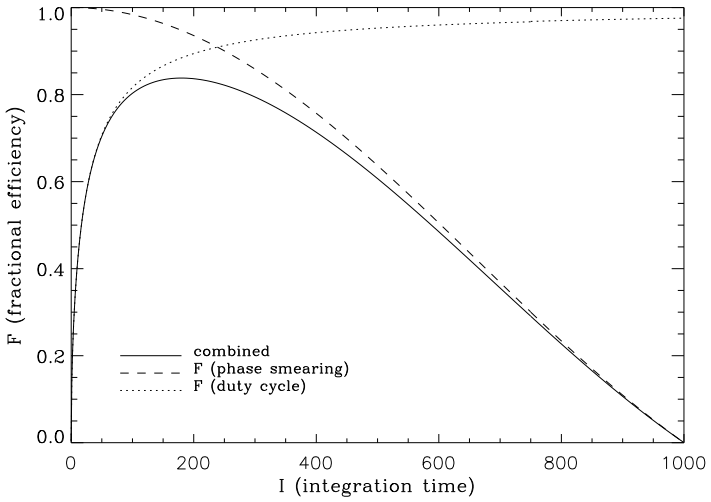

Figure 2.1 Efficiency of observing a star with a pulsation period of $P = 1000$ seconds and an over-head time between exposures of $R = 50$ seconds. The effects of phase smearing and duty cycle are shown separately and combined.

Using cosine identities, this can be simplified to

$$V_m(t) = \frac{2A}{\omega I} \sin\left(\frac{\omega I}{2}\right) \sin(\omega t) \,. \tag{2.3}$$

Setting $V_m = A_m \sin(\omega t)$, we have

$$A_m = \frac{\sin(x)}{x} A \,, \quad \text{where} \quad x = \frac{\omega I}{2} = \frac{\pi I}{P} \,. \tag{2.4}$$

This quantifies the effect of phase smearing. At the limit $I \to 0$ then $A_m = A$; and if $I = P$ then $A_m = 0$. The signal-to-noise ratio is proportional to $\sqrt{D} \times (A_m/A)$, which is the fraction F of the most efficient observing ($F = 1$ in the theoretical limit of $R = 0$ and $I \to 0$).

$$F = \sqrt{D}\frac{A_m}{A} = \sqrt{\frac{I}{I+R}} \frac{\sin(\pi I/P)}{(\pi I/P)} = \frac{P}{\pi\sqrt{I(I+R)}} \sin\left(\frac{\pi I}{P}\right) \,. \tag{2.5}$$

An example of F as a function of I is shown in Fig. 2.1 for a pulsation period of 1000 seconds with an over-head time between exposures of 50 seconds. The figure shows the effect of the two factors separately and combined. The combined curve is fairly flat at the top and integration times ranging from 100 to 250 seconds would give an F-value of greater than 0.8. Therefore there is plenty of room to vary I in consideration of other factors, while maintaining a good F-value in terms of this analysis. For instance, there may be other pulsation periods within the same star to consider. Fig. 2.2 shows the effect of changing the pulsation period on the F versus I curve, with R constant (20 seconds).

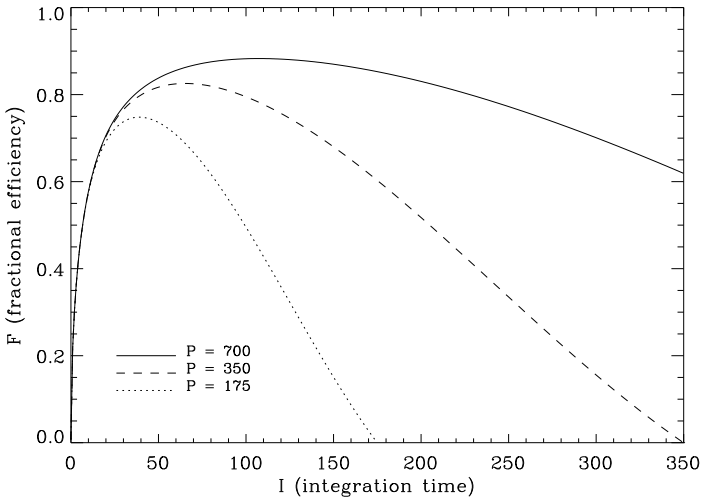

Figure 2.2 Efficiency of observing a star with several pulsation periods and an over-head time of $R = 20$ seconds. These periods are equal to the principal, 1st harmonic and 3rd harmonic pulsation periods in HR 3831.

I used this analysis to determine the optimum integration time for the observing run on HR 3831 during March 1997 (Section 7.2.1). I chose to use an integration time of 100 seconds which was close to the optimum time for detecting the principal frequency and which also gave a reasonable F-value for the first harmonic. Higher order harmonics were not considered, since I was mainly interested in determining the properties of the principal frequency.

For the observations of α Cir during May 1996 at Mt. Stromlo (Section 5.2), with the principal oscillation period of 410 seconds and an over-head time of 17 seconds, the optimum integration time was calculated to be 70 seconds. However, during this observing run, the integration time was limited by the digital saturation of the CCD. I varied the integration time between 20 and 45 seconds depending on the conditions (seeing and extinction), with the aim of maximising the duty-cycle without saturating any images.

In summary: for observations of a singly periodic star where the final noise level in the amplitude spectrum is expected to be approximately proportional to $\sqrt{1/D}$, the integration time should be chosen to maximise F according to Equation 2.5. If several pulsation periods *of equal interest* are being studied in a star, the F-value should be chosen for the shortest period because, in any case, it will be higher for longer periods. In consideration of other noise factors: if there is a noise level in the final analysis that is independent of the duty cycle, higher weight should be given to the effect of phase smearing and therefore the integration time should be lower. Conversely, if read-out noise is a significant factor, increasing the duty-cycle is more important and therefore the integration time should be higher.

Note that the above analysis was made by considering a fixed total observing time. The signal-to-noise ratio in the final amplitude spectrum can be increased by observing

for longer, as long as an oscillation remains coherent, i.e., with no significant phase jumps or frequency changes. The noise level in the amplitude spectrum will be, approximately, inversely proportional to the square-root of the total observing time.

2.3 Data reduction

CCDs consist of an array of pixels (typically 2000 x 2000 pixels). During an exposure, incident photons are stored as electrons in each pixel. After the exposure is finished, the CCD is read out, which means the charge in each pixel is converted to a digital number called analogue-to-digital units (ADU; usually a 16-bit integer 0–65535). In addition to the science spectral images, several calibration images are usually taken — these include: biases, flat-fields, dark images, arcs and standard stellar spectra. The initial reduction process involves converting the 2D science spectral images to 1D spectra (relative intensity vs. wavelength), using the calibration images to improve accuracy. The methods, as applied to the data analysed for this thesis, are briefly outlined in the results chapters (4–7). In this section, I describe in more detail some of these methods as a general guide [(i)–(vii) below].

The main software packages used were FIGARO, developed by Keith Shortridge, and IRAF, maintained by the National Optical Astronomy Observatories (NOAO). These packages have similar capabilities for analysing astronomical data.

(i) Bias subtraction — Every CCD digital image has a zero-point offset to the measured number of photons, which is called the bias (typically around 1000 ADU). The bias level can vary over the CCD (bias structure) and can vary from image to image. The reduction generally involves two stages: (a) subtraction of a bias frame, which is obtained by reading out the CCD without exposing it to light; and (b) adjustment to the zero level using over-scan regions of the image, which are regions that are not exposed to light during an exposure on the rest of the CCD. As with all images, the bias images will contain read-out noise. To avoid introducing unnecessary extra noise into the images of the spectra, ten or more bias images can be averaged to produce a low noise-level bias frame.

(ii) Non-linearity correction — For a linear CCD, the measured ADU counts (after bias subtraction) will be proportional to the number of incident photons. However, no CCD is perfectly linear, and in some cases, the accuracy of results can be significantly improved by making a non-linearity correction. This is the subject of Chapter 3.

(iii) Flat-field correction — The quantum efficiency, or probability of capturing photons, can vary from pixel to pixel on a CCD (typically by a few percent). This can be corrected by dividing the images of the spectra by a flat-field frame, which is made by processing images of the spectrum of a bright lamp that has no spectral-line features. The processing can involve bias subtraction, non-linearity correction, averaging and illumination correction.

Figure 2.3 A CCD image of an echelle spectrum

Any pixel-to-pixel variations in a flat-field image are due to intrinsic variations of the CCD, noise or illumination. The noise can be reduced by averaging many flat-field images, so that the percentage noise variations are significantly smaller than the percentage intrinsic variations. If the illumination of the lamp on the CCD is significantly different from the star light (along the dispersion direction), it may be necessary to remove illumination variation of the flat-field. This can be done by dividing by a smoothed version of the flat-field, in effect, leaving only the high-frequency intrinsic variations.

(iv) Cosmic ray removal — When a high-energy particle interacts with a CCD, a number of extra electrons are left in one or a few neighbouring pixels. These can be removed by comparing similar images, or by searching for and interpolating over spikes in an image. The easiest method, for biases and flat-fields in particular, is to take the median value (pixel by pixel) of three or more images. For spectral images, obvious spikes can be removed before or after extracting the spectra. With thousands of short exposures, as with the observations of α Cir and HR 3831, it is unnecessary to remove cosmic rays because each measurement has very little chance of being contaminated and bad data-points can be removed when the time-series analysis is applied.

(v) Tracing and extraction of spectrum — Spectra are projected onto two-dimensional images (Figure 2.3). One dimension represents the dispersion direction and the other represents the slit direction (the spread of light along the slit due to seeing or tracking). In the case of an echelle spectrum, several wavelength regions (called orders) are projected onto different parts of the CCD, the dispersion direction remains nearly the same and the different orders are separated from each other in the slit direction so that light from adjacent orders does not overlap. In reality, the dispersion direction is never exactly horizontal or vertical, and therefore, the first part of this

reduction is to trace the peak of the spread of star light (in the slit direction), along the dispersion axis. This must be done for each order, with typically a quadratic fit to the trace. The second part is to extract the order(s), by adding-up the counts in the slit direction within typically ten pixels of the centre of the trace at each point along the dispersion axis.

As well as star light dispersed onto the CCD, there will be scattered star light and background sky light. This extra light can be removed by measuring the light intensity on either side of the extracted spectrum (in-between the orders of an echelle spectrum), and then subtracting an appropriately scaled value. For example, 10 lines are added-up to determine the extracted spectrum and 20 lines to determine the scattered light, then 0.5 times the scattered light is subtracted from the spectrum. This process 'adds' photon and read-out noise to a spectrum but it is necessary if accurate relative intensity measurements are to be made, because the ratio between the scattered / background light intensity and the true spectral intensity can vary from exposure to exposure.

(vi) Continuum fitting — It is generally not possible to make absolute intensity measurements in medium- to high-resolution spectra because slit losses vary. Therefore, the continuum emission is usually taken as a reference level. The intensity and shape of this continuum level can vary from exposure to exposure. To overcome this, a fit can be made to continuum or near-continuum regions in order to normalise the continuum level to an intensity of 1.0 across the spectrum. Continuum fits with only a few parameters are more robust, while those with more parameters are potentially more accurate. When reducing thousands of spectra, as in the case of α Cir and HR 3831, robustness is important and typically a 2nd or 3rd degree polynomial is used. For a few spectra, the continuum fit can be checked and adjusted by eye and any type of fit can be tried to obtain high accuracy. In the case of spectra with many absorption lines, sometimes only a poor approximation can be made to the continuum level.

In the case of echelle orders, the shape of the continuum is noticeably curved due to the grating diffraction pattern. Therefore, it may better to correct for this illumination shape before applying a continuum fit. This can be done by dividing by a smoothed flat-field order or by a good fit to an order of a stellar spectrum which has few lines (for example, the spectrum of an early-type-B star).

(vii) Wavelength calibration — The orders, once extracted, will be in the form of intensity versus pixel-number. In order to calibrate the pixel-number in terms of wavelength, it is useful to take spectra of an arc lamp (e.g., a Th-Ar arc). The positions of the emission lines with known wavelengths are then identified, and a fit is made to the dispersion across the order. Typically, a quadratic fit is adequate.

For ℓ Car (Chapter 4), further reduction involved converting the wavelengths to heliocentric values and determining the pulsational phase for each observed spectrum.

For α Cir and HR 3831, more than a thousand spectra were observed in each case, and the changes from one spectrum to the next were too small to interpret by eye. Further

reduction consisted of measuring observables from each spectrum, and determining their oscillation amplitudes and phases through time-series analysis. These processes are described in detail in the results chapters (e.g., in Sections 5.3, 6.2, 7.3). For this specialised analysis, I wrote or modified programs in the commercial package IDL or in FORTRAN.

Chapter 3

Correcting for CCD non-linearities

3.1 Introduction

A charge coupled device (CCD) consists of an array of elements (pixels) arranged on a very thin silicon layer. Incident photons on each pixel are converted to electron-hole pairs. Up to 50 000–500 000 electrons can be stored in each pixel, depending on the CCD. After an exposure is finished, the electrons can be moved around and read-out by a controller which converts the electron charge in each pixel (or binned group of pixels) to digital counts (analogue-to-digital units or ADU). The conversion factor (electrons/ADU) is called the gain and is typically in the range 2–5.

CCDs are not perfectly linear systems as some people often assume. After bias subtraction, the number of ADU counts is not exactly proportional to the number of incident photons. The most probable reason for this non-linearity is that the controller gain is not a constant function of the number of electrons. When the CCD approaches saturation, there will be much larger non-linearities due to the reduced probability of capturing photons in nearly full pixels.

Correcting for non-linearities is important whenever a differential intensity measurement needs to be made. For example, measuring the equivalent width of lines in spectroscopic data or in most photometry. In general, non-linearities will be less important for Doppler shift measurements, except in the case of asymmetric line profiles where the measured wavelength displacement depends on the depth in the line.

3.1.1 Testing for non-linearities

To test for non-linearities, we need a fairly stable light source, for example either a lamp or clear daytime sky. There are two methods that I will discuss here, a bracketed repeat-exposure method (Section 4 from Gilliland et al. 1993) and a ratio method developed by myself.

The bracketed repeat-exposure (BRE) method involves making single and multiple exposures with the CCD. We do not change the exposure time as we cannot assume that the nominal exposure time is accurate, i.e., there may be an constant offset to any selected

exposure time. Instead, we keep the exposure time constant and make repeat exposures of the CCD before reading-out. A typical example of the method consists of several read-outs with the no. of repeats = 0,1,2,1,3,1,4,1,5,1,6,1,7,1,8,1,9,1,10,1,0. The first and last read-outs are bias frames and the single exposures (bracketing the multiple exposures) are used to calibrate the change in the lamp's intensity, i.e., to determine the expected counts for the multiple exposures. Only a small region of the CCD is read out, such that the read-out time is only a few seconds, while the exposure time should be about two seconds. It is then possible to plot a curve of relative gain[1] (measured-counts / expected-counts) versus measured-counts for various regions on the CCD (note that all counts are bias-corrected first). For a linear CCD, the gain should be constant. Each plot can be normalised to have the same value of relative gain at a certain number of measured counts.

The ratio method is an indirect method and, as the name suggests, involves calculating the ratio between the measured light level on two regions of the CCD. By varying the exposure time, we can then make a plot of the ratio versus measured-counts (of one of the regions). For a linear CCD, the ratio should be constant. This method is unaffected by uncertainties in the exposure time or in the light level, except in the case of spectra, where changes in the temperature of the lamp will affect the ratio between some regions. To avoid this problem, half of the length of the slit can be covered with a filter to create a light level difference at each wavelength. These ratio measurements can be used to test a non-linearity curve obtained by the BRE method. Another good test involves taking daytime spectra to determine how the equivalent width of lines changes for various light levels. This is similar to the ratio method in that the equivalent width is a measure of the mean depth of a line relative to the continuum. Taking daytime spectra is a good way of testing to see if a particular type of measurement depends significantly on non-linearities.

[1]This 'relative gain' is proportional to ADU/electrons (inverse to the normal definition of gain).

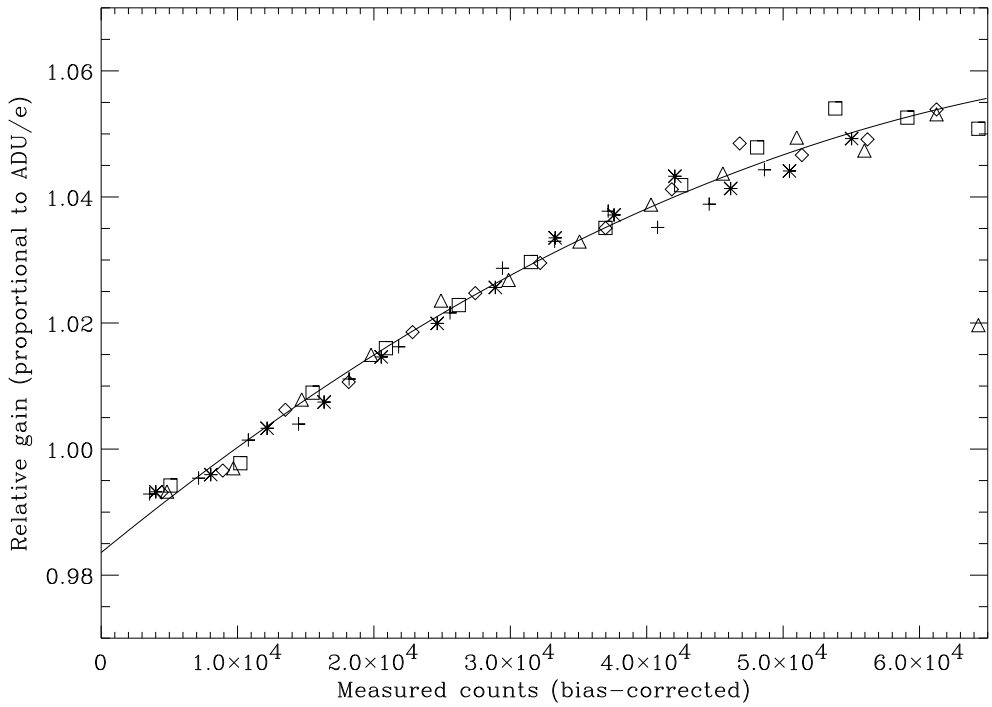

Figure 3.1 BRE measurement of non-linearity from a set of exposures in March 1997

3.2 Measurement of non-linearity using BRE method

BRE measurements of the non-linearity of the CCD system at the 74-inch Telescope at Mt. Stromlo Observatory were made in February and March 1997, along with an application of the ratio method where half of the slit was covered with a filter (Section 3.4). I used the 2Kx2K Tektronix chip (CCD10, serial number 1509BR24-01), with a nominal gain of 2e/ADU, with the B grating (dispersion 0.5Å/pixel) set up to look at the 6000Å to 7000Å wavelength region. A tungsten lamp was used for the light source.

Sixteen sets of repeat exposures were made for the BRE method as described in Section 3.1.1, with the maximum number of repeats ranging from 10 to 16. For each set of repeat exposures, plots of non-linearity (measured-counts / expected-counts versus measured-counts) were made using five different regions on the CCD. A straight line was fitted to each plot across the region from 0 to 30000 measured-counts so that each data set could be normalised to a relative gain of 1.0 at 10000 counts. For each set, a quadratic fit was made using all the five plots. Figure 3.1 shows one of the sixteen sets with the five plots combined, this set has the best quadratic fit. There is a 7% change in the gain between 0 and 64300 counts when the detector becomes digitally saturated (the bias level is $\sim$1200 ADU and the digital saturation before bias correction is 65535 ADU). The large non-linearity in this case may be because the CCD is only of engineering-grade; there are CCDs with a change in gain of less than 0.5% across a similar range.

Next, I combined the best five sets, which were all from March 1997, to produce a final

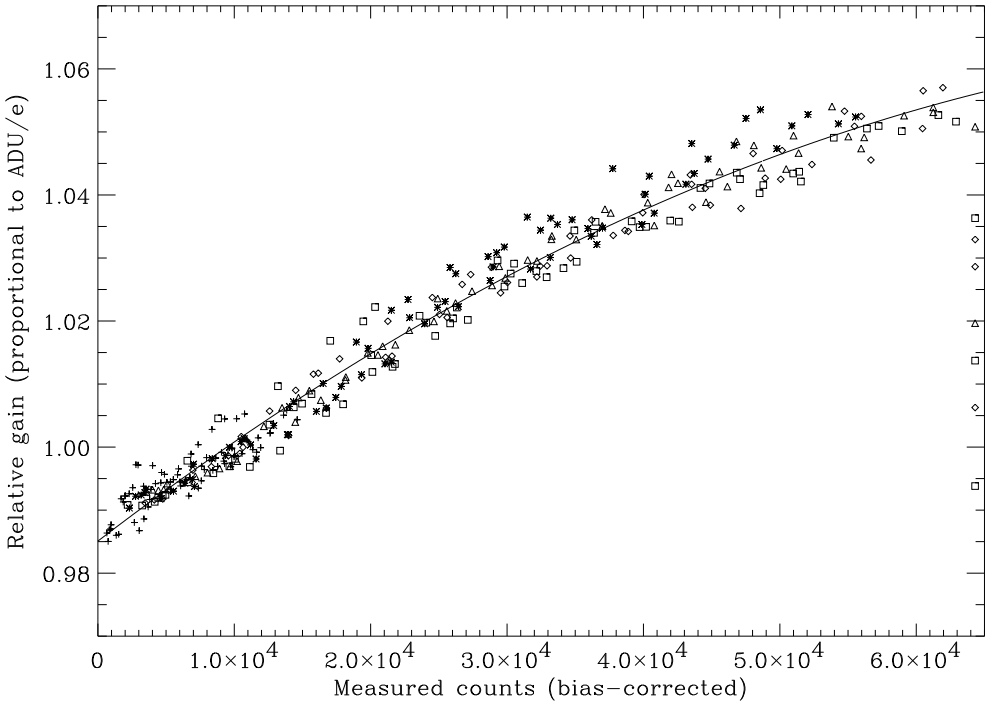

Figure 3.2 BRE measurement of non-linearity from five sets of repeat exposures

plot. For unknown reasons, the BRE measurements of non-linearity from February 1997 were not as good. Figure 3.2 shows the final plot with a quadratic fit to the data points. 3rd and 4th order polynomial fits to the data were only slightly better than a quadratic fit. The coefficients of different fits are shown in Table 3.1. In order to convert data to expected-counts, we divide the measured-counts by the relative gain.

Table 3.1 Coefficients of polynomial fits to non-linearity measurements

Polynomial	Coeff.				
1st order	0.989	1.17E−06			
2nd order	0.985	1.66E−06	−8.65E−12		
3rd order	0.987	1.32E−06	5.63E−12	−1.60E−16	
4th order	0.988	8.22E−07	4.28E−11	−1.12E−15	7.90E−21

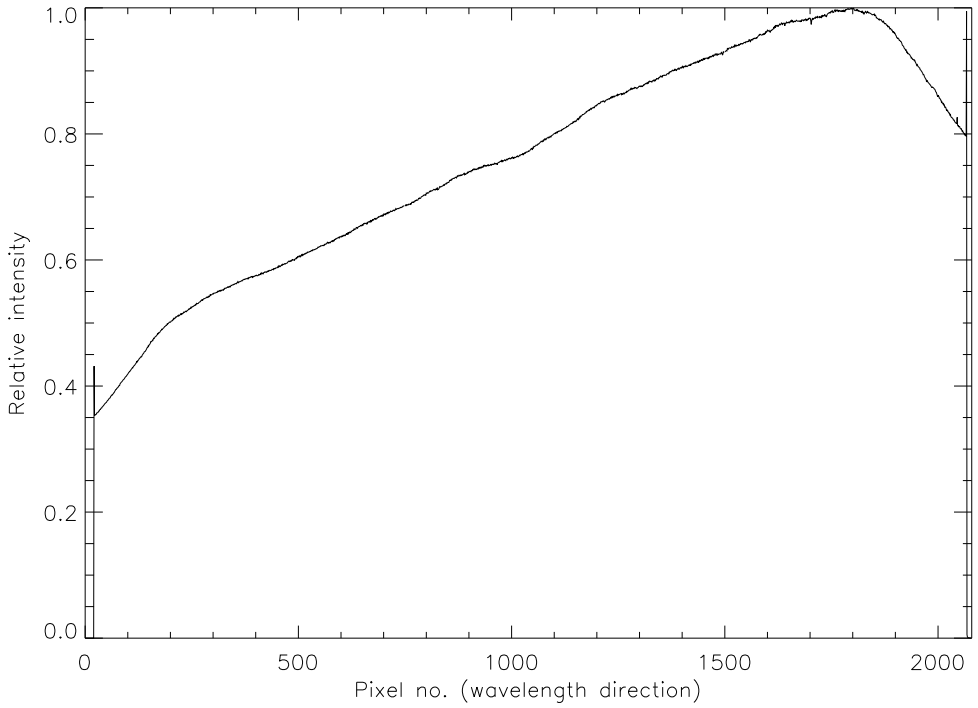

Figure 3.3 Cross-section of flat-field from May 1996

3.3 Stability of non-linearity curve

In this section, I compare non-linearity data taken in May 1996 and February 1997 using the ratio method in order to test the stability of the CCD10 system. The BRE method and the ratio method using a filter are more accurate, but no measurements were made in May 1996. However, flat-field spectra of various exposure times were taken and can be analysed using the ratio method. Figure 3.3 shows a cross-section of the tungsten lamp flat-field images that I used for the non-linearity tests. The aim is to test whether the non-linearity curve measured in 1997 can be applied to the 1996 data.

I measured the ratios between certain regions of the flat-field images and the highest intensity part of the images. For a linear detector and a lamp with a stable temperature, the ratio between two fixed regions in the flat-field spectrum should not depend on the actual light level. Figures 3.4–3.8 show the non-linearity ratio plots for the two years at ratios of approximately 0.450, 0.585, 0.680, 0.810 and 0.915. The scatter in the plots are mainly due to changes in temperature of the flat-field lamp which produces a variable intensity gradient across the spectrum. However, there is clearly a decrease in the measured ratio at higher light levels due to the non-linearity of the CCD. This is consistent with an increase in the relative gain of the CCD at higher light levels, as seen using the BRE method. At a ratio of approximately 0.450 (see Figure 3.4), the decrease in the ratio between light levels of 5000 counts and 60000 counts is about 2%. Note that at near 64300 counts the ratio can go up because the ADU counts are saturated for the higher value. The shapes of

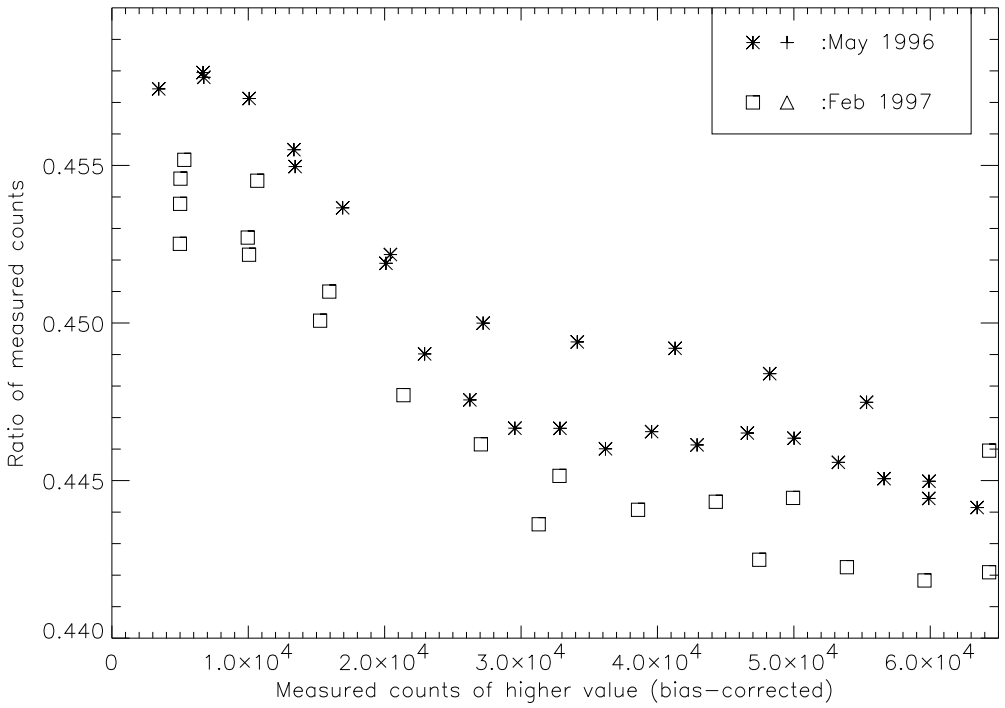

Figure 3.4 Comparison of non-linearity data using ratio method

the ratio curves are approximately the same for May 1996 and for February 1997 which means that I cannot detect any change in the non-linear behaviour of the CCD. This is evident in Figures 3.4–3.6 when the ratio change is large. I assumed that there was no significant difference between the non-linearity from 1996 and from 1997 and, therefore, used the non-linearity curve measured in 1997 to correct for the non-linearities in the 1996 data.

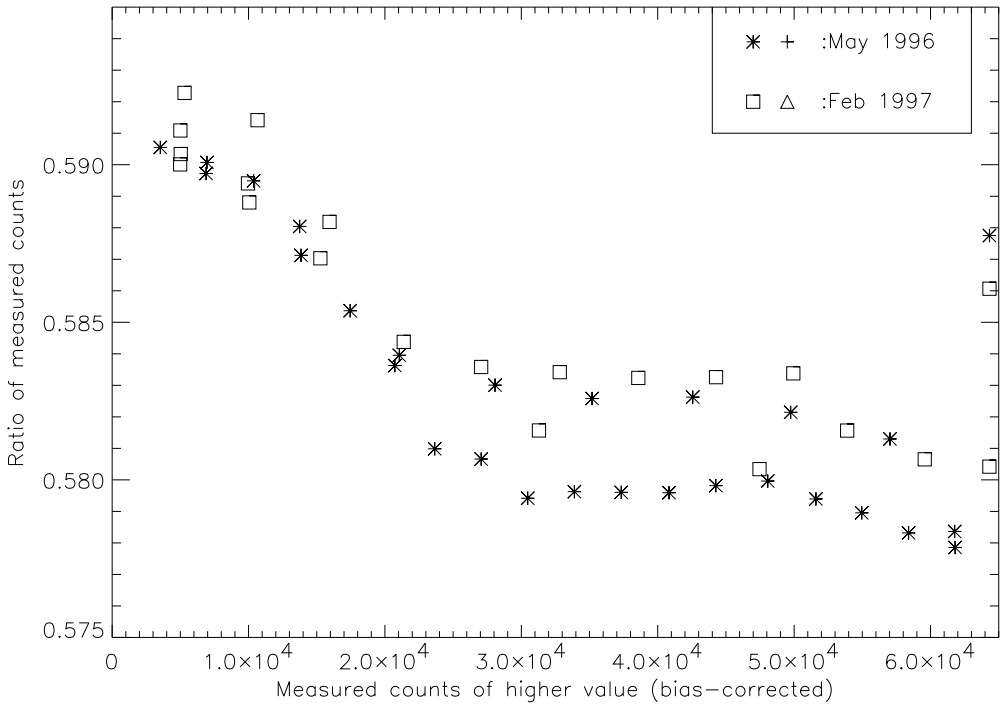

Figure 3.5 Comparison of non-linearity data using ratio method

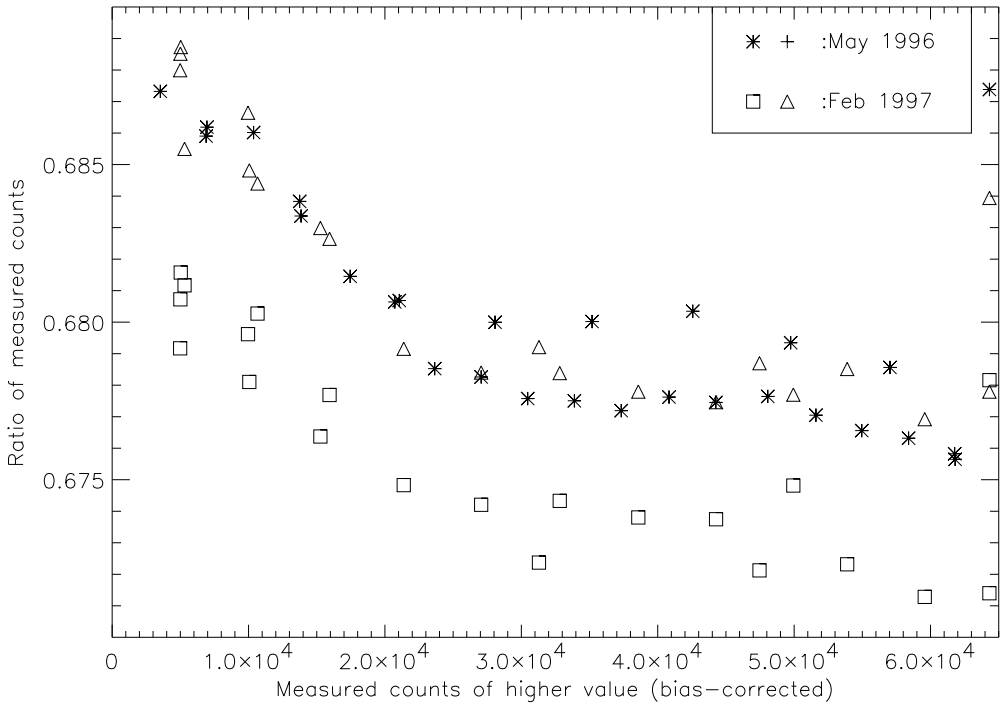

Figure 3.6 Comparison of non-linearity data using ratio method

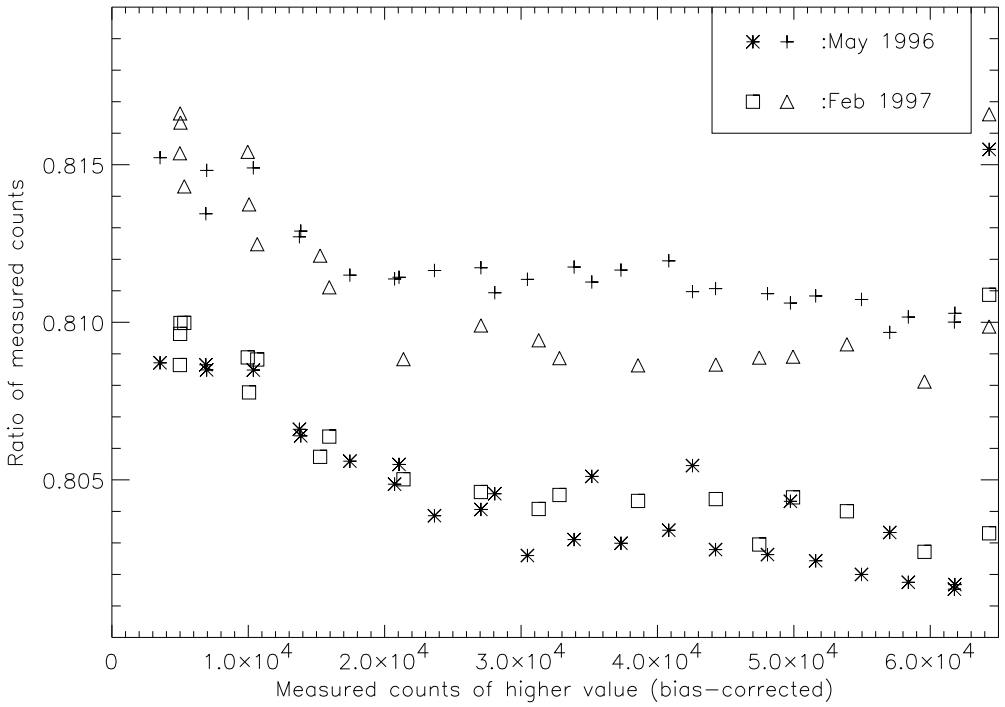

Figure 3.7 Comparison of non-linearity data using ratio method

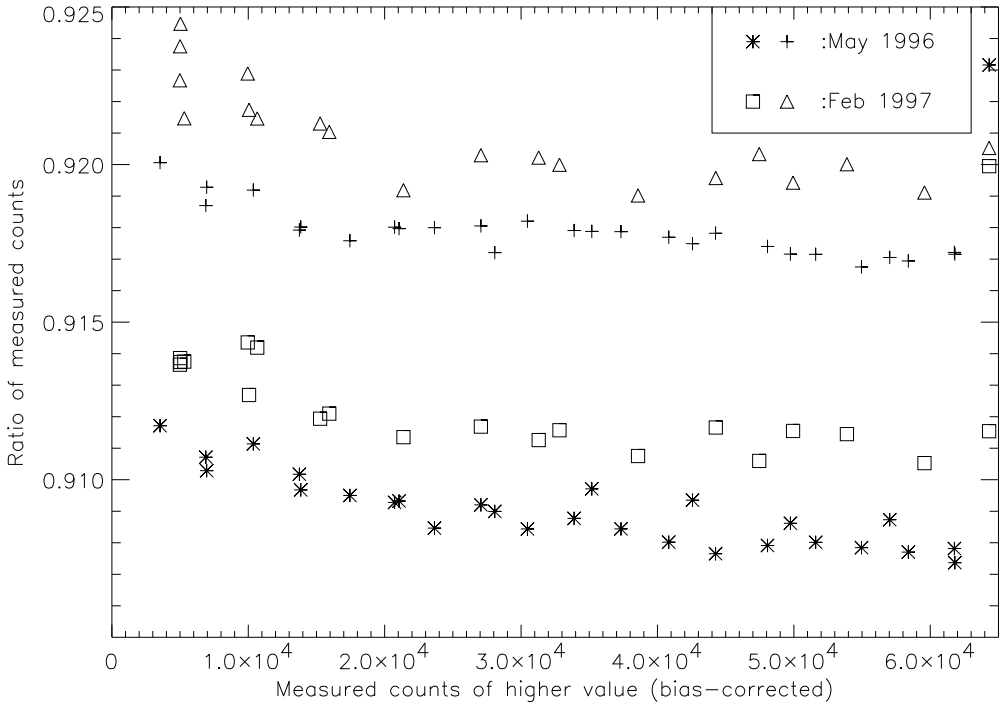

Figure 3.8 Comparison of non-linearity data using ratio method

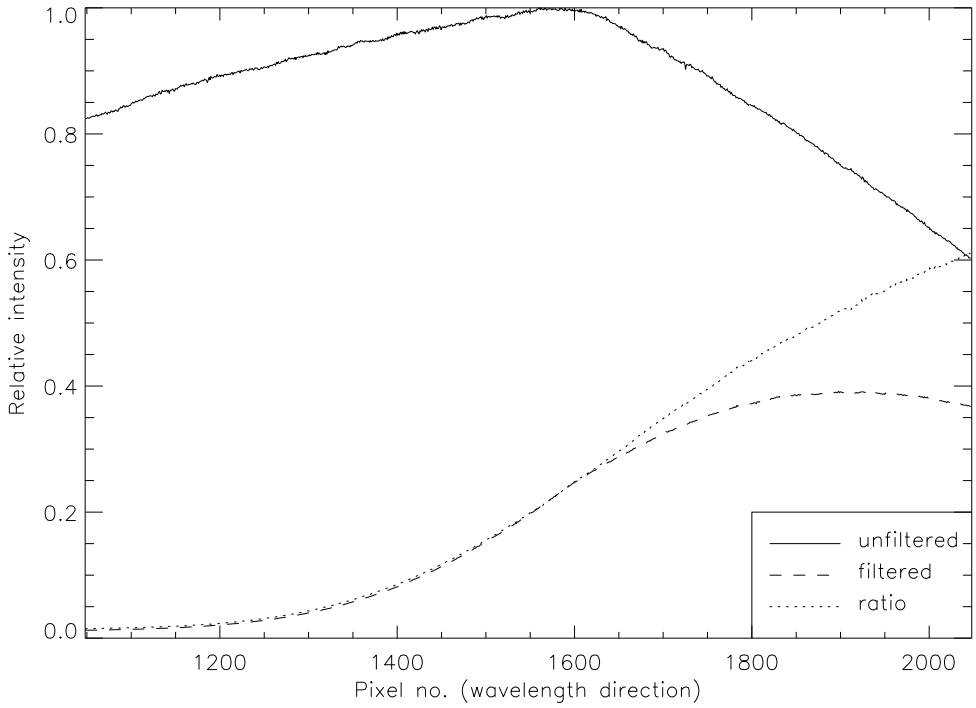

Figure 3.9 Cross-sections of flat-field from February 1997. The solid line represents the direct spectrum of the lamp with vignetting above pixel 1600. The dashed line represents a parallel cross-section where the light has passed through a colour filter. The dotted line represents the transmission profile of the filter.

3.4 Checking the non-linearity curve

Ratio measurements using a colour filter, to cover half of the length of the slit, were made in 1997 to check the validity of the non-linearity curve of CCD10 derived using the BRE method. Figure 3.9 shows two cross-sections of a flat-field image from a filtered and an un-filtered part and the ratio between the two parts. In Figures 3.10–3.14, the ratios between the filtered and un-filtered parts of the image, at a certain wavelength, versus counts of the un-filtered part are plotted. The same measurements were made on the data before and after the 2nd order non-linearity correction given in Table 3.1.

There is a definite improvement in all the ratio changes by a factor of about 5 after the non-linearity correction has been made. However, this ratio method has a very low scatter and seems to be detecting higher order non-linearities (Figures 3.13–3.14) which were not evident using the BRE method. Note that at light levels below 10000 counts, the scatter is much higher, probably because of errors in bias subtraction. I have ignored this region for the purposes of this analysis. From Figures 3.10–3.11, it appears that the non-linearity correction is working quite well but perhaps slightly under-correcting at high light levels. I have tried re-reducing the BRE method by using different normalisations and different sets of exposures but the small discrepancy remains.

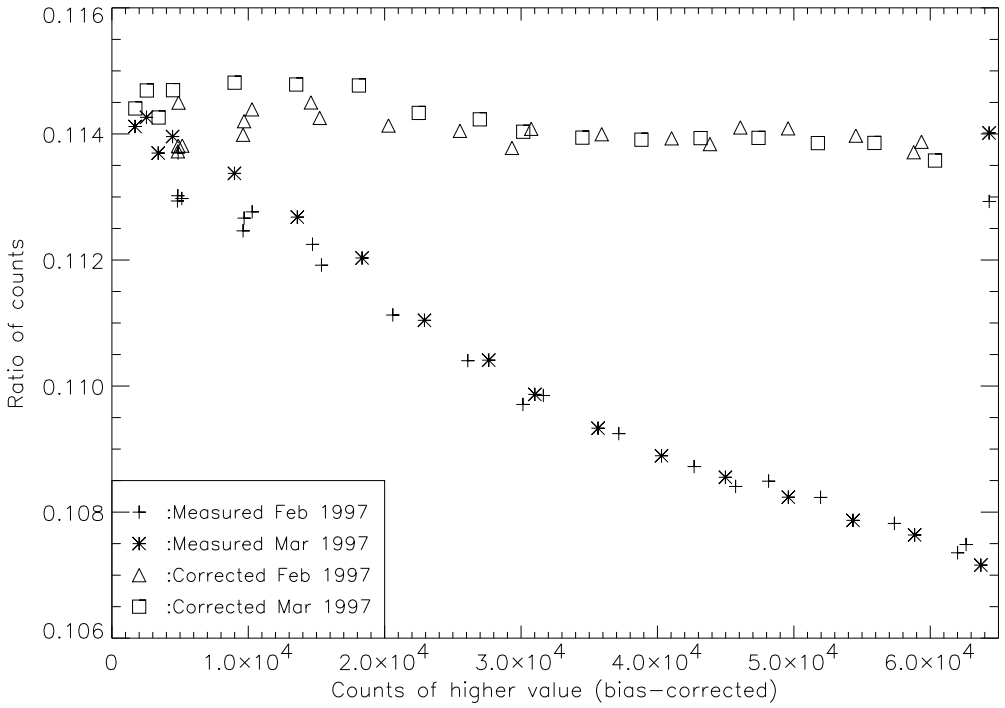

Figure 3.10 Testing of non-linearity curve using ratio method

Structure in the non-linearity curve appears around 18000 and 31000 counts, as is most evident in Figures 3.12–3.14. The obvious change in ratio at 31000 counts in Figure 3.14 is interesting because at this ratio ($\sim$0.58), there is structure in the non-linearity curve around the lower value (18000) as well as the higher value. Using 3rd and 4th order non-linearity corrections from the BRE method only slightly improves the glitches in the ratio curves. This is not surprising as a polynomial fit is not a good representation of what is occurring in the non-linearity curve at these points. It is also likely that the BRE method has smoothed over these high-order changes because of the normalisation and the scatter in the plots. Despite these glitches, the 2nd order fit derived by the BRE method has improved the non-linearity significantly and, therefore, it is valuable to use this non-linearity correction on data obtained with this CCD.

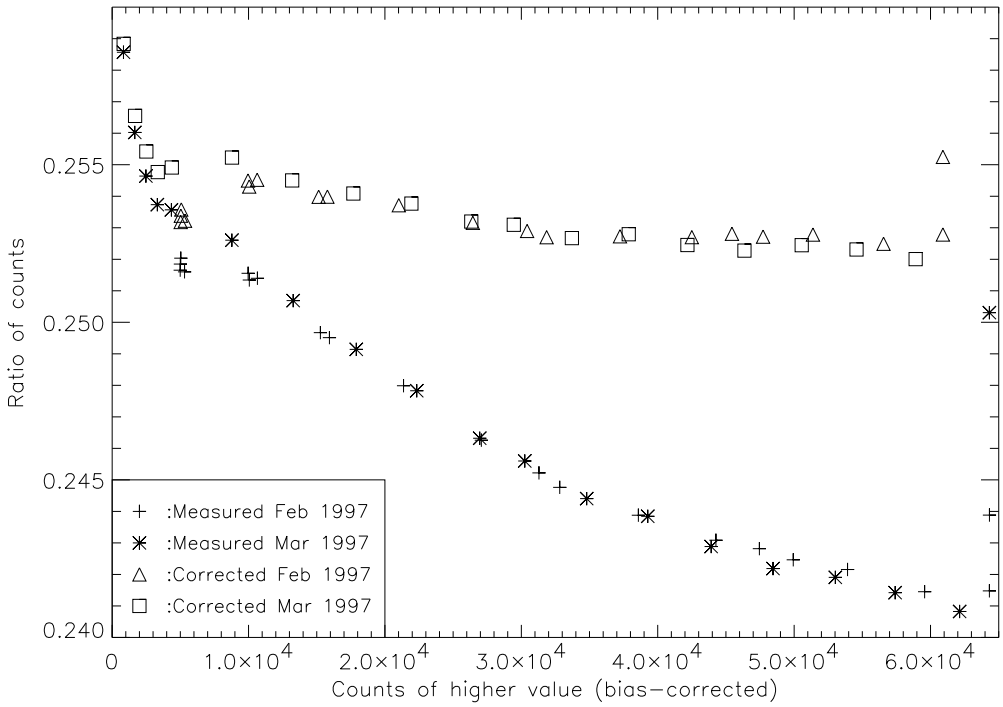

Figure 3.11 Testing of non-linearity curve using ratio method

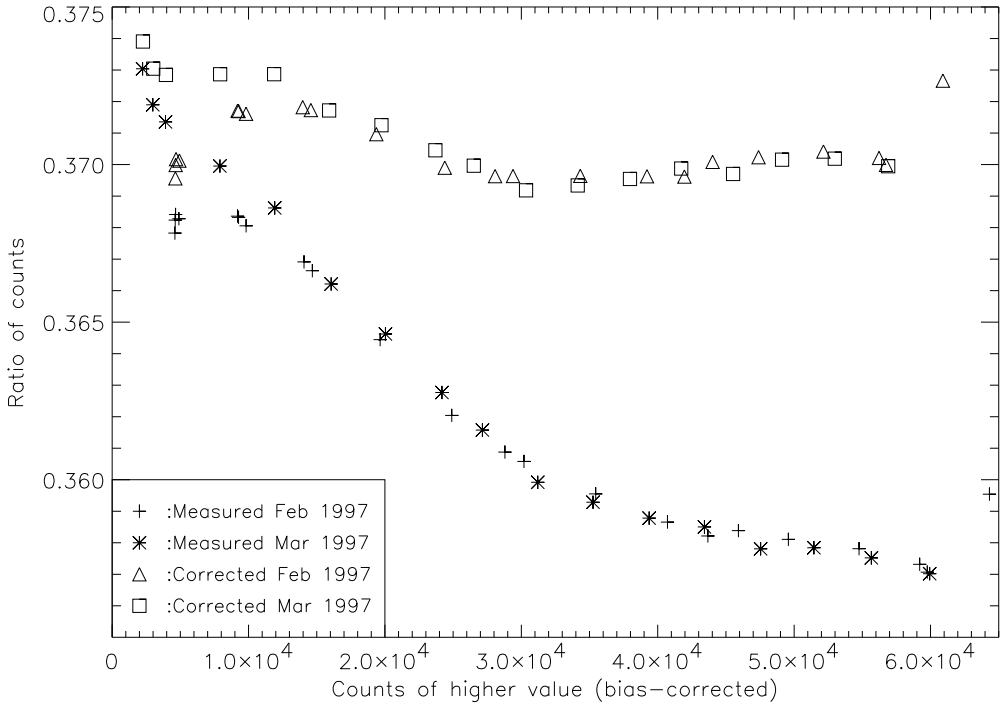

Figure 3.12 Testing of non-linearity curve using ratio method

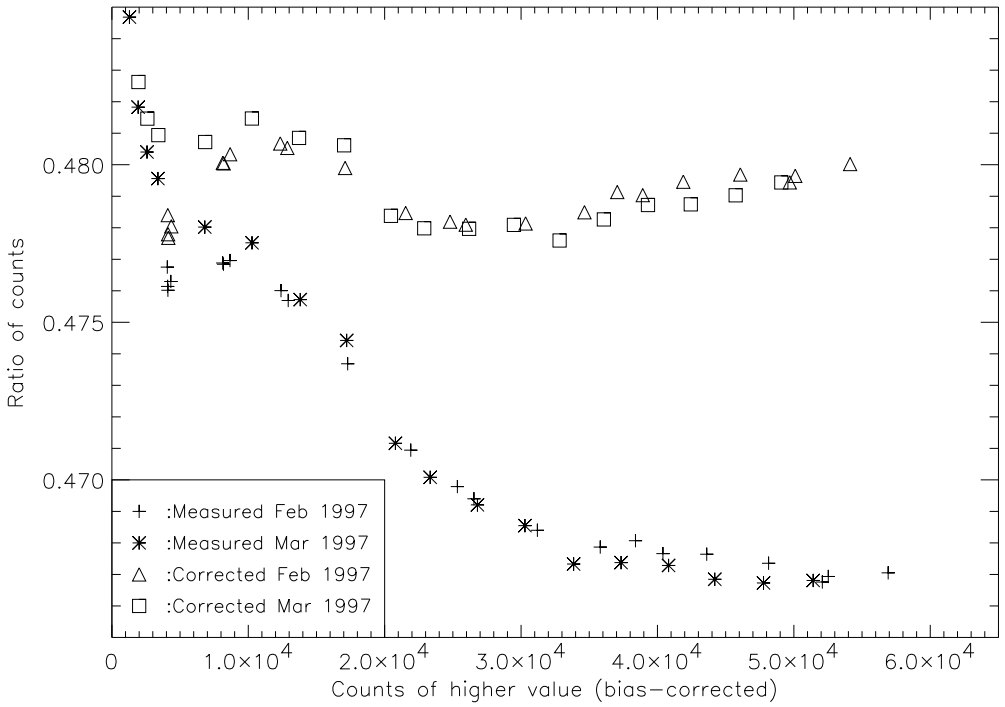

Figure 3.13 Testing of non-linearity curve using ratio method

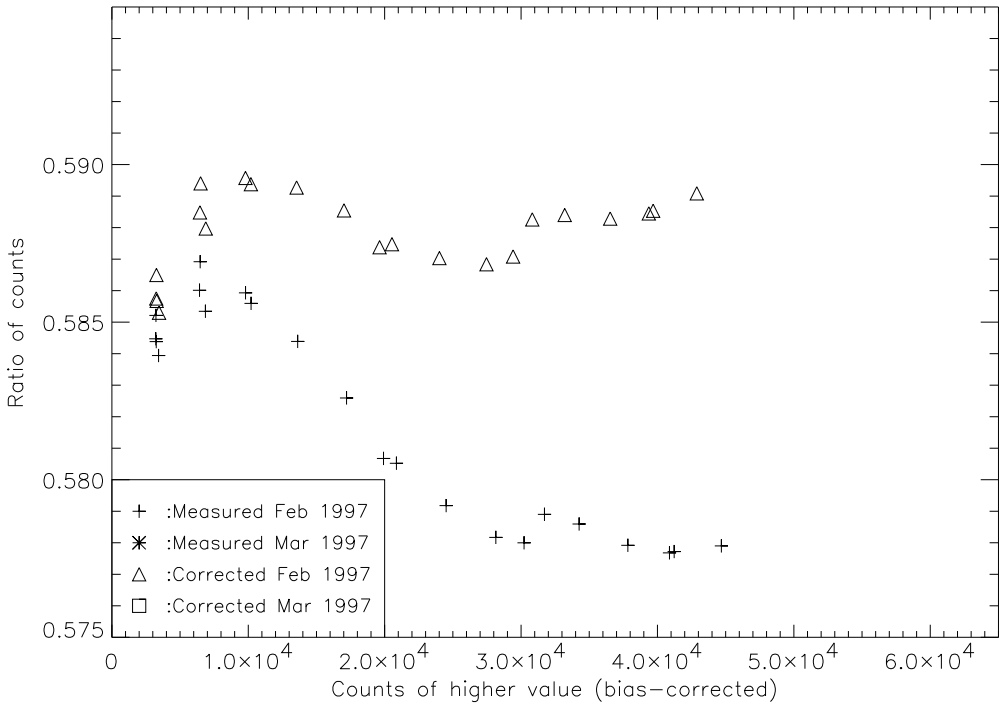

Figure 3.14 Testing of non-linearity curve using ratio method

3.5 Measurement of non-linearity using ratio method

It is possible that the ratio method can provide a better non-linearity curve, for example, by solving an equation of the form

$$R_{12} = \frac{N_1/f(N_1)}{N_2/f(N_2)} = \frac{N_1^{'}/f(N_1^{'})}{N_2^{'}/f(N_2^{'})} = \frac{N_1^{''}/f(N_1^{''})}{N_2^{''}/f(N_2^{''})} = ... , \tag{3.1}$$

where N_1 and N_2 are the measured counts of the two regions, at different light levels N $N^{'}$ $N^{''}$ etc., $f(N)$ is the relative-gain function equivalent to measured-counts / expected-counts and, R_{12} is the ratio of the expected (or true) counts between the two regions (the corrected ratio). A fit can be made to the parameters chosen for the relative-gain function, by minimising the scatter in the corrected ratio between different light levels. Similar equations can be solved for different pairs of regions on the CCD. For low intensity non-linearity tests, it will be necessary to obtain a good overscan region for accurate bias subtraction. A non-linearity measurement of a CCD using the ratio method is described in this section.

In December 1998, I observed at Mt. Stromlo as part of a multi-site campaign to study the roAp star HR 1217 (organised by S. Frandsen et al.). A different CCD was used (2Kx4K SITe chip: CCD17, serial number 6044FCD04-01, gain 2.5 e/ADU, 1x2 binning), from the one that was used in 1996 and 1997 to study α Cir and HR 3831. For this campaign, it was important to measure the non-linearity of this CCD. I used primarily the ratio method and fitted only one parameter, the α parameter (Tinney 1996), to the data. This demonstrates that the ratio method can be used as an accurate and independent method to determine the non-linearity of CCDs.

The spectrum of a flat-field lamp was projected onto the CCD, using the B-grating of the coudé spectrograph in the range 6300–6900Å (dispersion 0.31Å/ pixel). A colour filter (BG 38) was placed directly over the slit, covering about half the length of the slit. This was secured with tape to avoid any movement of the filter during the measurements. The result of placing this filter was that a filtered spectrum and a direct spectrum were both projected onto the CCD. The ratio between the intensities in each spectrum varied between 0.1 and 0.4 depending on the wavelength. If the CCD is a perfectly linear system, the ratio between the intensities (bias-corrected) at each wavelength should remain the same and not depend on the exposure time or changes in the lamp flux.

17 exposures were taken with exposure times varying between 0.1 s and 6 s. The exposure times were first increased and then decreased to check if there was a systematic change with time. An average bias frame was subtracted from all the exposures, to remove spatial structure due to bias, and then overscan regions of the CCD were used to fine tune the bias correction. Six pairs of regions, each pair consisting of a filtered and a direct region, were chosen equally spaced along the dispersion direction (each region consisted of about 300 pixels). The mean intensity was measured for each region and exposure. The measured intensity ratios for each pair of regions are shown in Figures 3.15–3.20.

Tinney (1996) described the AAO CCD non-linearities in terms of an α parameter.

$$N_m = N_t(1 + \alpha N_t) \tag{3.2}$$

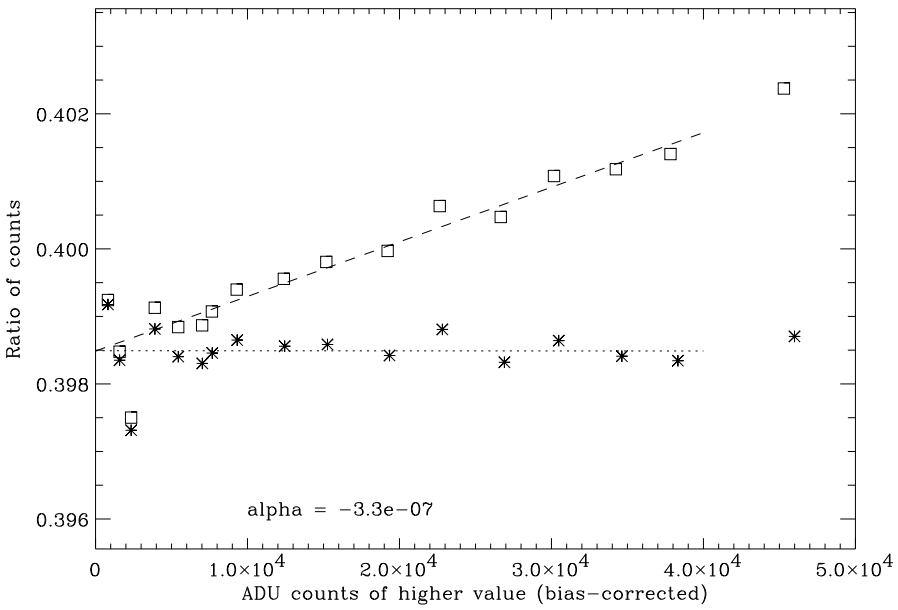

Figure 3.15 Non-linearity measurement using ratio method. The squares represent the measured ratios, while the asterisks represent the ratios after correcting the intensities using the alpha parameter. The lines are best fits to each set of ratios, between 0 and 40 000 counts, with lower weight given to measurements below 10 000. The alpha value has been chosen so that the slope of the best fit to the corrected ratios is zero.

where N_m are the measured counts in ADU above the bias level and N_t are the 'true' counts (normalised so that $N_t = N_m$ for $N_t \to 0$). The non-linearity of CCD17 was assumed to be represented by a single parameter similar to that defined by Tinney, except that the true intensity is defined in terms of the measured counts; $N_t = N_m/(1 + \alpha N_m)$. To first order, it makes no difference to the value of α.

For each set of ratio measurements, α was varied until the best fit for the corrected ratios had a slope of zero. The fit was obtained using the ratios with counts of the higher-value between 0 and 40 000. Lower weight was given to those with counts below 10 000 because of increased noise. Figures 3.15–3.20 show the value of α and the corrected ratios, for each set of measurements. For CCD17, $\alpha = -3.5 \pm 0.2 \times 10^{-7}$ from Figs. 3.15–3.18, where the correction factor is well defined. The α parameter is less well defined from Figs. 3.19–3.20 because of higher noise factors.

The ratio method removes the problems of requiring accurate exposure times and lamp-temperature stability to make accurate non-linearity measurements. Further improvement of the accuracy of the method described in this section could be made by (i) taking more exposures, (ii) increasing and decreasing the exposure time several times, and (iii) interspersing the exposures with bias frames. In the second case, this will reduce problems which might arise from a systematic change in the measurements with time. In the third case, monitoring any changes in bias frames will improve the accuracy of bias subtraction which is critical for measurements with low counts.

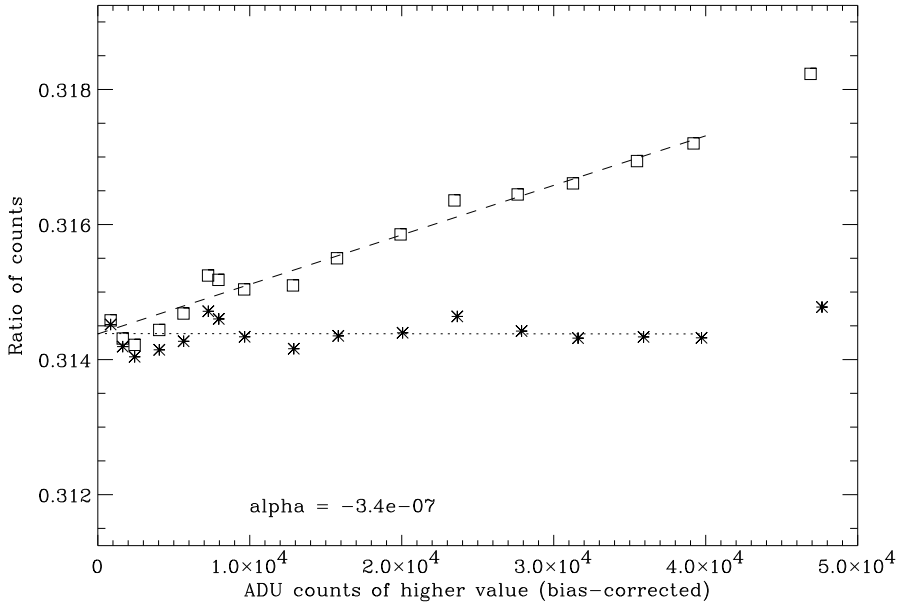

Figure 3.16 Non-linearity measurement using ratio method. See Fig. 3.15 for details.

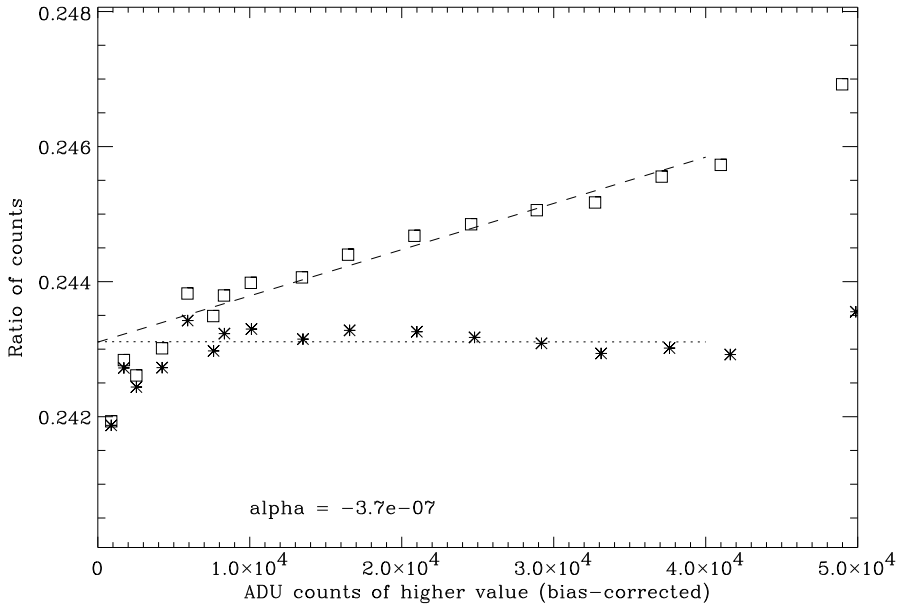

Figure 3.17 Non-linearity measurement using ratio method. See Fig. 3.15 for details.

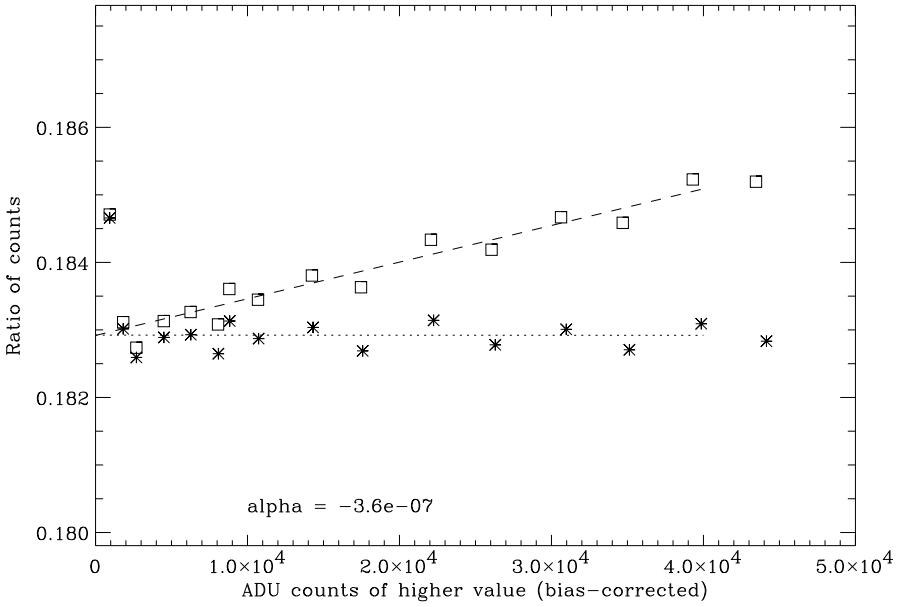

Figure 3.18 Non-linearity measurement using ratio method. See Fig. 3.15 for details.

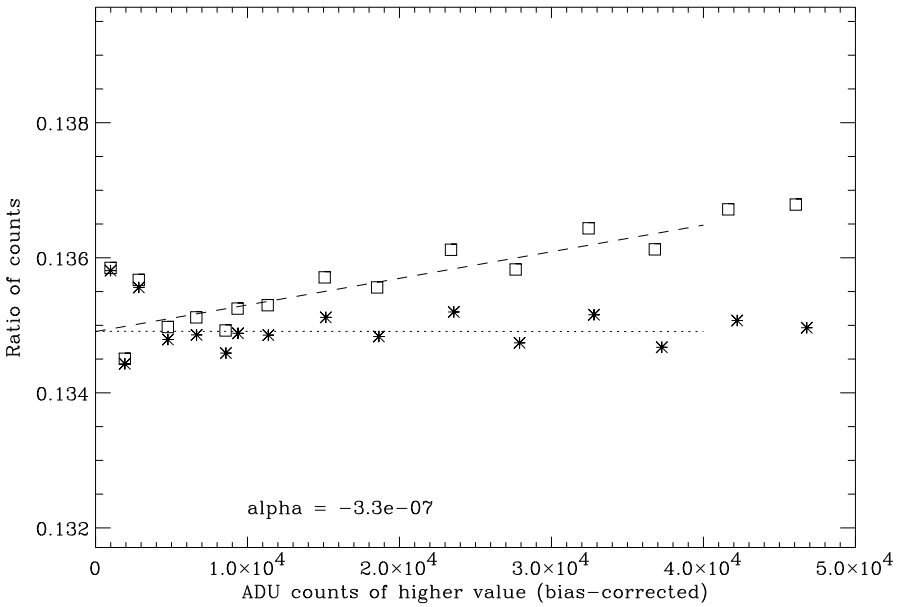

Figure 3.19 Non-linearity measurement using ratio method. See Fig. 3.15 for details.

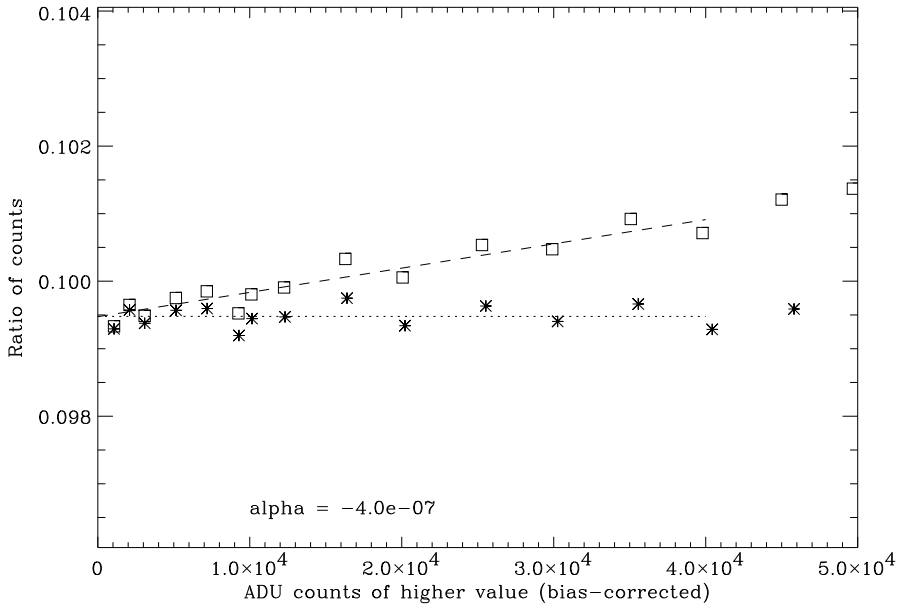

Figure 3.20 Non-linearity measurement using ratio method. See Fig. 3.15 for details.

3.6 Discussion

In Sections 3.2–3.4, I looked at the non-linearity of the Tek CCD10 at Mt. Stromlo (serial number 1509BR24-01, gain 2.0 e/ADU). This is the CCD with which I obtained most of the data for this thesis. In this section, I compare the non-linearity of this CCD with other CCDs.

For CCD10, the non-linearity cannot be accurately quantified using the α parameter due to higher-order effects. The measured value of α varies between 1.17×10^{-6} and 1.29×10^{-6}, depending on the range of counts considered (0–25000 up to 0–60000). Tinney (1996) quotes an α value of -3×10^{-8} for the AAO 1Kx1K Tek #2 chip (commissioned in July 1992) in 'normal' mode (gain 2.7 e/ADU). The linearity for this Tek CCD is a factor of 40 better than for CCD10 at Mt. Stromlo, the difference being due to the grade of the chip. Top science-grade CCDs should have a non-linearity parameter of $|\alpha| < 10^{-7}$ with a gain of about two electrons/ADU. This means that at an ADU level of 50 000, the correction is less than 0.5%. Note that, for a given CCD, the α parameter will be proportional to the gain (e/ADU) if the non-linearity is only a function of the number of electrons and not a function of the number of electrons and the gain.

In 1998, I observed at Mt. Stromlo using the SITe CCD17 (serial number 6044FCD04-01, gain 2.5 e/ADU). The α parameter was measured to be -3.5×10^{-7} in the range 0–40 000 ADU (Section 3.5). The CCD is of moderate science-grade with the non-linearity well characterised by one parameter, which means the non-linearity can be easily and accurately corrected when high-precision measurements need to be made.

The CCD17 measurements were taken using 1x2 binning to match the spectral data being taken during the observing run. The saturation level was determined to be around 57 000 ADU which is approximately double the saturation level when no binning is used. This is because the serial-register pixels of the CCD, where the electrons are combined, have a higher electron capacity. In this sense, the non-linearity is different when the CCD is binned. The α parameter should not depend on the binning because it is related to the controller conversion of electrons to ADU.

CCD10 has a non-linearity characterised by an α parameter of around $+1.2 \times 10^{-6}$, which is significantly non-linear compared to science-grade CCDs. Therefore, in order for this CCD to perform adequately in terms of high precision spectroscopy, it is necessary to apply a non-linearity correction. I used the 2nd order fit derived by the BRE method (Table 3.1) to correct the CCD data taken from Mt. Stromlo, for the results in Chapters 5–7. It would be difficult to make improvements on this correction because the non-linearity for this CCD is not easily quantified by two or three parameters.

In this chapter, I have demonstrated two techniques for measuring or checking the non-linearity of CCDs. The BRE method measures the variation in the intensity of a region on the CCD (using multiple exposures bracketed by single exposures to monitor any changes in the lamp's intensity). The ratio method measures the variation in the ratio between the intensities of two regions on the CCD. This can provide a more accurate non-linearity curve because it is less affected by changes in the lamp's flux and is unaffected by uncertainties in the exposure time.

Chapter 4

Hα profile variations in the long-period Cepheid ℓ Carinae

The content of this chapter was published in paper Baldry et al. (1997) in collaboration with Melinda Taylor, Tim Bedding and Andrew Booth. I wrote the paper and reduced the data with the supervision of T. Bedding. M. Taylor did most of the observing (see Table 4.1) with help from A. Booth.

4.1 Introduction

ℓ Carinae is the brightest classical Cepheid in the southern sky. It will be a primary target for the Sydney University Stellar Interferometer (SUSI) as part of a programme for measuring the angular diameter of Cepheids (Booth et al. 1995), and much work is being done to improve the general understanding and the radial velocity curve of this star (Taylor et al. 1997). Here we present spectra showing what appears to be continuous Hα emission throughout the whole pulsation cycle in ℓ Car. In long-period Cepheids the Hα line has often shown two components in absorption but only sometimes shown an emission feature (Rodgers & Bell 1968; Wallerstein 1972, 1983). We believe that the true shape and flux of the emission in ℓ Car are largely obscured by upper atmospheric and circumstellar absorption as occurs with Mg II emission (Böhm-Vitense & Love 1994). The origin of the emission feature may be a shock front in the atmosphere of the star or may be the upper atmosphere (we avoid the term chromosphere: see the discussion by Sasselov & Lester 1994).

From the early work on the Hα line in Cepheids (Wallerstein 1972), it appears that in stars with periods less than about 13 days the Hα line behaves more or less like other absorption lines. Anomalous Hα profiles have been observed in many long-period Cepheids (Grenfell & Wallerstein 1969; Schmidt 1970) and it is generally agreed that the photospheric line is largely obscured by upper atmospheric absorption and emission in these stars. However Schmidt (1970) argued that the wings of Hα could be used as an effective temperature indicator as long as the measurements of the width of the line are made far enough away from the upper atmospheric core. Our original aim was to measure the equivalent width of Hα in ℓ Car as a function of phase but this has not been possible with our data set.

ℓ Car (HR 3884, HD 84810) has $< V > = 3.7$, full range $\Delta V = 0.7$, $< B - V > = 1.2$ and a spectral type around G5Iab. We adopt a period of 35.54434 days and a zero-phase (maximum light) Julian date of 2447880.81 (Shobbrook 1992). The period is known to vary but not enough to affect the results in this chapter.

We use photometric phases referenced to maximum light. In order to convert to a more physically related phase it is best to define zero phase to be minimum radius, which occurs at photometric phase 0.93 in this star (i.e. add 0.07 to all the phases quoted in this chapter).

4.2 Observations and data reductions

We obtained high-resolution optical spectra of ℓ Carinae at Mount Stromlo Observatory, with the 1.88-m telescope and coudé echelle spectrograph, between February 1994 and April 1995. A single spectrum contained about 45 orders, each approximately 100Å long, projected on to a 2K Tek CCD. The dispersion was $\sim$0.05Å per pixel and the full width at half maximum of the instrumental profile was $\sim$0.10Å. Moderately full phase coverage of ℓ Car was obtained (the largest gap in the coverage is 0.085 of a cycle between phases 0.609 and 0.694). Table 4.1 provides a list of the dates and phases of the 33 spectra analysed for this paper.

The data were reduced using the FIGARO software package (Shortridge 1993). For the purposes of this chapter only the two orders containing Hα were reduced. Other work has been done on the radial velocities of metal lines by Taylor et al. (1997) using more of the orders.

The reduction began with bias subtraction followed by extraction of orders. Corrections using the flat fields were not applied to the data as they were not useful either for tracing the shape of the order or for correcting pixel-to-pixel variations on the CCD. This was because the two orders around Hα were in a vignetted part of the CCD, such that the flat field and the star profiles were significantly different and there were not enough photons in the combined flat field images to reduce the photon noise below the level of the pixel-to-pixel variations on the CCD. Once the orders were extracted, the white scattered light level was removed by using an estimate obtained from levels either side of the star light. Cosmic rays were removed by interpolating across that part of the spectrum. The spectra from the 29th March to the 10th April 1995 contained some high-frequency pattern noise which was reduced significantly by smoothing using a three-point triangle (0.25,0.50,0.25). This smoothing was applied to all 33 spectra to ensure consistency. In most cases no pattern noise was left, an exception being the data from the 1st April (see Figure 4.1, phase 54.244). Finally a pseudo-continuum was fitted to each spectrum and wavelengths were calibrated using arc spectra. The 'continuum fitting' was the most critical part of the data reduction and was done by eye, aiming to get a good fit over the region of the order 13Å either side of the Hα core at 6563Å. It is not possible to analyse the depth of the wings of Hα using this set of data because of the difficulty of obtaining a good continuum fit over a region much larger than 26Å. In fact the wings will have been removed by our fitting procedure.

Table 4.1 Log of the observations of ℓ Car

Date	UT	Observer	JD −2449000	Phase
1994 Feb 25	13.7	P.R.Wood	409.07	42.996
1994 Feb 26	11.3	P.R.Wood	409.97	43.021
1994 Feb 28	10.3	P.R.Wood	411.93	43.076
1994 Mar 01	12.1	P.R.Wood	413.00	43.106
1994 Mar 02	10.4	P.R.Wood	413.93	43.133
1994 Mar 29	10.0	P.R.Wood	440.92	43.892
1994 Mar 31	11.1	H.M.Schmidt	442.96	43.949
1994 Jun 27	08.2	M.M.Taylor	530.84	46.422
1994 Jun 28	07.7	M.M.Taylor	531.82	46.449
1994 Jun 29	08.2	M.M.Taylor	532.84	46.478
1994 Jul 09	08.9	M.M.Taylor	542.87	46.760
1994 Jul 10	08.2	M.M.Taylor	543.84	46.787
1994 Jul 11	08.7	M.M.Taylor	544.86	46.816
1994 Jul 12	08.6	M.M.Taylor	545.86	46.844
1994 Jul 13	07.8	M.M.Taylor	546.82	46.871
1994 Jul 14	07.9	M.M.Taylor	547.83	46.900
1995 Mar 29	11.6	M.M.Taylor	805.98	54.163
1995 Mar 31	08.7	M.M.Taylor	807.86	54.215
1995 Apr 01	08.7	M.M.Taylor	808.86	54.244
1995 Apr 02	09.0	M.M.Taylor	809.88	54.272
1995 Apr 03	08.8	M.M.Taylor	810.87	54.300
1995 Apr 04	09.1	M.M.Taylor	811.88	54.328
1995 Apr 05	08.7	M.M.Taylor	812.86	54.356
1995 Apr 08	13.4	M.M.Taylor	816.06	54.446
1995 Apr 10	11.7	M.M.Taylor	817.99	54.500
1995 Apr 11	08.7	M.M.Taylor	818.86	54.525
1995 Apr 12	09.1	M.M.Taylor	819.88	54.554
1995 Apr 13	09.2	M.M.Taylor	820.88	54.582
1995 Apr 14	08.7	M.M.Taylor	821.86	54.609
1995 Apr 17	08.6	M.M.Taylor	824.86	54.694
1995 Apr 18	08.4	M.M.Taylor	825.85	54.722
1995 Apr 19	11.6	M.M.Taylor	826.98	54.753
1995 Apr 20	08.7	M.M.Taylor	827.86	54.778

4.3 The Hα profiles

The Hα profiles are plotted in Figures 4.1–4.4 over the range 6550Å to 6576Å (heliocentric wavelength) and are normalised so that the continuum is at approximately 1.0, except that each plot is offset from the previous one by a factor equal to ten times the phase difference. The spectra are plotted from top to bottom in each figure in order of phase, but note that the observations span several cycles.

There is some repetition in the phase coverage from cycle to cycle, for instance the data from the 28th June 1994 and the 8th April 1995 are almost at the same phase. There are four pairs of spectra with a phase difference of less than 0.010 (43.892 & 46.900, 46.449 & 54.446, 46.760 & 54.753, 46.787 & 54.778). There are slight differences between the profiles from cycle 47 and from 55 but we suggest they are caused by the changing strength and position of the terrestrial atmospheric lines. We see no significant cycle to cycle variations in the Hα profile in ℓ Carinae during 1994 and 1995. Taylor et al. (1997) discuss variations from cycle to cycle in the radial velocities of metal lines.

Throughout the whole pulsation cycle, there is a dominant absorption component (6562.9Å) whose velocity (+4 km s^{-1}) appears to be constant. This means that it does not partake in the pulsation and we attribute this component to a circumstellar shell; this was also seen by Rodgers & Bell (1968). Mass loss (Deasy 1988) from the star is the probable origin for the circumstellar material. There must also be at least one other absorption component and an emission component to explain the complexity of the profile at different phases. The radial velocities of the non-constant components are difficult to measure due to blending effects.

From phase 0.1 (just after maximum light) to phase 0.4 there is an obvious red-shifted emission component of Hα. The spectrum from phase 0.106 also shows more possible absorption components at 6561.8Å and at 6563.7Å. The latter feature is possibly caused by a weak terrestrial line (rest wavelength 6563.521Å). Alternatively this profile could be caused by a very weak emission feature not related to the redward emission. These weak features have disappeared by phase 0.244, leaving a P-Cygni-like profile. From phase 0.4 we see a weakening of the redward emission and by phase 0.500 (minimum light) it has disappeared. At this point there may be a very weak blueward emission component but this is not convincing due to the possibility of the line Si I (rest wavelength 6560.6Å) becoming stronger and creating this profile. However the blueward emission grows stronger (see Figure 4.3) and by phase 0.844 it is clearly present. Figure 4.4 shows the sudden decrease in the blueward emission from phase 0.892 to 0.996. Then from maximum light onwards the cycle starts again with an increase in the redward emission.

During the phases around maximum light (see Figure 4.4) there is evidence of absorption line doubling, as has been seen in other Cepheids (Grenfell & Wallerstein 1969; Wallerstein 1972, 1983) but there is also possible contamination with terrestrial lines. The weak nature of this effect in ℓ Car is consistent with significant absorption line doubling from the upper atmosphere, which has been mostly obscured by circumstellar absorption.

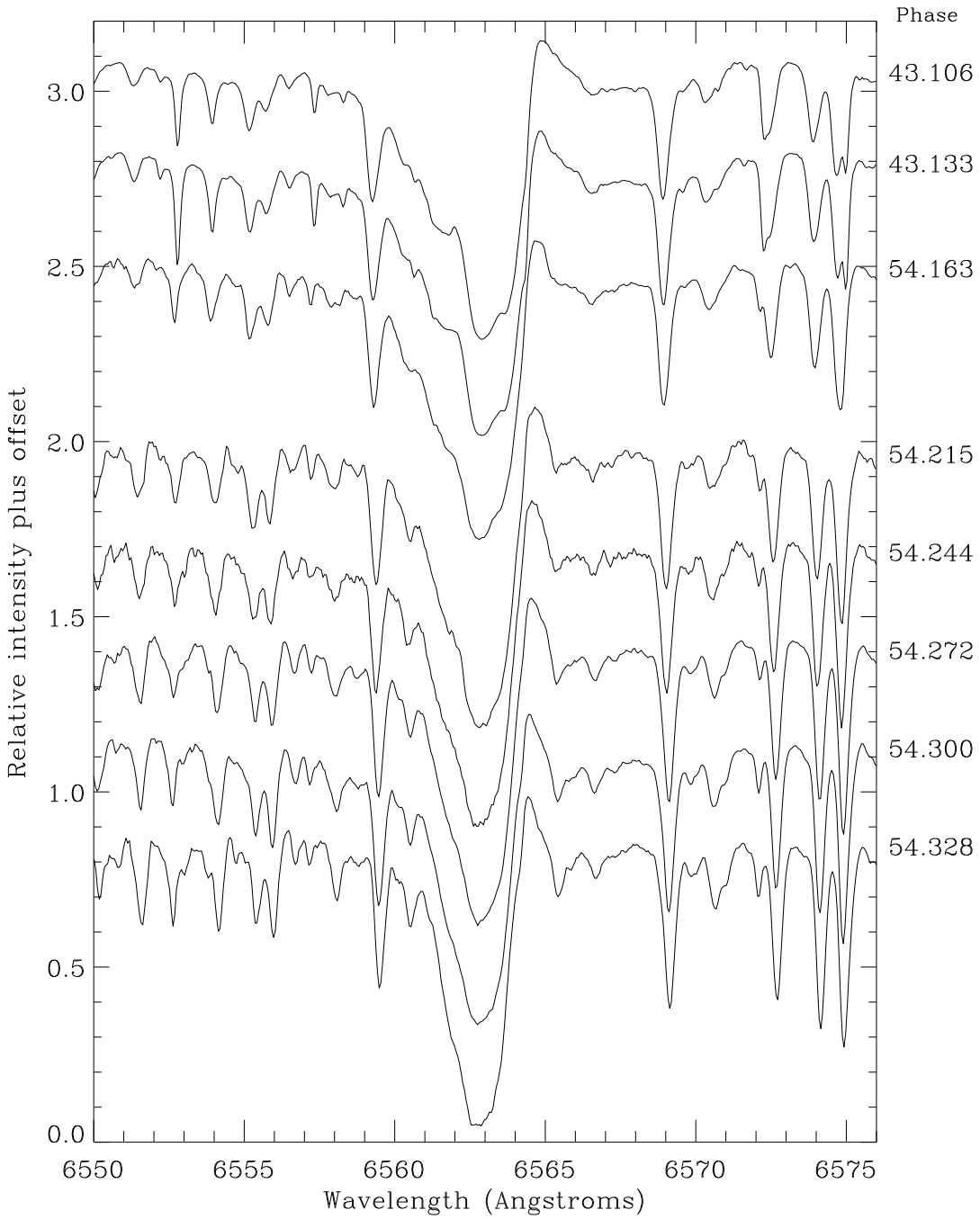

Figure 4.1 Plots of the Hα profile in ℓ Car when the emission is redward of the central absorption

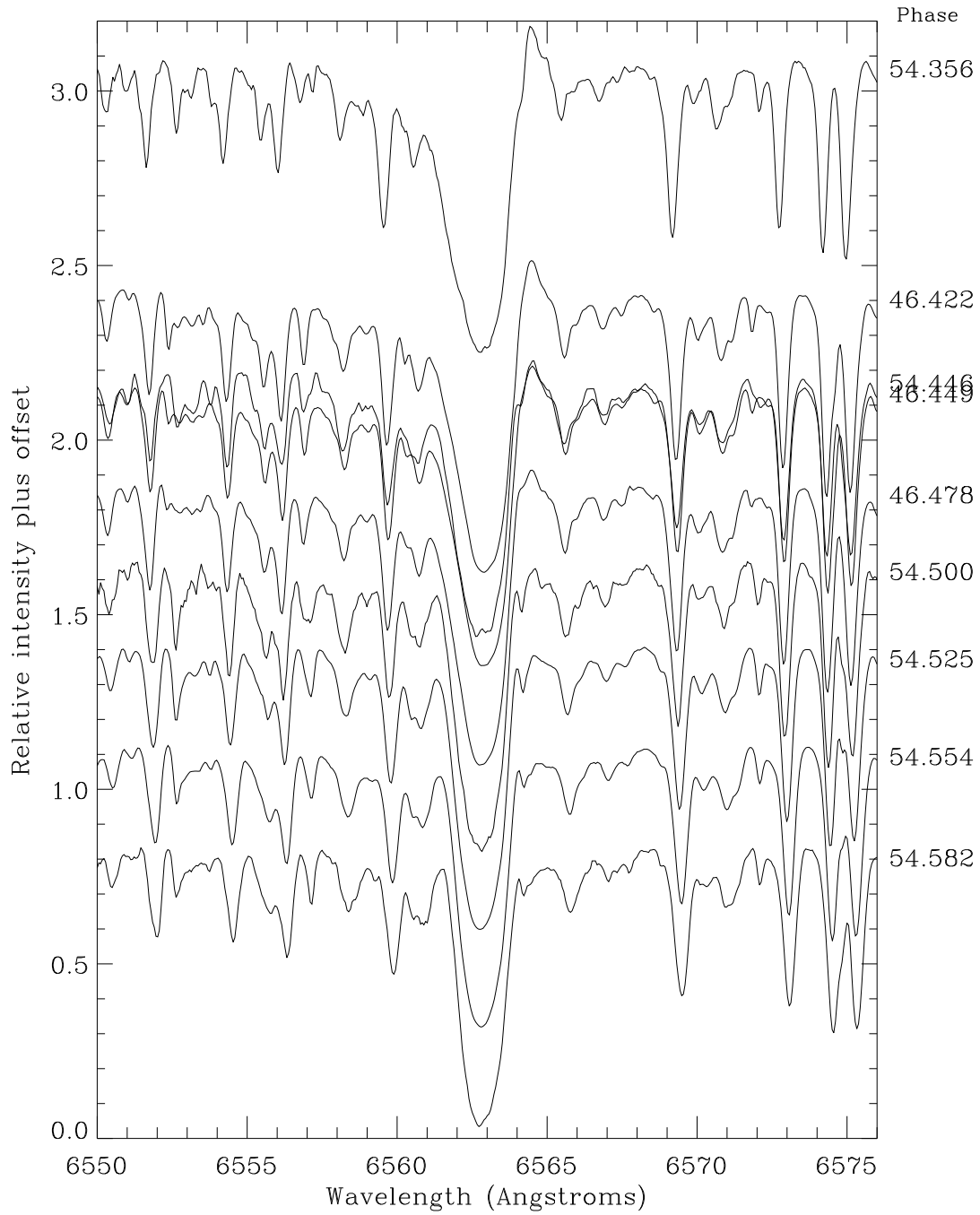

Figure 4.2 Plots of the Hα profile in ℓ Car during the change from redward to blueward emission

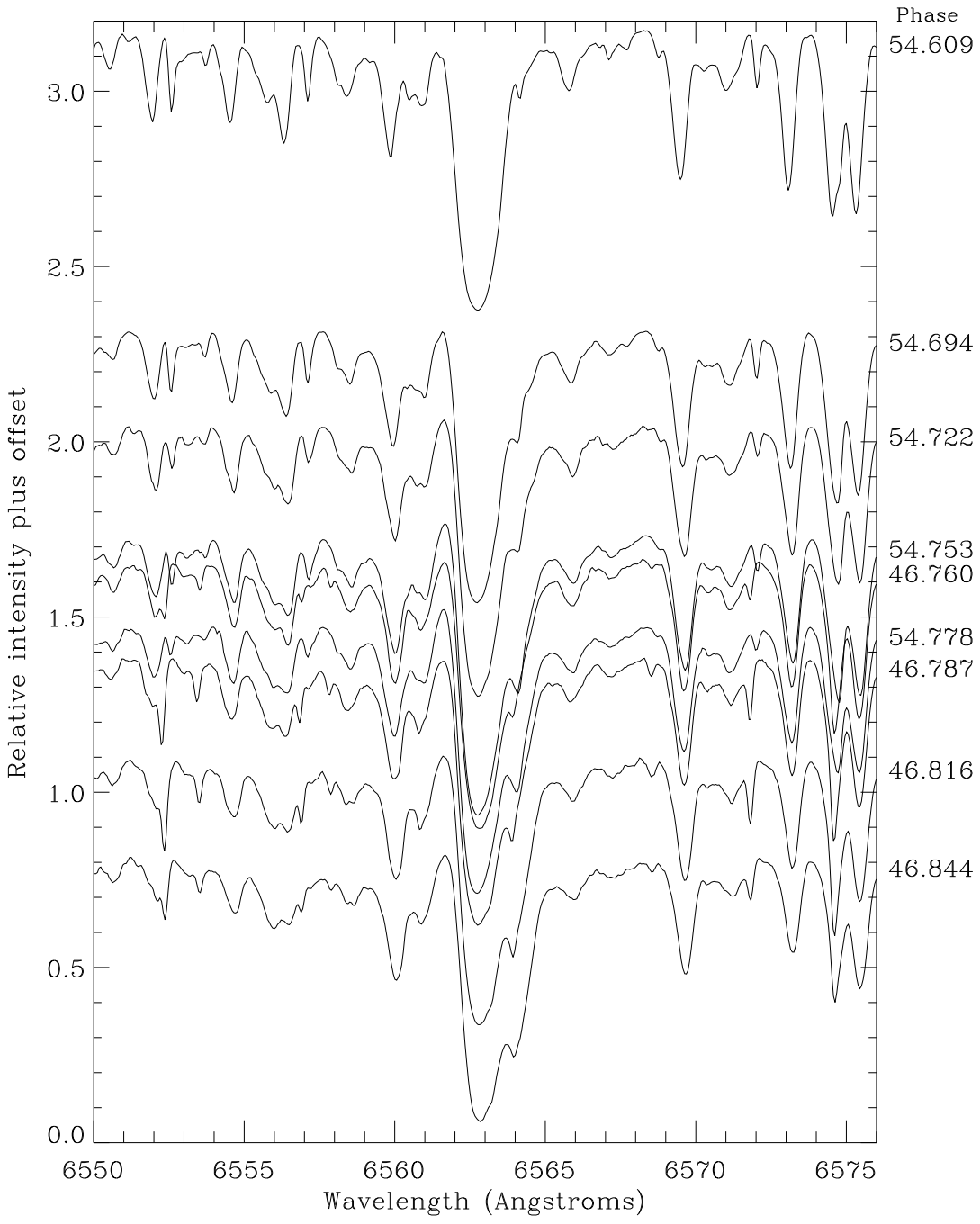

Figure 4.3 Plots of the Hα profile in ℓ Car when the emission is blueward of the central absorption

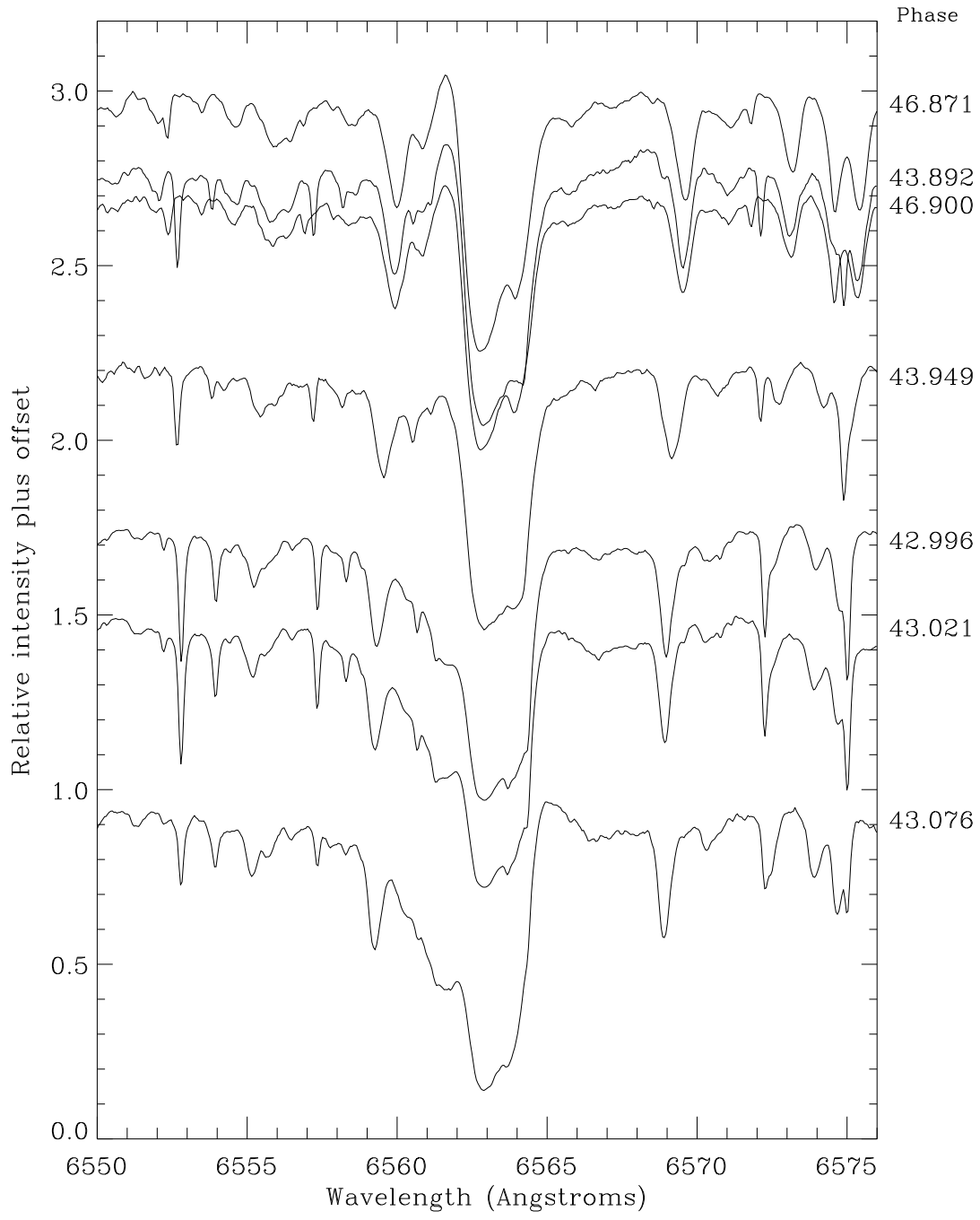

Figure 4.4 Plots of the Hα profile in ℓ Car during the change from blueward to redward emission

4.4 Discussion

Hα emission is seen in other yellow supergiants (Sowell 1990; Mallik 1993) and not just in long-period Cepheids. Sowell (1990) observed Hα emission in 13 out of 40 stars in his survey and several other stars had possible weak emission features. Mass flows and circumstellar shells are invoked to explain some of the distorted Hα profiles in these stars. For photometrically variable supergiants there are also pulsation and shock mechanisms capable of producing asymmetrical profiles. This makes it difficult to determine the cause of the observed Hα emission in Cepheids because one cannot easily distinguish between a generic supergiant phenomenon, where the emission is constant but the profile changes due to blending effects with an absorption component, and a pulsation phenomenon where the emission actually changes throughout the cycle.

Barrell (1978) discovered a surprisingly high frequency and strength of Hα emission components in beat Cepheids, which are classical Cepheids having more than one mode of pulsation. She suggested that the emission may indicate the existence of an acoustically heated upper atmosphere surrounding beat Cepheids. She (Barrell 1981) later made measurements of the effective temperatures of some beat Cepheids as a function of phase by using the width of the Hα line. This was possible because the emission in the beat Cepheids was not present most of the time and if present was not usually strong enough to affect measurements using the wings of the Hα line.

There have been several studies of Hα behaviour in classical Cepheids (Bell & Rodgers 1967; Rodgers & Bell 1968; Grenfell & Wallerstein 1969; Schmidt 1970; Wallerstein 1972, 1979, 1983; Jacobsen & Wallerstein 1982; Wallerstein et al. 1992). In a few cases Hα emission has been observed but only on the red wing and only for a fraction of the pulsation cycle. Wallerstein (1972) suggested that a small red emission feature in T Mon is due to broad emission which is largely self-absorbed, leaving a small sharp red wing. The strong emission could be caused by shock heating.

Gillet et al. (1994) have observed BL Her, a Population II Cepheid. They observed a small sharp blue wing in Hα emission in phases 0.82 and 0.86 and absorption line doubling before and after maximum light. This is similar to what might be happening in ℓ Carinae between phases 0.8 and 0.2 except that the circumstellar material is obscuring the effect. Fokin & Gillet (1994) model the Hα profile in BL Her in terms of shock wave propagation in an extended atmosphere. We have to be careful about comparing BL Her and ℓ Car because of the difference in periods, 1.3 days and 35.5 days respectively.

Now we compare previous work on ℓ Car with our own observations. Rodgers & Bell (1968) made a study of the Hα line in ℓ Car and presented profiles at 18 different phases, they used the same telescope and spectrograph 32-inch (81-cm) camera at Mt. Stromlo that we used, but with a lower dispersion (10Å/mm compared to 2Å/mm). Their data cover two sections of the pulsation cycle, phases 0.94–0.08 and 0.49-0.73. In the first section, their profiles are similar to ours and show the weak red-shifted emission starting between phases 0.0 and 0.08 (see Figure 4.4) but there is no evidence for any residual blue-shifted emission at phase 0.94 in their data. In the other section, there are more discrepancies between the two sets of observations. Again, there is no evidence for a blue-shifted emission in their data but they do not have any observations between

Table 4.2 Summary of some spectral features in ℓ Car

Feature	Phases	Ref. / Notes
Hα emission:		this chapter
red-shifted	0.0–0.5	peak at 0.25
blue-shifted	0.6–0.95	peak at 0.9
Mg II emission:		Böhm-Vitense & Love (1994)
stronger red wing	0.1–0.65	
stronger blue wing	0.7–0.1	
metal absorp. lines:		Taylor et al. (1997)
red-shifted	0.40–0.93	
blue-shifted	0.93–0.40	

phases 0.85 and 0.9 when we observed the blue-shifted emission to be strongest. The differences between our observations and theirs may be due to the dispersion, the data recording device (CCD vs photographic plate) or to an intrinsic change in the star.

Böhm-Vitense & Love (1994) made a study of ℓ Car in the UV using the International Ultraviolet Explorer (IUE). They studied the emission-line fluxes of several spectral lines (C II, C IV, Mg II, O I) as a function of pulsational phase. It is interesting to compare the Mg II emission with the Hα emission. The Mg II *h* and *k* line profiles consist of a strong emission component, which is effectively split into red and blue wings by a strong absorption component, producing a double hump appearance. The absorption component is stationary and is attributed to circumstellar gas. The overall flux of the emission changes throughout the pulsational cycle. Between phases 0.8 and 0.9 a very steep increase in flux occurs which they suppose is due to an outward-propagating shock. As well as the overall flux of the Mg II emission changing, the relative strength of the two wings also changes, but this variation is 0.1–0.15 cycles out of phase with our observed Hα emission shifts (see Table 4.2).

Table 4.2 shows that the Hα emission is approximately half a cycle out of phase with the motion of the photosphere as seen from the metal absorption lines. This implies that the emitting gas is travelling in the opposite direction to the photosphere. One possible explanation is that we are seeing moving gas in a shockfront on the far side of the star, this is possible if the radius of the emitting shock is much larger than the photosphere. In this model, the emission from the shockfront on the near side would be obscured by another absorption component, moving nearly in phase with the photosphere, other than the central component due to the circumstellar gas. Another explanation is that there is fairly stable emission from the upper atmosphere. This would arise from the limb and because of projection effects would have almost no Doppler amplitude. An absorption component moving back and forward obscures part of the emission feature creating the red and blue wings. In either case, the Hα absorption velocity (not the circumstellar component) is in

the opposite direction to the emission. This means that the Hα absorption is red-shifted between phases 0.6–0.95 and blue-shifted from 0.0–0.5 which gives it a phase lag of $\sim$0.1 behind the metal line velocity. This is consistent with this Hα absorption component being formed higher up in the atmosphere than the metal lines. Further theoretical work may indicate the origin of the Hα emission in ℓ Car.

Chapter 5

Velocities of Hα and metal lines in the roAp star α Circini

The content of this chapter was published in paper Baldry et al. (1998b) in collaboration with Tim Bedding, Michael Viskum, Hans Kjeldsen and Sören Frandsen. I wrote the paper and reduced the data, with the exception that M. Viskum reduced the La Silla data from the CCD images to the 1D spectra. I observed at Mt. Stromlo while M. Viskum observed at La Silla. M. Viskum and I were supervised by the other collaborators.

5.1 Introduction

Rapidly oscillating Ap (roAp) stars are a sub-class of the chemically peculiar magnetic (Ap or CP2) stars. The Ap phenomenon is characterised by spectra with anomalously strong lines of Si, Sr, Cr, other iron peak elements, Eu and other rare earth elements. The stars also have strong global magnetic fields of typically a few kG. The cause of the abundance anomalies is thought to be magnetically guided chemical diffusion, made possible because Ap stars have slower rotation rates than normal A stars. Some Ap stars also show evidence of an inhomogeneous distribution of elements (in spots) on the surface of the star (Rice & Wehlau 1991). Despite the name, the Ap stars range in temperature from spectral type B8 to F0 (luminosity class IV-V). At the cool-end of the range, the Ap stars overlap the instability strip and this is where the roAp stars are found. However, not all the Ap stars in the instability strip have been observed to pulsate (Mathys et al. 1996). A review of roAp stars with a comprehensive list of references is given by Kurtz (1990). Later reviews are given by Matthews (1991, 1997, 1998) and Martinez & Kurtz (1995a, 1995b), and a review on the theoretical aspects is given by Shibahashi (1991).

About thirty percent of main-sequence (normal) A-stars in the instability strip pulsate with photometric amplitudes greater than 10 mmag and with periods in the range 30–360 minutes; these are δ Scuti stars. However, the roAp stars are characterised by photometric amplitudes below 8 mmag and periods in the range 5–15 minutes. Both δ Scuti and roAp stars pulsate in low-degree ($\ell \leq 3$) *p*-modes but while the δ Scuti stars pulsate with low-overtones, the roAp stars vibrate in very high-overtones ($n \sim 25$–50). Explaining why the chemically peculiar roAp stars pulsate in much higher overtones than the normal δ Scuti stars remains one of the exciting challenges in this field. For recent theoretical work on different aspects of roAp stars, see Takata & Shibahashi (1995); Dziembowski & Goode (1996); Audard et al. (1998); Gautschy et al. (1998).

5.1.1 α Cir

α Circini (HR 5463, HD 128898, V=3.2, spectral type Ap SrEu(Cr)) is the brightest of the known roAp stars. It is situated at a distance of 16.4 ± 0.2 pc (parallax 61.0 ± 0.6 mas, HIP 71908, Perryman et al. 1997) and is a visual binary (secondary, V=8.2) with a separation of 15.6 arcsec. Kurtz & Martinez (1993) determined an equivalent spectral type of A6V ($T_{\rm eff} = 8000$ K), while Kupka et al. (1996) have derived $T_{\rm eff} = 7900 \pm 200$ K and $\log g = 4.2 \pm 0.15$.

Previous observations of this star in photometry (Kurtz et al. 1994b) have shown that its principal pulsation mode is a pure oblique dipole mode (ℓ=1) with a frequency of 2442 μHz ($P = 6.825$ min). Kurtz et al. (1994b) measured the amplitude of the principal mode to be 2.55 mmag (Strömgren v). They also found two rotationally split side-lobes (~ 0.27 mmag), four weaker modes (~ 0.15 mmag) and the first harmonic of the principal mode (~ 0.20 mmag). It has also been observed that the photometric amplitude depends on the wavelength (Weiss et al. 1991, Medupe & Kurtz 1998), with amplitude decreasing with increasing wavelength. In Section 5.5.3 we relate these wavelength dependent photometric amplitudes to our results.

The vast majority of studies of roAp stars have been made using photometry. In three stars, HR 1217 (Matthews et al. 1988), γ Equ (HR 8097; Libbrecht 1988, Kanaan & Hatzes 1998) and 10 Aql (HR 7167; Chagnon & Matthews 1998), oscillations have been convincingly detected in Doppler shift. For α Cir, based on the photometric amplitude given above, the relation of Kjeldsen & Bedding (1995) predicts a velocity amplitude of $160\,\mathrm{m\,s^{-1}}$. Belmonte et al. (1989) claimed a detection in α Cir at an amplitude of $1000\,\mathrm{m\,s^{-1}}$ using a line at 5317.4Å, but this result was in doubt given that Schneider & Weiss (1989) had set an upper limit of $100\,\mathrm{m\,s^{-1}}$ for possible radial velocity variations, using a wavelength region from 6450Å to 6500Å. More recently, an upper limit for α Cir of only $36\,\mathrm{m\,s^{-1}}$ (peak-to-peak) was set by Hatzes & Kürster (1994) at the frequency of the principal photometric pulsation mode, using a wavelength region from 5365Å to 5410Å. In this chapter we examine the radial velocity amplitude of the principal mode for different wavelength bands. From our work (see also Viskum et al. 1998a) and from the work by Kanaan & Hatzes (1998) on γ Equ, it is apparent that the velocity amplitude in roAp stars can vary significantly from line to line, and that previous upper limits reflect averages over the wavelength regions used.

5.2 Observations

We have obtained intermediate-resolution spectra of α Cir using the coudé spectrograph (B grating) on the 74-inch (1.88-m) Telescope at Mt. Stromlo, Australia and the DFOSC spectrograph mounted on the Danish 1.54m at La Silla, Chile. We have a total of 6366 spectra from a period of 2 weeks in 1996 May (Table 5.1).

The Stromlo data consist of single-order spectra, projected onto a 2K Tektronix CCD, with a wavelength coverage of 6000Å to 7000Å. The dispersion was 0.49Å/pixel and was nearly constant across the spectrum, with a resolution of approximately 1.5Å set by the slit width of 2 arcsec. The typical exposure time was 28 seconds, with an over-head between exposures of 17 seconds. The average number of photons/Å in each spectrum was about 800 000.

The La Silla data consist of echelle spectra containing six orders, projected onto a 2K LORAL CCD, with a total wavelength coverage of 4500Å to 8000Å. For this chapter, we have only considered the order containing Hα, which covers the range 6200Å to 7200Å. The dispersion varied from 0.51Å/pixel to 0.70Å/pixel across this order, giving a similar resolution to the Stromlo data. For the La Silla data, the typical exposure time was 40 seconds with an over-head of 42 seconds. The average number of photons/Å in the Hα order of each spectrum ranged from about 480 000 at the blaze peak (6700Å) to about 120 000 at the blue end (6200Å).

Table 5.1 Log of the observations of α Cir

UT-date	Site	No. of hours	No. of spectra	Julian dates −2450000
1996 May 05	Stromlo	0.97	23	209.31 – 209.35
1996 May 06	Stromlo	3.66	249	210.19 – 210.34
1996 May 09	La Silla	4.13	123	212.77 – 212.94
1996 May 09	Stromlo	12.05	785	212.84 – 213.35
1996 May 10	La Silla	3.78	142	213.77 – 213.92
1996 May 10	Stromlo	11.82	640	213.83 – 214.32
1996 May 11	La Silla	4.15	151	214.76 – 214.93
1996 May 11	Stromlo	9.17	735	214.82 – 215.21
1996 May 12	La Silla	3.98	156	215.77 – 215.93
1996 May 12	Stromlo	8.19	447	216.01 – 216.35
1996 May 13	La Silla	4.35	186	216.76 – 216.94
1996 May 13	Stromlo	12.72	856	216.82 – 217.35
1996 May 14	La Silla	2.09	88	217.76 – 217.84
1996 May 14	Stromlo	12.52	862	217.83 – 218.35
1996 May 15	La Silla	4.58	156	218.75 – 218.94
1996 May 15	Stromlo	6.33	303	219.09 – 219.35
1996 May 17	La Silla	4.08	121	220.76 – 220.93
1996 May 18	La Silla	4.16	159	221.76 – 221.93
1996 May 19	La Silla	3.82	184	222.74 – 222.90

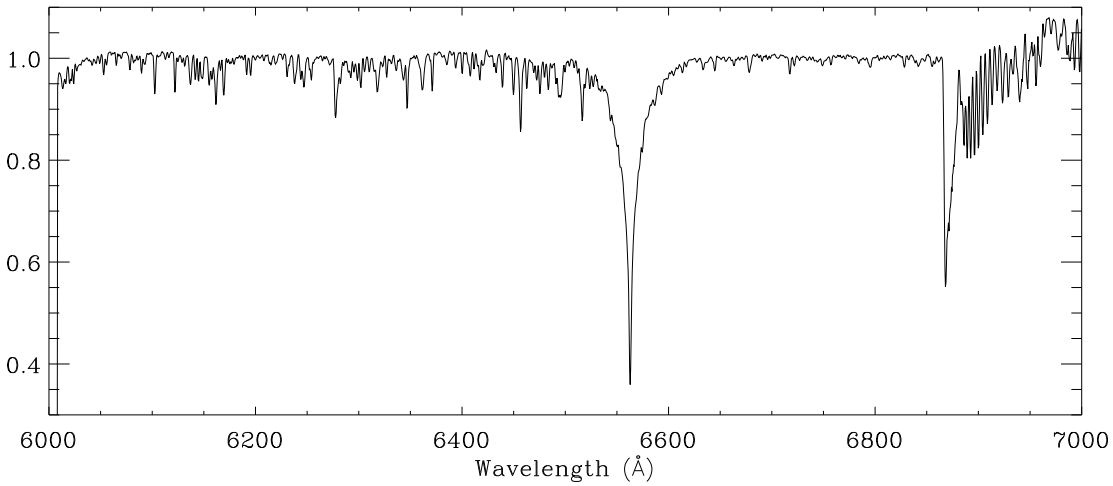

Figure 5.1 Template spectrum of α Cir from the Stromlo data set

5.3 Reductions

5.3.1 Extraction of spectra

IRAF procedures were used to reduce the data from 2D images to 1D spectra. These involved bias subtraction, flat-field division, and extraction of the orders including background scattered-light subtraction. Additionally the Stromlo data were corrected for non-linearities on the CCD image after bias subtraction (Chapter 3). This was necessary because the ratio between expected-counts and measured-counts varied by 7% from low-light levels to digital saturation. After correction, the data were linear to within 1%. The La Silla data were measured to be linear within 0.5%.

After reduction to the 1D stage, the spectra were fitted using the IRAF procedure, `continuum`, in which low points are excluded until a fit is obtained close to the continuum level. A third order polynomial fit was used for the Stromlo data and a second order fit for the La Silla data. For each data set, a template spectrum was obtained by averaging 25 high-quality spectra (Figure 5.1 or; for a close-up: Figures A.1–A.2).

5.3.2 Cross-correlations

The spectra obtained from Mt. Stromlo were divided into 89 unequal wavelength bands (Table 5.3). Except for the region containing Hα, the bands were non-overlapping and typically contained a few lines. The boundaries were chosen at places where two or three pixels were nearly at the same level (close to the continuum). In the case of Hα, we defined four bands of different widths, each centred on the core (band nos. 85–88). Only 66 of these bands were used from the La Silla spectra because of the different wavelength coverage.

A cross-correlation technique was applied to measure the Doppler shift of each band

in each spectrum, relative to the same band in the template spectrum. The following procedure was applied:

(i) a linear local continuum fit was applied across the band using the edge pixels;

(ii) the spectral band was linearly rebinned by a factor of 40 and 1.0 was subtracted such that the edge pixels were nearly zero;

(iii) a half-cosine filter was applied across 3 pixels at the edges so that there was a smooth transition between zero outside the band and nearly zero on the edge pixels;

(iv) the spectral band was cross-correlated (using Fast Fourier Transforms) with the band from the template spectrum, which had been processed in the same way;

(v) the peak of the cross-correlation function was found by fitting a quadratic to 9 points around the peak point.

With this procedure, we could measure shifts to within 0.02 pixels (400 m s^{-1}) in most of the spectra.

5.3.3 Velocity reference

The dominant cause of scatter in the velocity measurements is the global shifts of the light on the spectrograph. To correct for this, we have used the strong telluric O_2 absorption band around 6870Å as a velocity reference (band no. 80). The noise factors associated with using a telluric reference are the instability of the telluric atmospheric band and the changes in dispersion of the spectrograph, which affects the relative shift between a target band and the reference band. In our data, the variance of the noise when using the telluric reference was about one-tenth of the variance when using no reference, when measuring a target band about 300Å away from the telluric reference. Note that we were only interested in high-frequencies (periods less than 15 minutes) for this analysis, so that slow drifts of the spectrograph and an absolute measure of the radial velocity of the star were not important.

Figures 5.2–5.3 show the Stromlo and La Silla Hα velocity time-series, with the improvement in noise level that is made when a telluric band is used as a velocity reference.

This is particularly evident for the Hα Doppler shift, for which the noise is dominated by instrumental factors rather than photon-noise.

5.3.4 Time-series analysis

The time-series for the 88 different bands (not including the velocity reference) were high-pass filtered, and then cleaned for bad data points by removing any points lying outside ± 6.5 times the median deviation. Next, a weighted least-squares fitting routine was applied to each time series (using heliocentric time) to produce amplitude spectra.

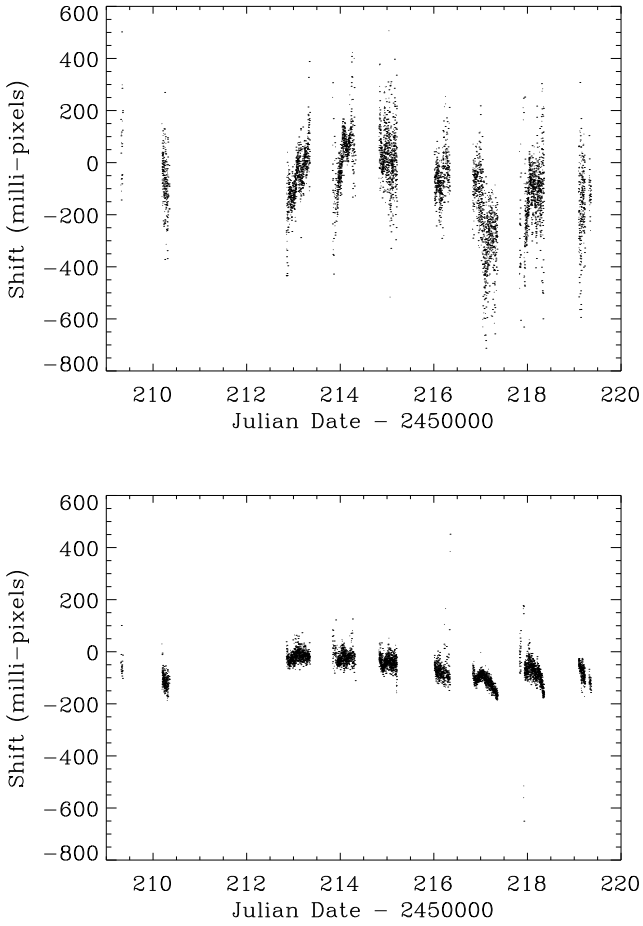

Figure 5.2 Shifts of the Hα line (band no. 88) from the Stromlo data set; **upper** using no reference; **lower** using a telluric band (no. 80) as a reference. Note that there are larger noise levels in the data at the beginning and end of each night. These points received lower weight in the time-series analysis.

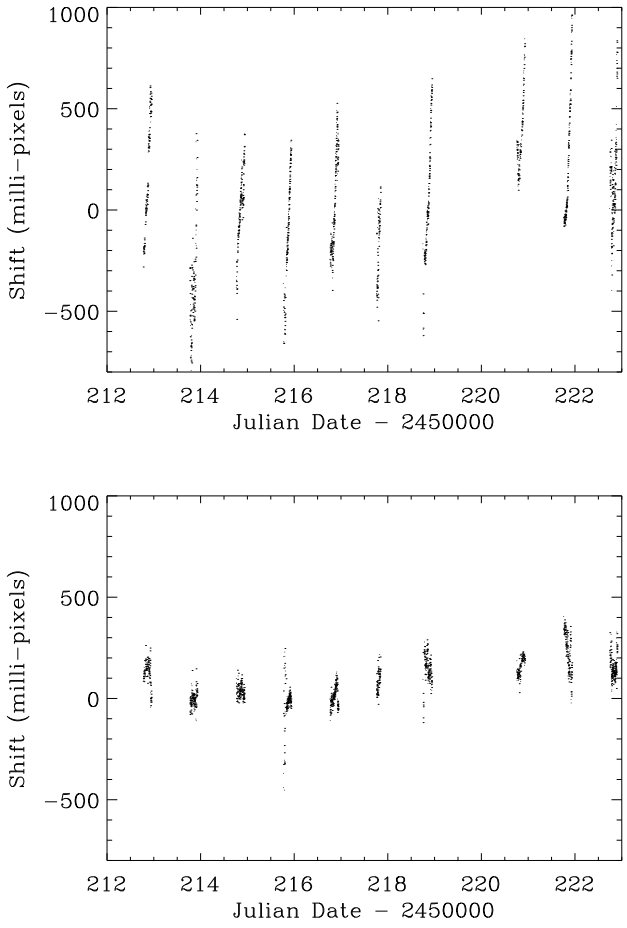

Figure 5.3 Shifts of the Hα line (band no. 88) from the La Silla data set; **upper** using no reference; **lower** using a telluric band (no. 80) as a reference

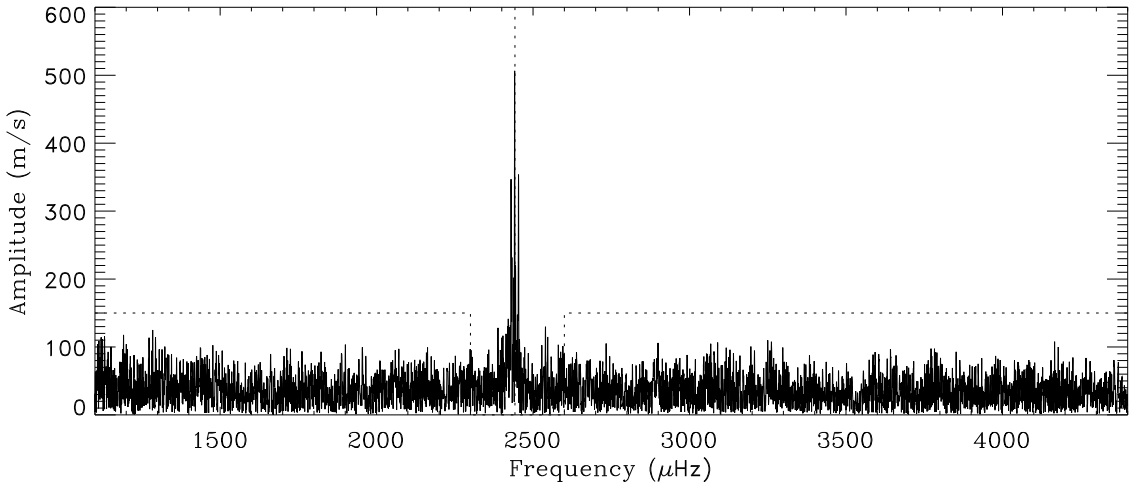

Figure 5.4 Amplitude spectrum for wavelength band no. 18, using the Stromlo data set. This figure clearly shows a peak at the principal frequency (2442 μHz), and shows the regions which were used to calculate the noise-level (1100–2300 μHz and 2600–4400 μHz). The side lobes to the main peak are caused by aliasing. The signal-to-noise ratio of the principal peak in this spectrum is 11.5.

5.4 Results on the principal mode

We have concentrated on using the Stromlo data for comparison between the different bands. This is because the La Silla data only covers bands 23–88 and also has a higher noise level per spectrum for the cross-correlation measurements. Also, we are only examining the principal pulsation mode with individual bands, therefore there is no need to use the dual-site combined data to reduce aliasing. This allows us to use the La Silla data to check the results obtained using the Stromlo data (Section 5.4.2).

Figure 5.4 shows the amplitude spectrum of a band with a strong peak at the principal photometric frequency, and Figures 5.5–5.6 show that the principal mode is evident even with quite low signal-to-noise ratios (4.4 and 3.1).

We measured the frequency of the principal mode to be 2442.05$\pm$0.02 μHz using the Stromlo data set, and 2442.02$\pm$0.03 μHz using the combined data from both sites. This is in agreement with photometric frequencies measured in the same time period by Don Kurtz (private comm., see Table 5.2) as part of an ongoing project of measuring frequency changes in roAp stars (Section 6 from Martinez & Kurtz 1995b, Kurtz et al. 1997). The two calculations from the photometric data, shown in Table 5.2, are over 130 days and 31 days. We have set our phase reference-point (t_0) to coincide with maximum light, using the first calculation. Our velocity phases are measured at this reference-point, with the convention that a phase of 0° represents maximum velocity (red-shift). For example, a phase of $-30°$ means that the velocity curve lags behind the light curve by 30°. Note that the second calculation indicates that there may have been some frequency changes during the time period of the first. If this is the case, then maximum light may not coincide with

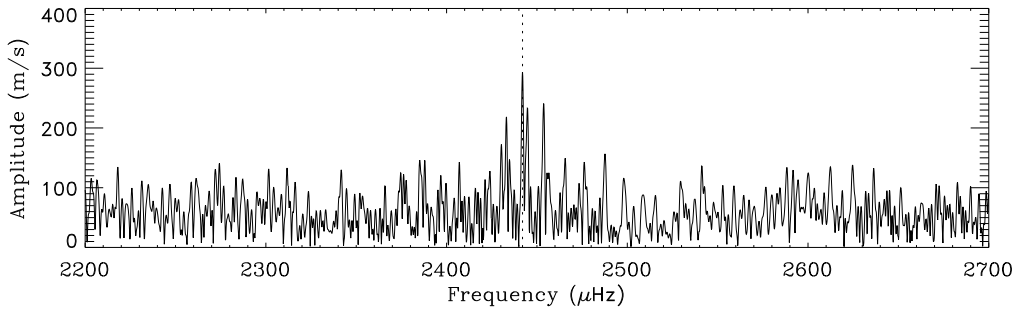

Figure 5.5 Amplitude spectrum for wavelength band no. 57. The signal-to-noise ratio in this spectrum is 4.4.

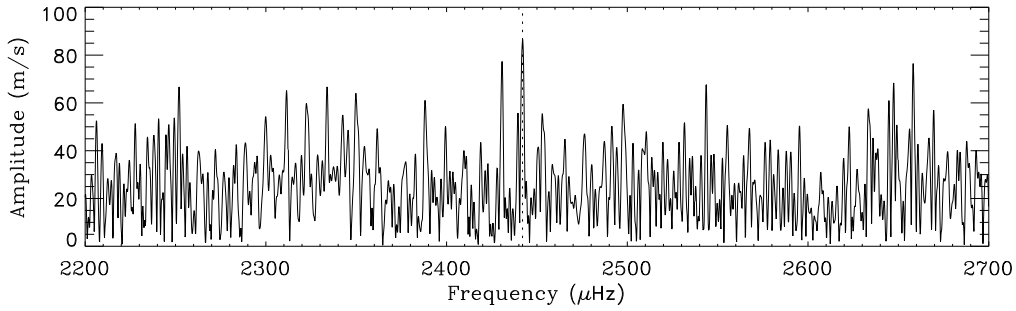

Figure 5.6 Amplitude spectrum for wavelength band no. 44. The signal-to-noise ratio in this spectrum is 3.1.

Table 5.2 Photometric amplitudes (Johnson B) and frequencies, of the principal mode, measured by Don Kurtz (private comm.). The reference-point (t_0) for the phase measurements is JD 2450215.07527, with the convention that a phase of 0° represents maximum light.

Julian dates -2450000	frequency (μHz)	amplitude (mmag)	phase (degrees)
142 – 272	2442.039±0.002	1.74±0.07	0.0±2.4
213 – 244	2442.022±0.011	1.63±0.12	15.3±7.3

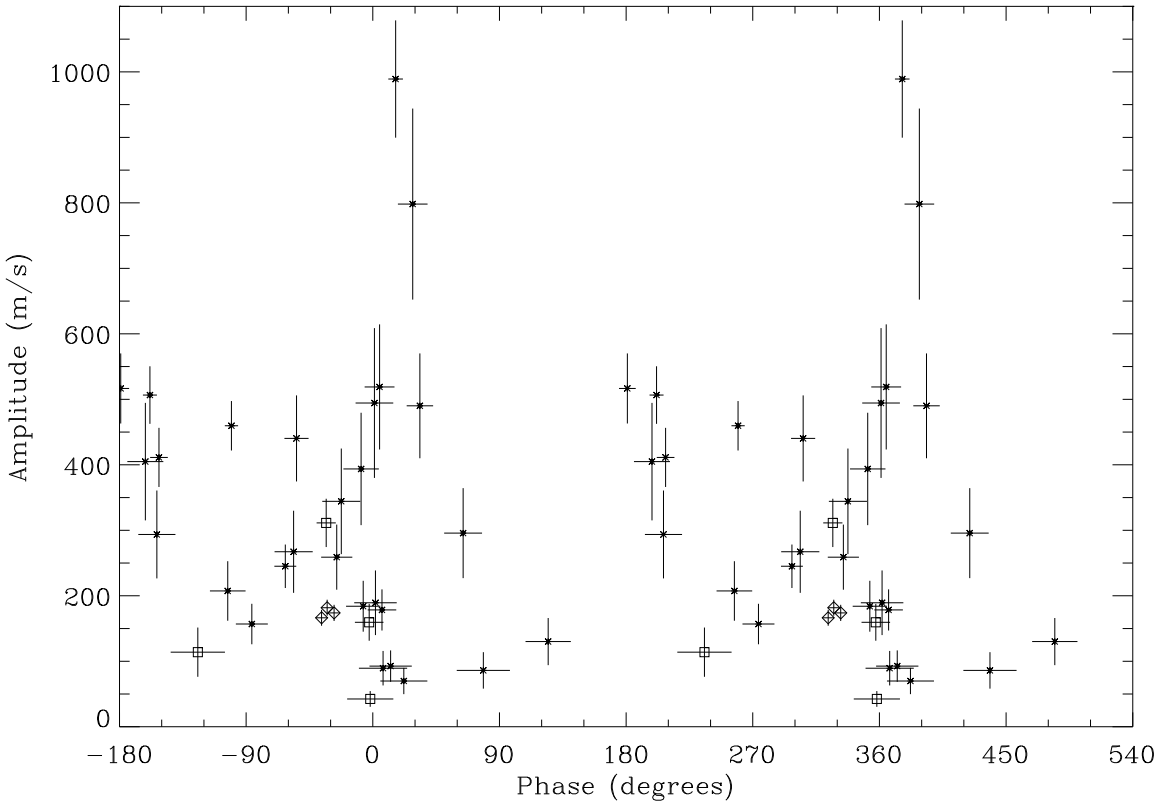

Figure 5.7 Amplitudes and phases of the principal pulsation mode in α Cir for different wavelength bands, using the Stromlo data. Only the bands with a signal-to-noise ratio greater than 3.0 are plotted. The diamonds represent three different wavelength bands across the Hα line, and the squares represent bands that contain some telluric lines. Note that the data are plotted twice for clarity.

the reference-point by up to $\sim$20° of a cycle.

We have measured the amplitude and phase of each time-series at 2442.03 μHz and estimated the rms-noise level by averaging over surrounding frequencies (1100–2300 μHz and 2600–4400 μHz). See Figure 5.4 for an example. The results are shown in Table 5.3.

5.4.1 Amplitude and phase variations

The amplitude and phase of the principal photometric mode vary significantly between different bands, with some bands that are pulsating in anti-phase with others. Figure 5.7 shows an amplitude vs. phase diagram for bands for which the signal-to-noise ratio in the amplitude spectrum is greater than 3.0. For these bands we can be sure that we have detected the principal pulsation and that the phase is reasonably well defined. For the uncertainty in the amplitude, we have used the rms-noise level directly. For the uncertainty

Table 5.3 Information on wavelength bands from α Cir showing amplitude and phase at 2442.03 μHz (from the Stromlo data set) – Part A

band no.	wavelengths (Å)	EW[a] (Å)	ampl. ($m\,s^{-1}$)	noise[b] ($m\,s^{-1}$)	S/N	phase[c] (deg.)	error[d] (deg.)	notes[e] on lines
00	6011.3 – 6018.2	0.143	136	60	2.2	171	26	Mn I
01	6019.1 – 6036.4	0.205	55	49	1.1	51	62	Fe I, Mn I, Si I
02	6037.7 – 6047.1	0.066	227	88	2.6	105	23	S I, Ce II, Fe II
03	6048.5 – 6050.6	0.017	56	72	0.8	—	—	Eu II, Co I
04	6051.9 – 6058.9	0.111	207	45	4.6	257	13	Cr II, Fe I, S I
05	6060.2 – 6073.6	0.083	93	52	1.8	24	34	Fe I, Cr II, Co I
06	6074.9 – 6084.8	0.074	189	49	3.8	2	15	Fe I, Co I, Fe II
07	6086.2 – 6095.6	0.108	411	45	9.1	208	6	Cr II, Co I, Si I
08	6099.4 – 6109.3	0.183	46	33	1.4	9	45	Ca I, Fe I
09	6110.7 – 6118.1	0.042	405	90	4.5	198	13	Fe II, Si I, Cr II, Co I
10	6120.5 – 6126.9	0.145	49	32	1.5	12	41	Ca I, Si I
11	6127.8 – 6133.8	0.054	71	63	1.1	70	62	Si I, Cr II, Fe I
12	6135.2 – 6139.7	0.134	11	39	0.3	—	—	Fe I
13	6141.0 – 6151.4	0.262	157	31	5.1	274	11	Fe II, Si I, Ba II
14	6153.3 – 6164.6	0.383	178	31	5.7	7	10	Ca I, Si I
15	6166.0 – 6171.5	0.133	60	30	2.0	140	30	Ca I, Fe I
16	6172.9 – 6181.8	0.046	26	65	0.4	—	—	Cr II, Fe II, Eu II
17	6184.1 – 6193.0	0.018	45	42	1.1	321	70	Fe I
18	6194.4 – 6197.5	0.055	507	44	11.5	202	5	Cr II, Si I
19	6198.8 – 6210.2	0.033	195	98	2.0	45	30	Ca II, Cr II, Fe I
20	6212.5 – 6217.5	0.055	140	82	1.7	243	36	Ti II, Fe I
21	6218.4 – 6223.4	0.048	394	86	4.6	352	13	Fe I, Ti II
22	6224.8 – 6228.3	0.016	64	125	0.5	—	—	Cr II, Fe I, V II
23	6229.2 – 6234.7	0.101	26	45	0.6	—	—	Fe I, Co I
24	6236.0 – 6241.5	0.159	105	41	2.6	336	23	Fe II, Si I
25	6242.9 – 6250.3	0.234	84	34	2.5	53	24	Si I, Fe II, Fe I
26	6251.7 – 6263.1	0.138	89	45	2.0	293	31	Fe I, Si I
27	6264.4 – 6274.8	0.045	226	77	2.9	341	20	Co I, Fe I
28	6275.7 – 6287.1	0.478	160	28	5.7	357	10	telluric, Co I
29	6288.9 – 6296.9	0.099	114	39	2.9	36	20	telluric, Fe I
30	6297.7 – 6308.1	0.202	68	29	2.4	308	25	Fe I, telluric
31	6309.0 – 6312.5	0.051	130	51	2.6	334	23	telluric, Si I
32	6313.4 – 6325.3	0.308	130	36	3.6	125	16	Ca I, Fe II, Fe I
33	6326.1 – 6333.6	0.106	460	38	12.2	260	5	Sm II(?), Fe II, Si I
34	6335.0 – 6338.5	0.048	119	56	2.1	17	28	Fe I, Cr II
35	6340.8 – 6350.7	0.319	89	26	3.4	7	17	Si II, Ca I
36	6352.1 – 6367.4	0.266	184	39	4.7	353	12	Ca I
37	6368.3 – 6373.7	0.143	35	29	1.2	287	55	Si II
38	6375.1 – 6387.9	0.090	440	66	6.7	306	9	Fe II, Fe I
39	6389.3 – 6397.2	0.077	100	49	2.0	297	30	Fe I
40	6398.6 – 6402.1	0.066	86	38	2.3	20	26	Fe I
41	6404.5 – 6412.9	0.132	78	30	2.5	14	23	Fe I
42	6414.3 – 6423.2	0.210	245	33	7.4	298	8	Fe II, Fe I, Co I

[a] Approximate total equivalent-width of lines in band, relative to local fit across band.
[b] rms-noise estimated from amplitude spectrum using 1100–2300 μHz and 2600–4400 μHz.
[c] Phase is calculated with respect to a reference-point (t_0) at JD 2450215.07527, and the convention is that a phase of 0° represents maximum velocity (red-shift).
[d] Error in the phase is taken to be arcsin (rms-noise/amplitude).
[e] Notes on each band giving the probable dominating absorption lines derived from synthetic spectra supplied by Friedrich Kupka (private comm.).

Table 5.4 Information on wavelength bands from α Cir showing amplitude and phase at 2442.03 μHz (from the Stromlo data set) – Part B

band no.	wavelengths (Å)	EW[a] (Å)	ampl. (ms^{-1})	noise[b] (ms^{-1})	S/N	phase[c] (deg.)	error[d] (deg.)	notes[e] on lines
43	6424.6 – 6435.4	0.152	69	47	1.5	332	43	Fe II, Fe I
44	6436.8 – 6441.3	0.132	86	28	3.1	79	19	Ca I, Eu II
45	6442.2 – 6444.7	0.013	120	95	1.3	100	52	Si I, Fe II, Co I
46	6448.1 – 6452.6	0.146	39	26	1.5	83	42	Ca I, Co I
47	6453.5 – 6460.4	0.363	70	20	3.5	22	17	Fe II, Ca II
48	6461.8 – 6465.3	0.100	93	24	3.9	13	15	Ca I
49	6468.1 – 6478.0	0.218	29	30	1.0	—	—	telluric, Ca I
50	6478.9 – 6488.3	0.152	114	38	3.0	236	19	telluric, Fe II
51	6489.7 – 6501.5	0.422	69	33	2.1	229	28	Ca I, Fe I, Ti II, Ba II
52	6502.4 – 6509.9	0.012	88	84	1.0	174	73	telluric, Fe I
53	6511.2 – 6521.1	0.395	49	23	2.1	20	29	Fe II, telluric
54	6522.5 – 6529.0	0.110	311	37	8.4	327	7	telluric, Si I
55	6530.3 – 6538.8	0.078	86	60	1.4	6	45	telluric, S I
56	6585.2 – 6589.7	0.055	25	88	0.3	—	—	Fe II, C I
57	6591.1 – 6596.5	0.049	294	67	4.4	207	13	Fe I
58	6597.9 – 6607.3	0.015	989	90	11.0	16	5	Sm II(?), Ti II
59	6608.7 – 6620.0	0.047	156	56	2.8	293	21	Y II, Co I, Fe I
60	6623.9 – 6640.6	0.100	296	69	4.3	64	13	Fe I, Si I, Co I
61	6642.0 – 6652.9	0.066	259	50	5.2	334	11	Eu II
62	6654.2 – 6658.7	0.021	139	189	0.7	—	—	C I, Ca I
63	6660.1 – 6674.9	0.084	199	67	3.0	351	20	Fe I, Cr I, Si I
64	6676.3 – 6682.2	0.100	517	54	9.6	181	6	Fe I, Ti II
65	6683.1 – 6714.1	0.042	267	63	4.3	304	14	Al I, Fe I, Ca I
66	6715.4 – 6719.5	0.062	56	38	1.5	302	43	Ca I
67	6720.8 – 6724.3	0.030	147	69	2.1	213	28	Si I
68	6725.2 – 6746.4	0.040	519	96	5.4	5	11	S I, Fe I
69	6747.3 – 6754.2	0.044	214	107	2.0	324	30	S I, Fe I, Si I
70	6755.6 – 6759.1	0.031	139	78	1.8	272	34	S I
71	6760.5 – 6779.2	0.013	95	112	0.8	—	—	Co I, Si I, Ni I
72	6781.5 – 6788.0	0.030	798	146	5.5	28	11	Ti II
73	6788.9 – 6798.3	0.067	490	80	6.1	33	9	Y II
74	6800.6 – 6823.8	0.021	344	81	4.3	338	14	Co I, Fe I, Si I
75	6826.6 – 6830.1	0.042	171	58	3.0	258	20	Ti II, C I, Fe I
76	6831.5 – 6834.5	0.013	177	149	1.2	59	58	Y II
77	6835.9 – 6850.2	0.153	78	88	0.9	—	—	Fe I
78	6851.6 – 6859.0	0.065	64	56	1.1	138	61	Fe I, Si I
79	6860.4 – 6863.9	0.018	494	114	4.3	1	13	Si I, Fe I, Fe II
80	6864.8 – 6881.0	3.605						telluric reference
81	6881.9 – 6902.1	1.958	36	14	2.5	318	23	telluric
82	6903.0 – 6920.2	0.832	30	10	3.0	263	19	telluric
83	6921.6 – 6966.2	2.424	42	12	3.5	358	16	telluric
84	6968.6 – 7007.4	1.184	45	21	2.2	322	27	telluric
85	6522.0 – 6607.8	10.398	168	13	13.1	325	4	Hα
86	6538.2 – 6590.2	7.774	174	12	14.1	332	4	Hα
87	6545.5 – 6578.4	5.486	166	12	13.7	324	4	Hα
88	6554.3 – 6571.1	2.931	182	12	14.9	328	4	Hα

[1,2,3,4,5] See Table 5.3.

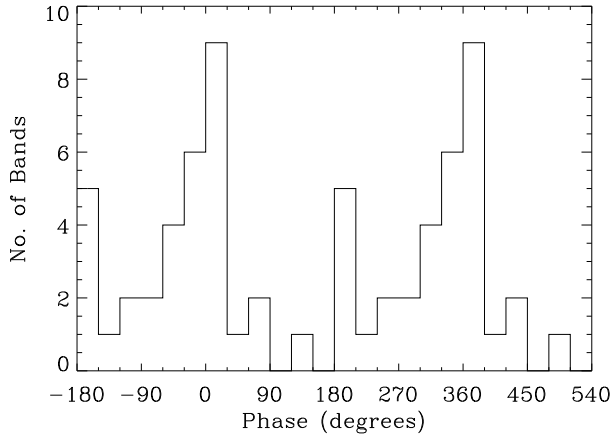

Figure 5.8 Histogram of the data in Figure 5.7 in phase bins of 30°. In total, 33 bands are plotted, with only one band across Hα included.

in the phase, we have used simple complex arithmetic to find the maximum change in phase that a rms-noise vector could induce i.e. arcsin (rms-noise/amplitude).

Figure 5.8 shows a histogram of the phases of the principal mode. Most bands have phases that lie between $-60°$ and 30° but there is also a group of five bands with phases between 180° and 210°. We suggest that these two groups might be associated with two sections of the atmosphere either side of a pulsational node (zero-point). However, there is more variation in the phases than can be accounted for purely by using a standing wave model. Perhaps there is also a travelling component to the pulsational wave in the star's atmosphere. Another possibility is that we are seeing asymmetric temperature (equivalent-width) changes that create apparent Doppler shifts and therefore produce a variety of phases. For example, consider two lines at different wavelengths which are blended. If a temperature change causes the relative strength of the two lines to change then a pseudo-Doppler shift may be measured from the blended profile.

The line identification for the different bands (Table 5.3) is only an approximate analysis based on synthetic spectra (Friedrich Kupka, private comm.) using recently derived abundances (Kupka et al. 1996). Nearly all the bands that we have measured are composed of blended lines in our spectra. Therefore it has been difficult to determine if there is a pattern associating the line-type with the measured amplitude of the pulsation. One noticeable pattern is that the largest amplitudes occur only in the weaker lines, this is seen from a plot of amplitude vs. total equivalent width of the band (Figure 5.9). Possibly this is because weaker lines are more likely to be formed in a narrower section of the star's atmosphere and therefore phase smearing between different parts of a pulsation wave is minimised. Kanaan & Hatzes (1998) have also found that the velocity amplitude tends to be higher (up to 1000 m s^{-1}) in the weaker lines of the roAp star γ Equ.

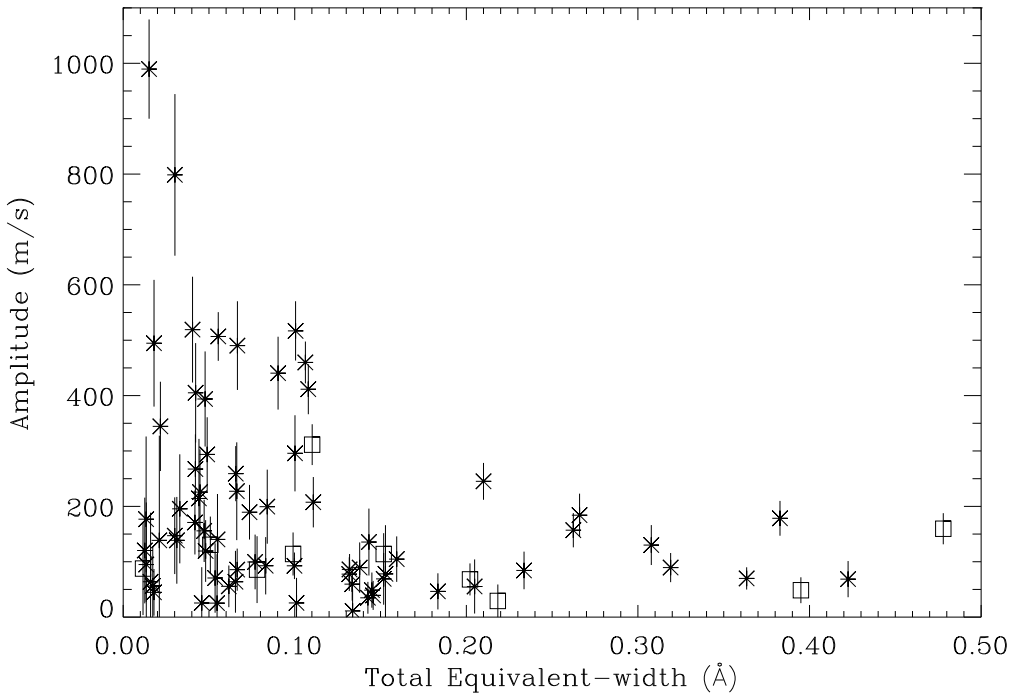

Figure 5.9 Amplitude of the principal pulsation mode as a function of total equivalent-width for bands 0–79, using the Stromlo data. The squares represent bands that contain some telluric lines.

5.4.2 Comparing the data sets

The amplitude vs. phase diagram for the La Silla data is shown in Figure 5.10. The amplitudes and phases measured from the two data sets are in complete agreement, at the 2σ level, with the exception of bands 58 and 79. These have larger amplitudes when measured using the La Silla data (Table 5.5). Amplitude variation is not unexpected since the photometric amplitude varies as a function of rotation phase of the star (rotation period 4.48 days, Kurtz et al. 1994b). The La Silla time-series may sample the rotational phases of the star in such a way to produce a larger amplitude on average. Other possible reasons are that the bands are not exactly equal for the two data sets (they are slightly out of alignment by about 0.5 to 1 pixel) and that the dispersions are different (see Section 5.2).

Table 5.5 Comparison of the large velocity amplitude bands between the Stromlo and the La Silla data sets

Band no.	Stromlo measurement	La Silla measurement
58	$990\pm\ 90\,\mathrm{m\,s^{-1}}$	$1660\pm280\,\mathrm{m\,s^{-1}}$
72	$800\pm150\,\mathrm{m\,s^{-1}}$	$960\pm400\,\mathrm{m\,s^{-1}}$
79	$490\pm110\,\mathrm{m\,s^{-1}}$	$1370\pm380\,\mathrm{m\,s^{-1}}$

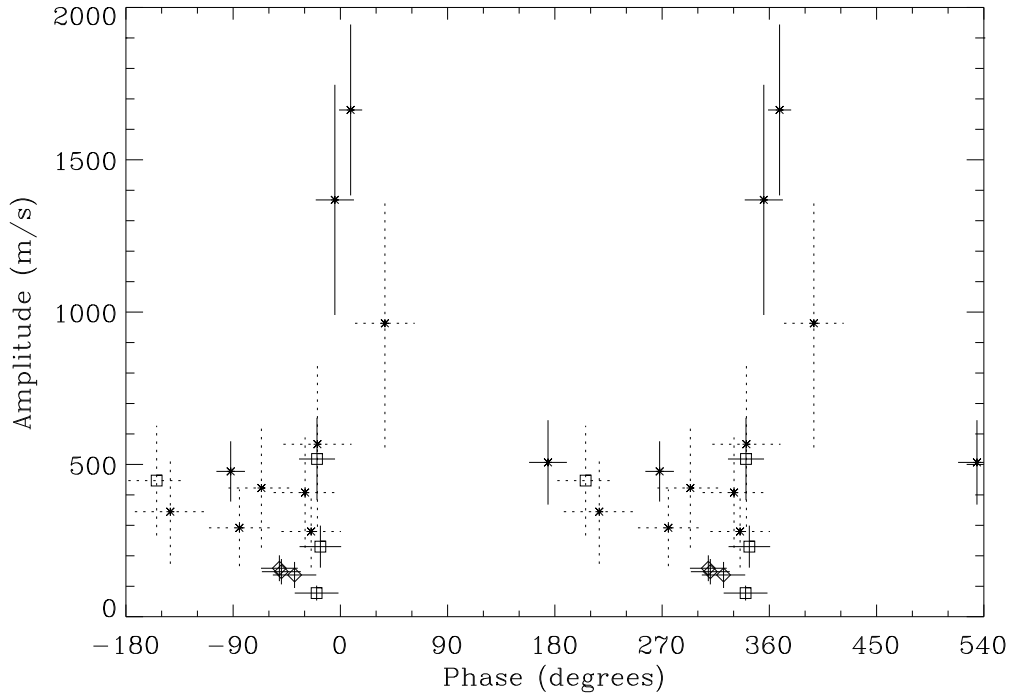

Figure 5.10 Amplitudes and phases of the principal pulsation mode for different bands, using the La Silla data (which covers bands 23–88). This figure is similar to Figure 5.7 except, additionally the bands with a signal-to-noise ratio between 2.0 and 3.0 are plotted (with dotted lines). Also note that the amplitude scale extends to $2000\,\mathrm{m\,s^{-1}}$ rather than $1100\,\mathrm{m\,s^{-1}}$.

5.5 Discussion and conclusions

5.5.1 Techniques

We have shown that it is possible to obtain high-precision velocity measurements with medium-dispersion spectrographs using telluric lines as a reference. For the Doppler shift of the Hα line, we have obtained a noise level of 500 m s^{-1} per spectrum from Mt. Stromlo and 900 m s^{-1} per spectrum from La Silla. These measurement are not limited by photon-noise, so the difference in precision between the two sites must be due to either the instrument (coudé vs. Cassegrain) or the telluric reference. Given that Mt. Stromlo (750m) is situated at a lower altitude than La Silla (2400m), we note that a possible advantage of low altitude sites is that the telluric lines are more stable. This is plausible since the lines will be stronger, and temperature and velocity changes will be averaged over a longer distance in the Earth's atmosphere.

We chose the strongest telluric feature (band 80) as our velocity reference. The total equivalent-width (EW) of the metal lines within this band was estimated (using the synthetic spectra) to be approximately 2 percent of the total EW of the band. Other bands (81–84), which are also dominated by telluric lines, show low-amplitude oscillation signals with signal-to-noise ratios from 2.2 to 3.5. This is not surprising since these bands have about 6%, 12%, 9% and 23% of their total EW coming from metal lines.

5.5.2 Velocity amplitudes

Schneider & Weiss (1989) set an upper limit of 100 m s^{-1} for radial velocity variations in α Cir but this was set assuming no amplitude and phase differences between lines. From their Table 4, it can be seen that only from lines at 6462.6Å and 6494.99Å can amplitudes above 100 m s^{-1} be ruled out. This is in agreement with our measured amplitudes in bands 48 and 51 which are 93 ± 24 m s^{-1} and 69 ± 33 m s^{-1} respectively.

We cannot compare our results directly with the upper limit of only 18 m s^{-1} set by Hatzes & Kürster (1994), but our results show that such a low limit could be set if there were only lines with low amplitude, and perhaps different phases, in the region used by them (5365–5410Å). Kanaan & Hatzes (1998) have measured radial velocity variations in γ Equ in a similar wavelength region (5373–5394Å) and find an average amplitude of 30 m s^{-1}. In conclusion, our measured amplitude differences between bands are consistent with previous upper limits on velocity variations in α Cir and are comparable to the amplitude differences found in γ Equ by Kanaan & Hatzes (1998). Furthermore, our data lend support to the detection by Belmonte et al. (1989) of a velocity amplitude of 1000 m s^{-1} in α Cir.

5.5.3 Probing the atmosphere

The photometry of roAp stars has revealed a steep decline of pulsational amplitude with increasing wavelength. Matthews et al. (1990, 1996) have attributed this to the wavelength dependence of limb-darkening. They have determined limb-darkening coefficients

from their amplitude measurements of HR 3831. However, Medupe & Kurtz (1998) suggest that limb-darkening is too small an effect to explain the observed decline. Instead, they account for the decline by the change in pulsational temperature amplitude with depth in the stars, α Cir and HR 3831. This result would imply a surprisingly small radial node separation in the atmosphere of roAp stars (Matthews 1997). The amplitude and phase variations presented in this chapter (see also Viskum et al. 1998a) suggest the same, with a radial-node situated in the atmosphere of α Cir. Matthews (1997) suggested an alternative interpretation, where ions are grouped either side of a horizontal node on the surface. Since we can find no simple pattern associating ion type with amplitude or phase, we argue that the phase differences are probably caused by differing formation depths and therefore there is a radial-node in the atmosphere.

Three bands (Table 5.5) have a particularly large amplitude in one or both data sets. It could be these bands contain elements that are located in spots on the surface of the star, near a pole of the dipole pulsation, which is why their velocity amplitude is larger. The argument against this hypothesis is that there is no one element that is a dominating factor in all three bands. However, we can not rule out surface inhomogeneities as a factor contributing to the amplitude and phase variations.

5.5.4 Further work

A time-series of high-resolution spectra would be invaluable in explaining the complete range of amplitudes and phases discovered in α Cir. With our results, we can not rule out significant contributions from blending effects to the amplitudes and phases of different bands. However, with our data set from May 1996 we can look for Hα line profile variations. In particular, measuring the width and velocity amplitude at different depths in the Hα line (Chapter 6).

Eventually, spectroscopy of α Cir combined with modeling, should be able to map the shape of the pulsation wave in the atmosphere of the star.

Chapter 6

The bisector and equivalent-width of the Hα line in the roAp star α Circini

The content of this chapter was published in paper Baldry et al. (1999), and is a continuation of the analysis of α Cir from Chapter 5, in collaboration with the same co-authors.

6.1 Introduction

Previous observations of α Cir in photometry have shown that it has one dominant pulsation mode with a period of 6.825 min ($f = 2442\,\mu$Hz; Kurtz et al. 1994b, hereafter KSMT). Medupe & Kurtz (1998) observed that the amplitude decreased with increasing wavelength, from 2.71 ± 0.18 mmag in Johnson U (3670Å) to 0.41 ± 0.13 mmag in I (7970Å). They proposed that the rapid decline of photometric amplitude with wavelength could be explained by a decrease in the temperature amplitude of the pulsation with atmospheric height.

In Chapter 5, we showed that the velocity amplitude and phase of the principal pulsation mode in α Cir varied significantly from line to line. However, it was difficult to interpret the data because of blending effects. In particular, there was evidence for a velocity node in the atmosphere of α Cir but it was uncertain whether the node was horizontal or radial. In this chapter we look at the Hα line in more detail using the same set of observations, taken during two weeks in May 1996. These observations comprise 6366 intermediate-resolution spectra taken using the 74-inch (1.88-m) Telescope at Mt. Stromlo, Australia and the Danish 1.54-m Telescope at La Silla, Chile (see Section 5.2 for further details).

We first examined how the Hα profile changed during the principal pulsation cycle, in terms of the bisector at different heights in the line (preliminary results were presented by Baldry et al. 1998a). In this way, the effect of the velocity on the profile could be analysed. To quantify the temperature effect, we measured the equivalent-width (EW) amplitude of the principal mode in filters of varying width and measured pixel-by-pixel intensity changes across the Hα region of the spectrum. Finally, we defined an observable quantity (related to the EW of Hα) which had a high signal-to-noise ratio for the principal pulsation. Using this observable, some of the weaker modes in α Cir were detected.

6.1.1 General properties of α Cir

Before we discuss the pulsation of α Cir, we will review the general properties in the light of a recent spectral analysis (Kupka et al. 1996) and the Hipparcos parallax measurement (ESA 1997). The distance of 16.4 ± 0.2 pc (parallax of 61.0 ± 0.6 mas), combined with a bolometric correction of -0.12 ± 0.02 ($M_{\mathrm{bol},\odot} = 4.64$, Schmidt-Kaler 1982), gives $M_{\mathrm{bol}} = 2.00 \pm 0.04$ ($L = 11.4 \pm 0.4 L_\odot$). From this luminosity and the temperature of $T_{\mathrm{eff}} = 7900 \pm 200$ K (derived by Kupka et al.), we obtain $R = 1.81 \pm 0.11 R_\odot$ (angular diameter of 1.03 ± 0.07 mas). Combining this radius with $\log g = 4.2 \pm 0.15$ (Kupka et al.) gives a mass of $M = 1.9 \pm 0.6 M_\odot$. The rotation period of 4.48 days (derived by KSMT) and the radius means that $v_{\mathrm{rot}} = 20.4 \pm 1.2$ km s^{-1}. Using $v \sin i = 13 \pm 1$ km s^{-1} (Kupka et al.), the inclination of the rotation axis to the line of sight is then $i = 40^\circ \pm 5^\circ$. This is an improvement on the estimate given by KSMT due to more recent results.

6.1.2 The oblique pulsator model

In some roAp stars, including α Cir, the amplitude of the oscillations has been observed to be modulated by the rotation period of the star. In particular, the amplitude is at a maximum when the observed magnetic field strength is also at a maximum. This led to the oblique pulsator model (Kurtz 1982), in which an roAp star pulsates non-radially with its pulsation axis aligned with the magnetic axis. The amplitude modulation comes from the inclination of the pulsation axis with respect to the rotation axis. Therefore different aspects of a non-radial mode are viewed as the star rotates. The oblique pulsator model predicts that, in the Fourier domain, a frequency of mode ℓ is split into 2ℓ +1 frequencies. The frequency splitting is exactly equal to the rotation frequency, and the relative amplitudes are determined by both the inclination of the rotation axis to our line of sight (i) and the angle between the rotation axis and the pulsation axis (β). Most of the review papers mentioned in Section 5.1 discuss the oblique pulsator model, a refinement of which is given by Shibahashi & Takata (1993).

The principal pulsation mode in α Cir is believed to be a pure oblique dipole mode ($\ell = 1$). KSMT observed a 21 percent full-range variation of the amplitude during the rotation period. This variation implies that $\tan i \tan \beta = 0.21 \pm 0.01$ (see Section 4.1 from KSMT). Using our new estimate of i (see Section 6.1.1), we get $\beta = 14° \pm 3°$. This means that the inclination angle of the pulsation axis to the line of sight (α) varies between 26° and 54° during the rotation cycle.

6.2 General data reductions

Extraction of spectra and continuum fitting were done using IRAF procedures (see Section 5.3.1). We made a number of types of measurements on the reduced spectra, including bisector line-shift measurements which are described in Section 6.2.2. The time series analysis of these is explained in Section 6.2.3 and is also applicable to other measurements, which are described later in the paper. Since the continuum fit is more critical than for Chapter 5, we first describe this procedure in more detail.

6.2.1 Continuum fitting

The IRAF procedure `continuum` was applied to each spectrum in our data, using the following parameters: sample=@list, naverage=1, function=legendre, order=3/4 (2nd/3rd order polynomial), low_rej=2, high_rej=4, niterate=20/25, grow=0.

Initially, a sample of about 1400 points from each spectrum was used to make a least-squares polynomial fit — 3rd order for the Stromlo data and 2nd order for the La Silla data. A higher order fit was used for the Stromlo data because the continuum shape was less stable. Next, points below 2σ and above 4σ from the fit were excluded from the next fit. The lower cutoff was used to exclude some absorption lines and the upper cutoff only excluded cosmic ray events. The fitting and excluding routine was repeated 20 to 25 times or in most cases until no more points were excluded. In the final fit, about 1000

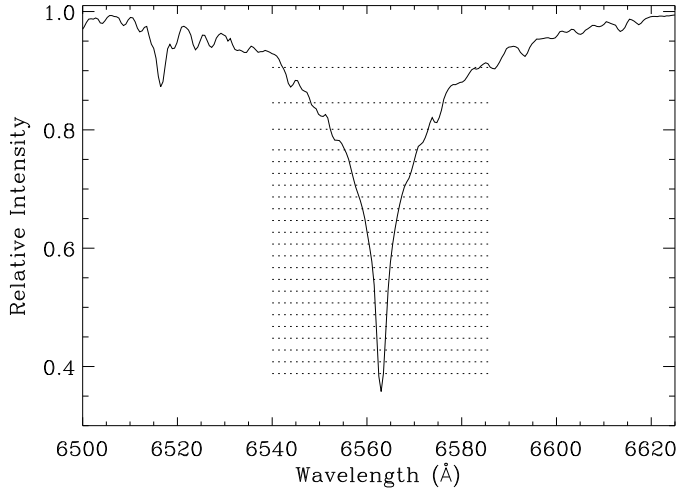

Figure 6.1 The Hα line in α Cir. The dotted lines divide the 22 contiguous sections.

points were included, with none being within 50Å of the core of the Hα line. Not all absorption lines were excluded from the final fit since there is very little real continuum at the resolution of our data ($\sim$1.5Å). The real continuum level in each fitted spectrum was around 1.005–1.010, depending on the wavelength. Therefore, we have scaled the spectra so that the continuum level is $\sim$1.00 in the Hα region of the spectrum. The level varied slightly from spectrum to spectrum, with a standard deviation of about 0.001.

6.2.2 Bisector measurements of Hα

The Hα line in each spectrum was divided into 22 contiguous horizontal sections (see Fig. 6.1 and Cols. 1–4 of Table 6.1) and two extra sections for checking. For each section, the average wavelength of each side of the absorption line was measured, and a bisector line-shift (average position of the two sides) was calculated. We have used a telluric O_2 band as a Doppler shift reference (see Section 5.3.3 for details).

An alternative method was also tried in which a least-squares fit was made to the position of each side of the line. A template spectrum was used to define the shape of the line and was shifted from side to side until a best fit was obtained. This method produced similar results and noise levels to the method of calculating the average wavelength, but the computational time was longer.

6.2.3 Time-series analysis

For each section of the Hα line, the above analysis produced a time series of 6366 bisector line-shift measurements (4900 from Stromlo, 1466 from La Silla). Each time series was high-pass filtered and then cleaned for bad data points by removing any points lying outside ± 6.5 times the median deviation. Typically, about 100 data points were removed.

Next, a weighted least-squares sine-wave fitting routine was applied (using heliocentric time) to produce amplitude spectra.

For the analysis of the principal pulsation mode in α Cir, we have measured the amplitude and phase of each time series at 2442.03 μHz and estimated the rms-noise level by averaging over surrounding frequencies, 1100–2300 μHz and 2600–4400 μHz. The phases are measured at a temporal phase reference point (t_0) with the convention that a phase of 0° represents maximum of the observable. t_0 was chosen to coincide with maximum light using data supplied by Don Kurtz (private communication); see Table 5.2 for details. For the phase error, we have used simple complex arithmetic to find the maximum change in phase that an rms-noise vector could induce, i.e., arcsin (rms-noise/amplitude).

6.3 Bisector velocities

6.3.1 Results

We have assumed that the bisector line-shift measurements represent velocities in the star. The velocity amplitudes and phases of the principal mode at different heights in the Hα line are shown in Fig. 6.2 and Table 6.1. The results describe the oscillations in the bisector about the mean position at each height (see Fig. 6.3 for the bisector shape). From 0.4 to 0.8 in the line, the amplitude decreases from 300 m s^{-1} to zero and then increases again, with a change in phase of $-140°$. Note that there is good agreement between the Stromlo and La Silla data sets, which were analysed separately for Fig. 6.2. This gives us confidence that the observed variations are intrinsic to the star.

In Chapter 5, the Hα velocity amplitude and phase were measured to be $\sim$170 m s^{-1} and $\sim$330° using a cross-correlation method. This is compatible with our bisector velocity results since the cross-correlation measurement would be dominated by the steepest part of the Hα profile, near the core.

To further illustrate the behaviour of the Hα bisector, in Fig. 6.4 we show the bisector velocity as a function of time and height. The horizontal axis covers two cycles of the principal pulsation mode ($P = 6.825$ min). Only sections 0–19 are shown (see Table 6.1), since above a height of 0.8 the measurements are significantly affected by line blends (see Section 6.3.2). The figure clearly illustrates that the higher sections are pulsating nearly in anti-phase with the lower sections, and that the velocities of the middle sections are close to zero. Since the bisector velocity reflects the velocity at different heights in the atmosphere, these results support the hypothesis, suggested in Chapter 5, of a radial node in the atmosphere of α Cir.

6.3.2 Blending considerations

We attribute the velocity node (at $\sim$0.65) and the phase jump between 0.4 and 0.8 to Hα line-formation effects, although there is some uncertainty as to how much blending affects the results between heights 0.7 and 0.8. Above a height of 0.8, the results are significantly affected by line blending. In order to identify any metal lines in the wings of Hα, we

Table 6.1 Amplitudes and phases of the principal pulsation mode for the bisector velocity at different heights in the Hα line. The line was divided into 22 non-overlapping and two extra horizontal sections. For the results in this table, the Stromlo and the La Silla data sets were combined.

section no.	low cutoff[a]	high cutoff[a]	mean width[b] (Å)	velocity ampl.[c] ($m\,s^{-1}$)	velocity noise[d] ($m\,s^{-1}$)	S/N	velocity phase[e] (°)	phase error[f] (°)
0	0.39	0.41	1.1	264	19	14.1	333	4
1	0.41	0.43	1.4	256	15	17.4	328	3
2	0.43	0.45	1.7	279	15	18.8	327	3
3	0.45	0.47	1.9	277	15	18.7	327	3
4	0.47	0.49	2.2	257	15	16.9	328	3
5	0.49	0.51	2.5	227	15	14.7	330	4
6	0.51	0.53	2.7	193	16	11.9	333	5
7	0.53	0.55	3.0	176	18	9.6	331	6
8	0.55	0.57	3.5	125	18	6.9	331	8
9	0.57	0.59	3.9	43	18	2.4	303	24
10	0.59	0.61	4.6	54	20	2.8	255	21
11	0.61	0.63	5.4	55	21	2.6	283	22
12	0.63	0.65	6.2	43	23	1.9	334	32
13	0.65	0.67	7.1	26	25	1.0	304	73
14	0.67	0.69	8.3	64	29	2.2	205	27
15	0.69	0.71	9.7	25	33	0.8	—	—
16	0.71	0.73	11.6	254	37	6.8	195	8
17	0.73	0.75	13.0	340	34	10.1	192	6
18	0.75	0.77	14.4	310	36	8.5	191	7
19	0.77	0.80	19.0	181	45	4.0	215	14
20	0.80	0.85	23.9	514	44	11.7	45	5
21	0.85	0.91	32.2	208	56	3.7	18	16
22	0.70	0.72	10.5	86	36	2.4	200	25
23	0.76	0.78	15.3	221	45	4.9	195	12

[a] Boundary of the section in relative intensity.
[b] Approximate mean width of the line at the height of the section.
[c] Amplitude measured at 2442.03 μHz.
[d] rms-noise estimated from amplitude spectrum using the regions 1100–2300 μHz and 2600–4400 μHz.
[e] Phase measured at 2442.03 μHz, with respect to a reference-point (t_0) at JD 2450215.07527, with the convention that a phase of 0° represents maximum of the observed variable.
[f] Error in the phase is taken to be arcsin (rms-noise/amplitude).

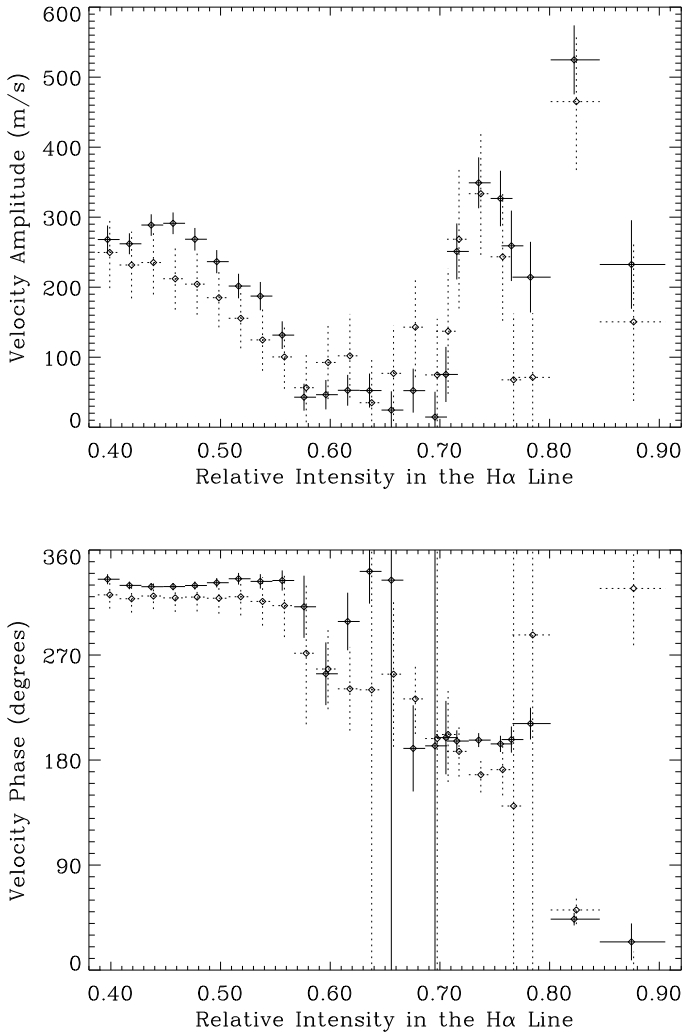

Figure 6.2 Amplitudes and phases of the principal pulsation mode for the bisector velocity at different heights in the Hα line. Points with solid lines represent the Stromlo data and points with dotted lines represent the La Silla data. For each measurement, the vertical line is an error-bar while the horizontal line shows the extent of the section in the Hα line.

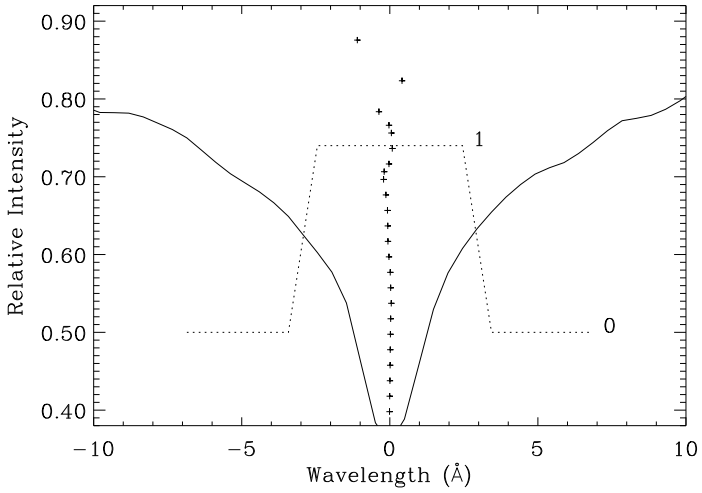

Figure 6.3 The Hα line in α Cir. The crosses show the mean position of the bisector. The wavelength is measured with respect to the centre of the line. The dotted line shows the shape of trapezium filter no. 2, which is used for the equivalent-width measurements. It is plotted using a different vertical scale.

used a synthetic spectrum calculated by Friedrich Kupka (private communication) and high-resolution spectra of α Cir taken in 1997 March (coudé echelle, 74-inch Telescope, Mt. Stromlo). From this, we determined that most of the lines blended with the Hα profile from 6540Å to 6585Å are telluric, including all those below a height of 0.7 in the Hα line (see Appendix A.1, Figure A.3 and Table A.1 for more details).

At height 0.82, the anomalously large velocity amplitude is probably caused by the metal absorption line Sr I 6550.2Å, with the possibility that Fe I 6575.0Å also contributes. Since metal lines can have amplitudes as large as $1000\,\mathrm{m\,s^{-1}}$ (Chapter 5), this can explain the large bisector velocity seen at this height. At height 0.88, the amplitude is similar to that between 0.72 and 0.79 but the phase is anomalous. This measurement is affected by various metal and telluric lines, in particular a metal line blend including Mg II 6546.0Å and Fe I 6546.2Å.

Below a height of 0.8, we expect any absorption features to have less impact on the bisector velocity due to the increasing steepness of the Hα profile. However, there is a metal line Fe I 6569.2Å in addition to a few telluric lines that affect the Hα profile between 0.7 and 0.8. This Fe I feature affects the bisector measurements between 0.71 and 0.76. Therefore, it probably causes the jump in amplitude near height 0.72 shown in Fig. 6.2. It cannot explain why all the bisector velocities from heights 0.67–0.80 have phases around 190°–200°, but it does lower the significance of the phase jump between the core and this part of the wings. We speculate that without this Fe I feature, the Hα bisector velocity amplitude would increase steadily from 0.70 to 0.77.

In summary, we believe features in Fig. 6.2 below height 0.7 reflect genuine effects in the Hα profile, while those above 0.8 are dominated by metal and telluric lines. Between

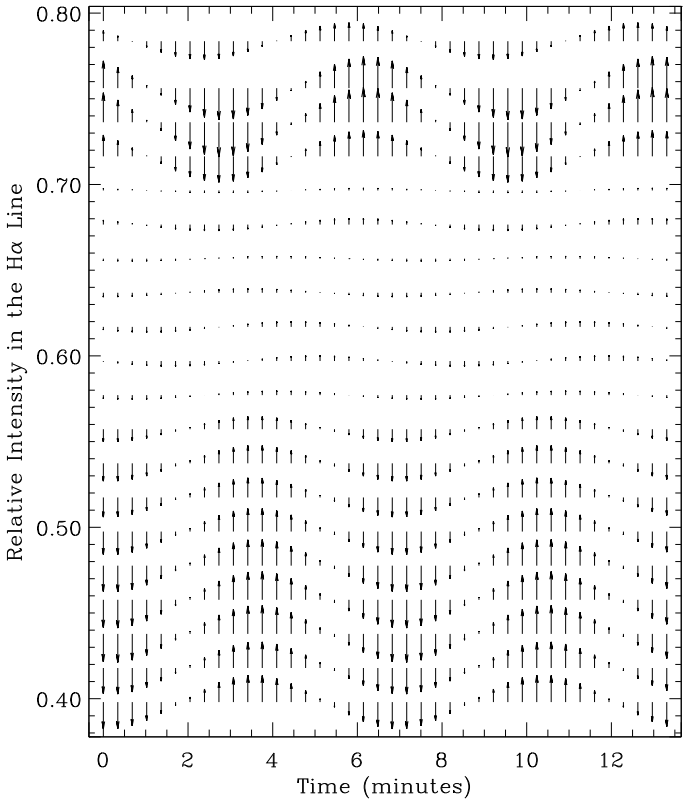

Figure 6.4 Velocity field diagram. The arrows represent bisector velocity vectors, relative to the mean velocity of the star, at different times throughout two pulsation cycles of the principal mode ($P = 6.825$ min). The velocity vectors are calculated from the amplitudes and phases of sections 0–19 given in Table 6.1.

0.7 and 0.8, a blend probably exaggerates the phase reversal by causing an increase in the measured amplitude around height 0.73.

6.3.3 Simulations

Two sources of noise for the velocity measurements, especially at high levels in the Hα line, are errors in the continuum fit and changes in the total equivalent-width (EW) of the line (which are expected due to temperature changes during the pulsation cycle). These sources will affect the bisector velocity if the line is asymmetrical at that height. To investigate, we first simulated fluctuations in the EW of the line and measured the resulting pseudo-velocity amplitude, and then simulated fluctuations in the continuum level. We concluded that, while there could be systematic changes in the velocity amplitude greater than 150 m s^{-1} above a height of 0.65, the phase of the systematic change would be opposite between height 0.72 and 0.76. This means that this effect cannot explain the different phase of heights 0.72–0.79 compared to heights 0.40–0.56. Perhaps, this systematic effect

could explain the large difference in velocity amplitude between height 0.70 and 0.72.

We also considered the effect of a systematic change in the slope of the continuum across the Hα line. This could arise because the continuum fit is not entirely independent of the metal lines and, since there are significantly more metal lines on the blueward side of Hα, the slope of the continuum may vary during the pulsation cycle. We have simulated the effect on the velocity amplitude of a continuum variation having a slope change of 0.001 / 100Å. We found that such a large slope change could produce a systematic change in the velocity amplitude greater than 300 m s^{-1} above a height of 0.75 and thus mimic a velocity phase reversal. However, the simulation fails to reproduce a velocity node at 0.65 and other features of Fig. 6.2. Furthermore, from calculations of the intensity variations in various regions of the spectrum, we do not expect any systematic continuum slope changes to be larger than 0.0001 / 100Å.

Our simulations show that continuum level, continuum slope and Hα EW changes cannot account for the observed features of Fig. 6.2. Therefore, we conclude that the node and phase reversal are caused by the velocity field of the star. Note that random variations in the continuum level and slope may be larger than tested for, but this will only effect the noise level in the amplitude spectra.

6.3.4 Discussion

Hatzes (1996) has simulated line-bisector variations for non-radial pulsations in slowly rotating stars. His simulations show that a bisector velocity phase reversal could occur in modes with $\ell = m \geq 3$ (see Fig. 3 from Hatzes 1996). In fact, the Hα line-bisector variations in α Cir could closely be described by his simulations with $\ell = m = 3$ or 4. However, he does not take into account any changes in pulsational amplitude with depth and the simulations were done for much narrower metal lines. Given that there is strong evidence for the $\ell = 1$ oblique pulsation model (KSMT), we suggest that a change in pulsational amplitude with depth is a more likely explanation for the bisector variations.

It is interesting to note that similar behaviour to that seen in α Cir has been seen in the Sun. Deubner et al. (1996) have observed a phase discontinuity in the solar 3-min oscillations using spectroscopy. In particular, they measured phase differences between the velocity of the core of the NaD_2 line and various positions in the wing (called V$-$V phase spectra). They discovered a 180° phase jump in the V$-$V spectra near a frequency of 7000 μHz. They also observed a phase discontinuity in the V$-$I (Line Intensity) spectra at a similar frequency.

The 3-min oscillations are thought to be formed in an atmospheric (or chromospheric) cavity. Deubner et al. (1996) suggested a model to explain the phase discontinuities, involving running acoustic waves and atmospheric oscillation modes, one of which must have a velocity node in the observed range of heights in the atmosphere.

In the solar model, the eigenfunction of a p-mode with $\ell = 1$ and $n = 25$ has a radial node separation in the outer part of the Sun of $\sim$0.3 percent of the radius (Christensen-Dalsgaard 1998). In α Cir, if we assume the oblique dipole pulsation model ($\ell = 1$) for the principal mode, with a large frequency separation $\Delta\nu_0 = 50\,\mu$Hz (KSMT), then the overtone value of the principal mode is $n = 48$, using the asymptotic theory of astero-

seismology (e.g. Brown & Gilliland 1994). The radial node separation in α Cir is then expected to be $\sim$0.15 percent of the radius of the star. This is equivalent to a distance of about 1900 km, assuming the radius of α Cir is about twice the radius of the Sun (see Section 6.1.1). This does not take in to account the difference in density as a function of radius between α Cir and the Sun. Using model atmospheres (Friedrich Kupka, private communication) to estimate the sound speed (v) just above the photosphere, we obtain a radial node separation of about 1500 km ($v/2f$; see Appendix A.2 for details). This is in good agreement with the estimate obtained by scaling from a solar model.

In the model of α Cir used by Medupe & Kurtz (1998), the geometric height between the formation of the I band and the B band is 250 km. We speculate that the extent of the line forming region is about 1000 km and that we are seeing one velocity node in the atmosphere. Recently Gautschy et al. (1998) described pulsation models for roAp stars which suggest that radial nodes can be expected in the atmospheres of these stars.

6.4 Equivalent-width measurements of Hα

Kjeldsen et al. (1995) developed a new technique for detecting stellar oscillations through their effect on the equivalent-width (EW) of Balmer lines. We expect to find changes in the Hα EW in α Cir due to temperature changes in the star.

6.4.1 Reductions

We measured the EW changes of the Hα line directly by looking at intensity changes in regions of varying width across Hα. First of all, the spectra were linearly re-binned by a factor of 40 and shifted so that the centre of the Hα line was in the same wavelength position for each spectrum. This was to reduce the noise caused by instrumental shifts of the spectra. The value used to define the centre of the Hα line in each spectrum was taken from the cross-correlation measurements used for Chapter 5. Next, the mean intensities in 11 trapezium-shaped filters (Cols. 1–2 of Table 6.2) were measured in each spectrum. Each filter was centred on Hα and the sloping part of the trapezium was two pixels wide (~ 1Å) at each end (see Fig. 6.3 for an example).

For each filter, we obtained a time series of intensity measurements which was analysed in the same way as in Section 6.2.3 to yield the amplitudes shown in Cols. 4–5 of Table 6.2. From an intensity change (δI), we defined the fractional EW change as:

$$\frac{\delta W}{W} = \frac{-\delta I}{C - I} \tag{6.1}$$

where W is the equivalent-width, C is the continuum level (approx. 1.00 in our reduced spectra) and I is the mean intensity in the filter averaged over all the spectra (Col. 3 of Table 6.2). Using this formula, we converted intensity amplitude spectra to EW amplitude spectra. To test whether any bisector variations could affect these measurements, we simulated shifts of $\pm 600\,\mathrm{m\,s^{-1}}$ in the template spectrum. From this, we determined that the effect of such a signal on the filter intensities would be less than the rms-noise level.

Table 6.2 Equivalent-width (EW) amplitudes and phases of the principal mode for filters of different width across Hα. The measured relative intensity amplitudes (δI) are converted to fractional EW amplitudes ($\delta W/W$), using the formula given in Section 6.4.1. For the results in this table, the Stromlo and the La Silla data sets were combined.

filter no.	filter width[a] (Å)	mean intensity[b]	intensity ampl.[c] (ppm)	intensity noise[d] (ppm)	EW ampl.[c] (ppm)	EW noise[d] (ppm)	S/N	EW phase[e] (°)	phase error[f] (°)
0	1.0	0.378	1085	72	1743	116	15.1	354	4
1	2.0	0.402	996	42	1667	69	24.0	354	2
2	5.9	0.511	692	20	1415	40	35.4	357	2
3	13.7	0.616	441	20	1148	51	22.6	1	3
4	17.6	0.650	390	20	1114	56	19.7	3	3
5	24.5	0.694	301	20	982	65	15.0	1	4
6	31.9	0.730	246	20	913	76	12.1	7	5
7	45.1	0.779	201	21	909	95	9.6	9	6
8	66.6	0.829	156	21	911	122	7.5	13	8
9	81.8	0.853	147	21	995	141	7.1	12	8
10	110.7	0.882	122	20	1039	172	6.0	11	10

[a] Full-width half-maximum of filter centred on Hα.
[b] Mean relative intensity in the filter averaged over all the spectra. The continuum level is ∼1.00.
[c,d,e,f] See Table 6.1.

6.4.2 Results

The results for the principal mode are shown in Cols. 6–10 of Table 6.2 and in Fig. 6.5. The phases of all the measurements lie between $-10°$ and $15°$. Since our phase reference point (t_0) coincides with maximum light (see Chapter 5), we conclude that the EW of the Hα line is pulsating in phase with the luminosity. This is expected, since maximum EW of the Hα line indicates maximum temperature in the stellar atmosphere. If the EW amplitude were the same in all filters then the change in intensity at each wavelength would be to be proportional to the depth of the absorption at that wavelength, i.e., $\delta I \propto C - I$. Such a profile variation is shown greatly exaggerated in Fig. 6.6. Our results in Fig. 6.5 suggest that this is nearly the case, with an amplitude of 1000 ppm, except that the core of the line is fluctuating in intensity by more than expected (see Appendix A.3 for a related analysis concerning variations in the width of the Hα line).

We must remember that the measurements were made on continuum-fitted spectra, which means that the absolute flux[1] in the core might be constant while the wings and continuum are changing in flux. We do have information about the pulsation in continuum

[1] We use the term `intensity` when referring to continuum-fitted spectra and the term `flux` when considering the true flux from the star.

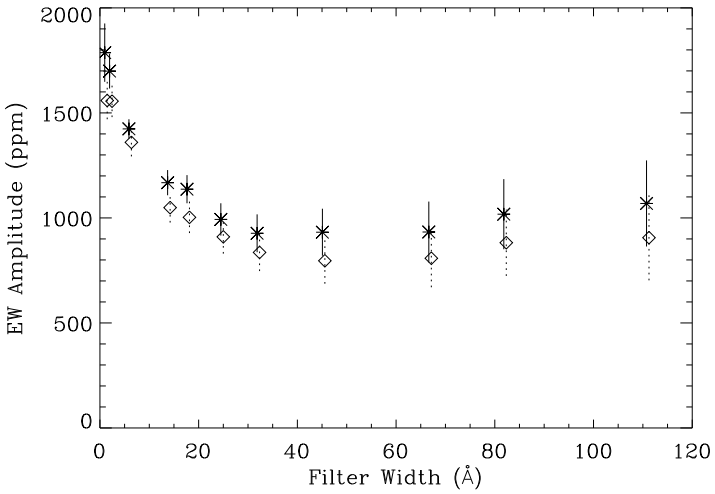

Figure 6.5 The EW amplitude in filters of different width centred on the Hα line. The stars with solid lines represent the Stromlo data and diamonds with dotted lines represent the La Silla data.

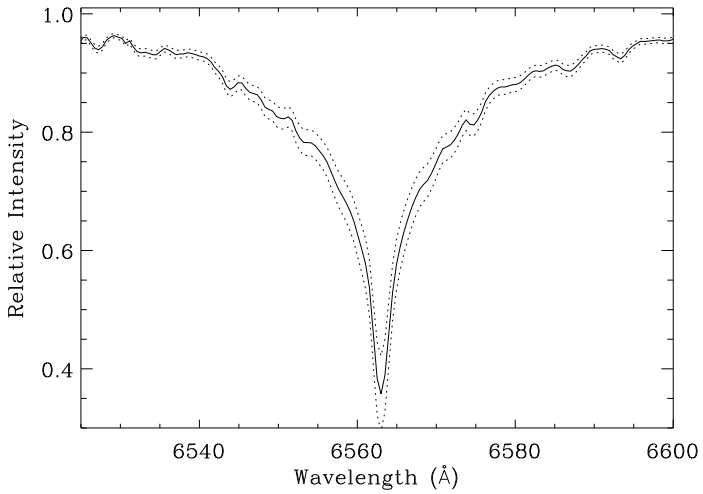

Figure 6.6 The Hα line with the dotted lines showing the profile with an increase and a decrease of 10 percent in EW. A variation of this type, but with much smaller amplitude (1000 ppm), was used to generate the dashed line in Fig. 6.8; and would produce a constant amplitude in Fig. 6.5.

flux. Medupe & Kurtz (1998) measured the photometric amplitude in Johnson R (central wavelength 6380Å) to be 0.54 ± 0.15 mmag (500 ± 140 ppm). A continuum flux amplitude of 500 ppm could only account for a 200 ppm Hα core relative intensity amplitude in continuum fitted spectra. This value is significantly smaller than the measured value of $\sim$1000 ppm (filter 1). Therefore, we can say with some certainty that the continuum flux from the star is varying in anti-phase with the flux in the core of the line and that, at some point in the wings of Hα, the flux is constant. To investigate this, we have calculated the intensity amplitude of the principal oscillation mode at each pixel in the spectrum, as we describe in Section 6.5.1.

6.4.3 The equivalent-width amplitude

Using the photometric amplitude for α Cir of $\sim$1.7 mmag (Johnson B) measured by Don Kurtz (private communication) around the time of our observations, we can calculate the expected EW amplitude of the principal pulsation mode. The photometric amplitude converts to $(\delta L/L)_{\rm bol} = 1.5 \times 10^{-3}$ using the relation of Kjeldsen & Bedding (1995) with $T_{\rm eff} = 7900$ K. In order to convert this to an EW amplitude, we use the scaling law from Bedding et al. (1996) which can be written as;

$$\frac{\delta W}{W} = \frac{1}{4} \frac{\delta \ln W}{\delta \ln T_{\rm eff}} \left(\frac{\delta L}{L} \right)_{\rm bol} . \tag{6.2}$$

Model atmospheres can be used to estimate the change in EW of the Balmer lines as a function of temperature. From Kurucz's models of the Hα profile with $\log g = 4.0$ (see Table 8A from Kurucz 1979), $\delta \ln W / \delta \ln T \approx 2.8$ between 7500 K and 8000 K. Using this value, we predict an EW amplitude of $\delta W/W = 1.0 \times 10^{-3}$.

The measured amplitude of 1000 ± 140 ppm (filter 9, see Table 6.2) is in excellent agreement with the prediction. However, to some extent the agreement is fortuitous because in reality, neither $(\delta L/L)_{\rm bol}$ nor $\delta \ln W / \delta \ln T$ are particularly well known. In the first case, since the photometric amplitude of α Cir varies with wavelength by more than expected for a blackbody (Medupe & Kurtz 1998), this will affect the bolometric luminosity amplitude. In the second case, the value depends significantly on the effective temperature and the accuracy of the model, giving a possible range in $\delta \ln W / \delta \ln T$ of 2–4. Additionally, there are uncertainties in the sensitivity of the EW amplitude to different modes (Bedding et al. 1996). Finally, note that the velocity amplitude is predicted to be 120 m s^{-1} using the same scaling laws (Kjeldsen & Bedding 1995), while the measured amplitudes vary between 0 and 1000 m s^{-1} (Chapter 5).

6.5 Pixel-by-pixel intensity measurements

Another way of examining changes in the Hα profile is to look at relative intensity changes across the Hα region as a function of wavelength (pixel by pixel).

6.5.1 Reductions

We could apply the time series analysis, as described in Section 6.2.3, to the intensity of each pixel in our spectrum. However, this is computationally intensive and, since we are only interested in the amplitude of the principal mode, is unnecessary. Instead, the spectra were phase-binned at the principal frequency. The phase-binning was done so that Fast Fourier Transforms (FFTs) could be applied to the intensity variations, and therefore save calculation time for the measurement of the amplitude of the principal mode.

A sample of 4718 spectra from the Stromlo data set was used to produce the phase-binned spectra. Spectra which produced bad data points from the EW measurements (Section 6.4.1) were not included. Each spectrum was linearly re-binned by a factor of 10 and shifted so that the centre of the Hα line was in the same wavelength position for each spectrum (determined by cross-correlation). This was similar to the reduction in Section 6.4.1. Additionally, the intensities in each spectrum were slightly adjusted, in order to remove low-frequency variations of the mean intensity across the Hα region (filter 9, 6522Å–6604Å). This was necessary in order to avoid introducing noise at the principal frequency due to the low-frequency intensity variations. Using this adjustment, we obtained consistent results between the filter measurements on the individual spectra and on the phase-binned spectra. The spectra were phase-binned at the principal frequency using a weighted mean in each phase-bin (25 phase-bins were used but this number was not critical). Finally, a FFT was applied to the phase-binned series of intensities, to measure the amplitude and phase of the principal mode and its harmonics for each pixel.

6.5.2 Results

The intensity amplitudes of the principal mode and harmonics, as a function of wavelength, are shown in Fig. 6.7. Note that a signal is expected in the first harmonic with an amplitude of about 8 percent of the principal mode (KSMT), with higher harmonics containing negligible signal. Therefore, the harmonics give a good indication of the noise level (the rms-noise is ~ 60 ppm). From Fig. 6.7, it is clear that the simple description of the profile variation given in Section 6.4.2 is inadequate and that the metal lines have an impact on the intensity variations. For instance, the peak blueward of Hα could be caused by the Sr I 6550.2Å line, while the Fe I 6569.2Å line may also have an effect (this is more evident in the next figure). The signal from the core of Hα is strong while the signal from the wings is much weaker.

To show the phase information, we have chosen to plot the cosine and sine components of the principal mode separately (see Fig. 6.8). The phase of most pixels is near 0° or 180° and therefore most of the information is contained within the cosine component, which represents the relative intensity variations that are in phase or in anti-phase with

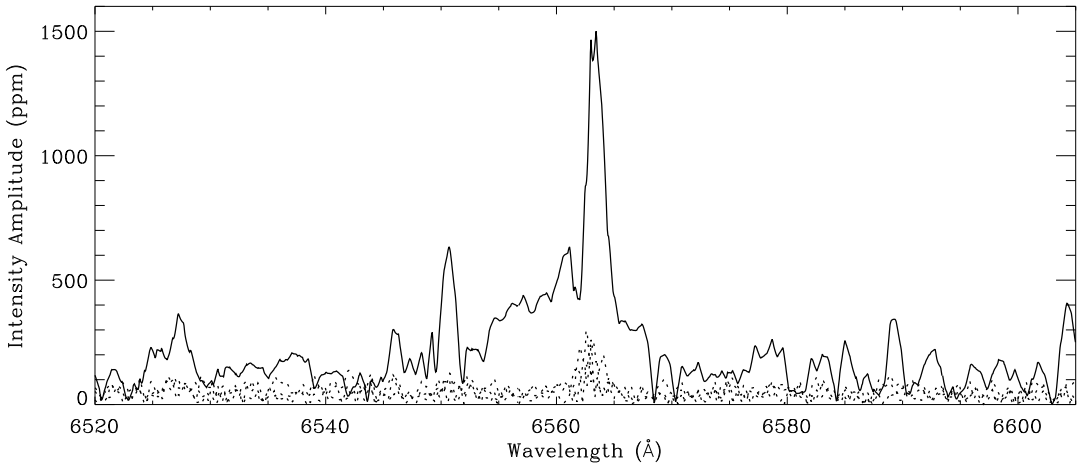

Figure 6.7 Relative intensity amplitude as a function of wavelength. The solid line represents the principal mode, while the other lines show three higher frequencies (harmonics).

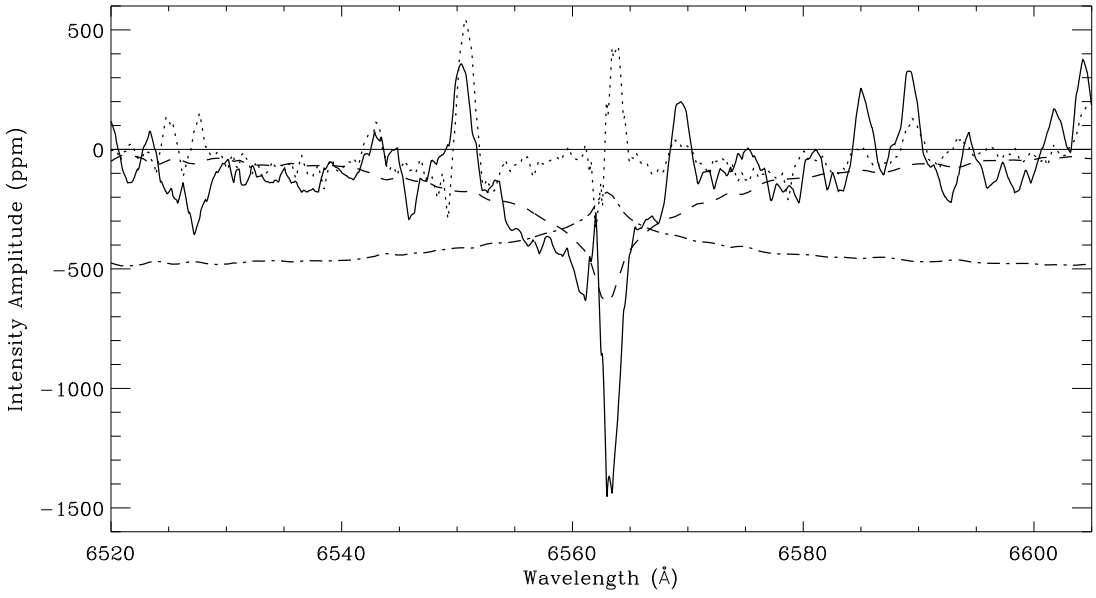

Figure 6.8 Relative intensity component amplitudes of the principal mode. The solid line represents the cosine amplitude which represents intensity changes in phase or in anti-phase with the photometric pulsation. The dotted line represents the sine amplitude. The dashed line is a theoretical amplitude with $\delta I = -10^{-3}(C - I)$, and the dash-and-dotted line shows $\delta I = -5 \times 10^{-4} I/C$ which represents approximately where the absolute flux amplitude would be zero (see text for details).

the photometric pulsation. The amplitudes of this component are mostly negative which means that at maximum light, the relative intensity is at a minimum i.e. the EW of Hα is at a maximum.

Two different simulations are also plotted:

(i) The dashed line represents the relative intensity amplitude assuming $\delta I = -A(C - I)$, where A is the EW amplitude of 1000 ppm. This is the amplitude (cosine component) expected from the profile variation described in Section 6.4.2.

(ii) The dash-and-dotted line represents $\delta I = -AI/C$ where A is the continuum flux amplitude of 500 ppm (Medupe & Kurtz 1998). This line shows how the relative intensity amplitude (cosine component) would behave if the absolute flux in this region were constant (6520Å – 6605Å), and the continuum flux outside this region were pulsating at the measured value of 500 ppm. This is not a realistic simulation but we use it to estimate how the absolute flux in this region behaves. Where the solid line is above the dash-and-dotted line, the absolute flux is pulsating in phase with the continuum. We see that the absolute flux of the inner 10Å of the Hα line is pulsating in anti-phase with the continuum.

6.5.3 Discussion

To evaluate these results, we have to consider systematic errors. Unlike for the bisector velocities, any systematic errors in the continuum level directly affect the EW and relative intensity measurements. The direction of any error would be the same at all wavelengths, equivalent to an offset in the cosine amplitude shown in Fig. 6.8. From looking at pseudo-continuum regions outside Hα, we estimate the intensity amplitude of the continuum level to be 100 ppm in the continuum fitted spectra (cosine component of -100 ppm). This slightly changes the details of the Hα profile variation.

Other systematic errors may be caused by residual Doppler shift signals that were not removed by the reduction process. It was not possible to remove such signals completely because of the variation in velocity amplitude and phase between different lines and between different heights in the Hα line. This could account for some of the sine component of the amplitude.

Ronan et al. (1991) measured the oscillatory signal in the Sun as a function of optical wavelength. One of their wavelength regions included the Balmer lines Hγ and Hδ. More recently, Keller et al. (1998) looked at the Hβ line region in the Sun, using a similar technique. Both groups showed that the absolute flux oscillations in the Balmer lines were reduced to about 70 percent of the continuum signal. This differs sharply from α Cir, where the Hα core absolute flux is pulsating in anti-phase with the continuum. This may be due to a pulsational temperature node in the atmosphere of α Cir, as was indicated by the results of Medupe & Kurtz (1998), and by the velocity node. The relationship between the temperature node and the velocity node is unclear with the present data.

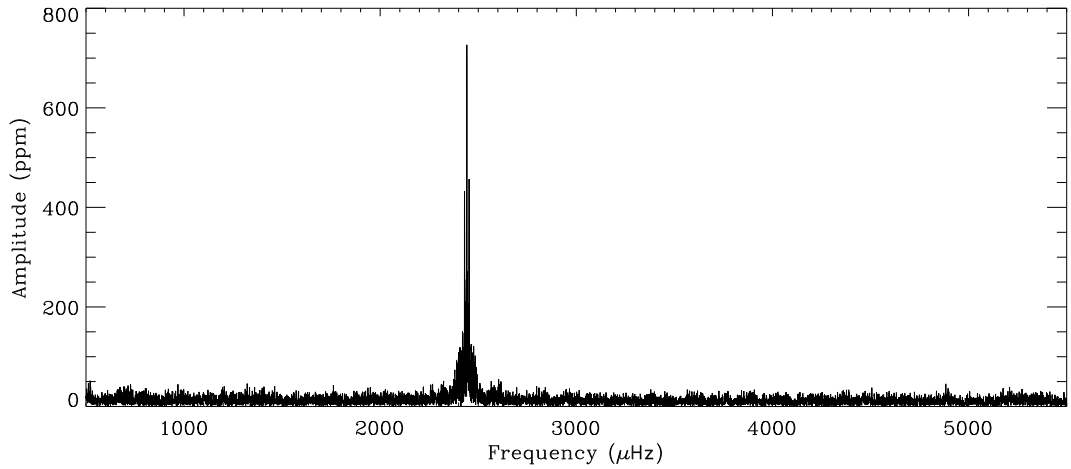

Figure 6.9 Amplitude (δR_{cw}) spectrum of the intensity ratio measurements

6.6 Detection of other frequencies

In order to detect weaker modes in α Cir, we need an observable which has a high signal-to-noise ratio in the amplitude spectrum. Of the observables discussed so far, the one with the highest S/N for the principal mode is filter 2 from the EW measurements (S/N $= 35$, see Col. 8 of Table 6.2). However, for the measurements of intensity in different filters across Hα, the noise level is approximately the same for filters 2–10 (20 ppm, see Col. 5 of Table 6.2). This means that the noise is caused by variations in the continuum level and not by photon noise. Therefore, we can improve the S/N for the principal mode by dividing the intensity in one filter by another and thereby reducing errors caused by the continuum fit. The highest S/N ($= 51$) was obtained by dividing the intensity in filter 2 (FWHM $\sim$ 6Å) by filter 7 (FWHM $\sim$ 45Å). We call this observable R_{cw} (ratio of Hα core to wing intensity). This is analogous to narrow / wide Hβ photometry.

We produced a time series of these R_{cw} measurements which was analysed in the same way as in Section 6.2.3. The amplitude (δR_{cw}) of the principal mode was measured to be 727 ppm, with an rms-noise level in the amplitude spectrum of 14 ppm (see Fig. 6.9). To search for other frequencies which were detected by KSMT (the same numbering is used), the principal pulsation mode was then subtracted from the time series to produce a pre-whitened amplitude spectrum (see Figs. 6.10–6.11). In this spectrum, we have detected the modes f_4, f_5 and $2f_1$, and the rotational splitting of the principal mode ($f_1 \pm r$), with amplitudes greater than $2.3\times$rms-noise. We have not measured the frequencies but have used the values given by KSMT, except we have increased the frequencies of f_1 to f_5 by 0.03 μHz for consistency with the change in the principal frequency, as measured during our observations (see Chapter 5). The rotational splitting r is taken as 2.59 μHz, as measured by KSMT.

The amplitudes and phases of each mode are shown in Table 6.3, with the last two columns showing the amplitude relative to that of the principal mode, both for our spec-

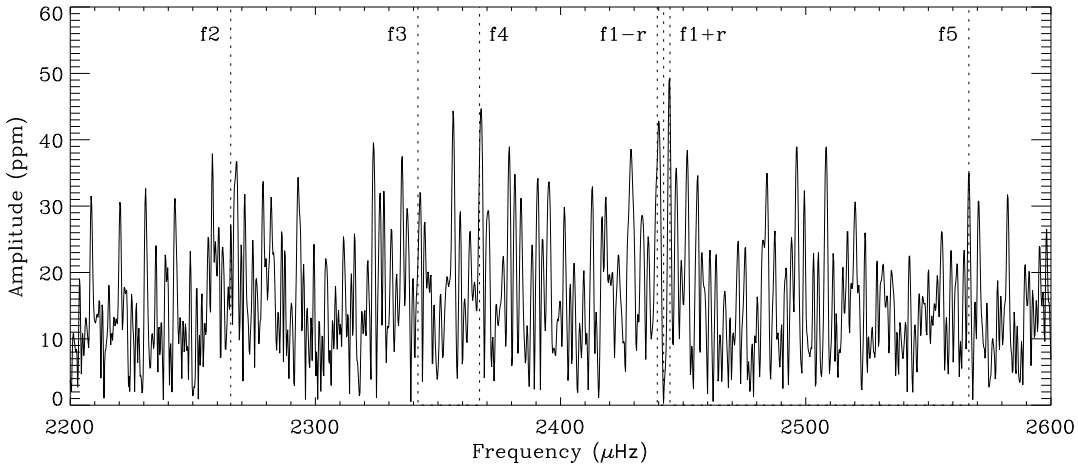

Figure 6.10 Amplitude spectrum after subtracting the principal frequency. The dotted lines represent the frequencies of modes detected by KSMT.

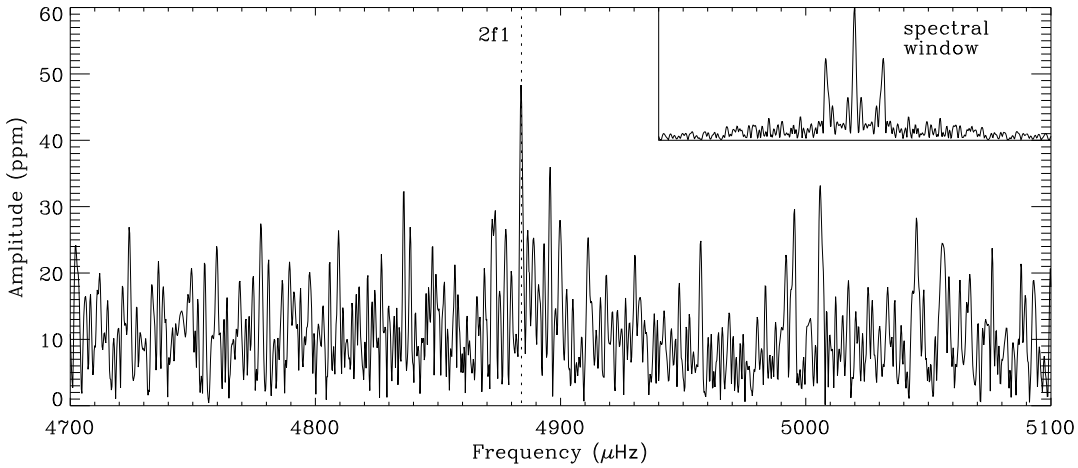

Figure 6.11 Amplitude spectrum after subtracting the principal frequency, at a higher frequency than Fig. 6.10. The dotted line represents the frequency of the first harmonic of the principal mode. The inset shows the spectral window on the same frequency scale.

Table 6.3 The amplitudes (δR_{cw}) and phases of different modes measured using the intensity ratio of filter 2 and filter 7 (see Table 6.2). Except for the principal mode (f_1), the measurements are made after pre-whitening with the principal frequency.

mode	freq.[a] (μHz)	ampl. (ppm)	S/N[b]	phase[c] (°)	phase error[d]	relative amplitude δR_{cw}[e]	relative amplitude photometric[f]
f_2	2265.46	26	1.8	—	—	0.036	0.055
f_3	2341.82	20	1.4	—	—	0.028	0.063
f_4	2366.97	35	2.4	272	24	0.048	0.057
$f_1 - r$	2439.44	37	2.6	92	23	0.050	0.095
f_1	2442.03	727	50.8	174	1	1.000	1.000
$f_1 + r$	2444.62	48	3.4	306	17	0.066	0.115
f_5	2566.52	34	2.4	16	25	0.047	0.046
$2f_1$	4884.06	48	3.4	76	17	0.066	0.077

[a] Frequencies taken from KSMT. See text for details.
[b] rms-noise estimated to be 14 ppm from the pre-whitened amplitude spectrum in the region 1100–4400 μHz.
[c] Phase measured with respect to a reference-point (t_0) at JD 2450215.07527, with the convention that a phase of 0° represents maximum of the observed variable.
[d] Error in the phase is taken to be arcsin (rms-noise/amplitude).
[e] Error of approximately 0.020 (rms-noise/amplitude of principal mode).
[f] Strömgren v photometry (KSMT), with an error of approximately 0.007.

tral data and for KSMT's photometric data. A possible significant difference is for the rotational side-lobes. Both side-lobes have a lower relative amplitude by more than 0.04 in our data. This rotational splitting is caused by a variation in the amplitude of the principal mode during the rotation cycle ($P_{\rm rot} = 4.479$ days). Our results therefore suggest that the amplitude δR_{cw} of the principal mode varies by less during the rotational cycle than the photometric amplitude.

To examine this, we divided the time series into 32 shorter time periods of about 4 hours each. In Fig. 6.12, we show the amplitude δR_{cw} of the principal mode for each time period. The solid line shows the amplitude variation expected from the measurements of f_1, $f_1 - r$ and $f_1 + r$ in the amplitude spectrum of the complete time series (Table 6.3). The dotted line shows the expected amplitude variation based on the full range variation of 21 percent and the ephemeris from the photometric results (KSMT). There is good agreement between the amplitude maximum of our fit and the ephemeris of KSMT, which supports the accuracy of the rotation period derived by them. Both fits shown in Fig. 6.12 appear to be consistent with the results of the analysis using the shorter time periods. Therefore, we cannot say with certainty that the percentage amplitude variation is less in our data than the variation measured by KSMT. Such a difference, if it exists, may be due to limb-darkening.

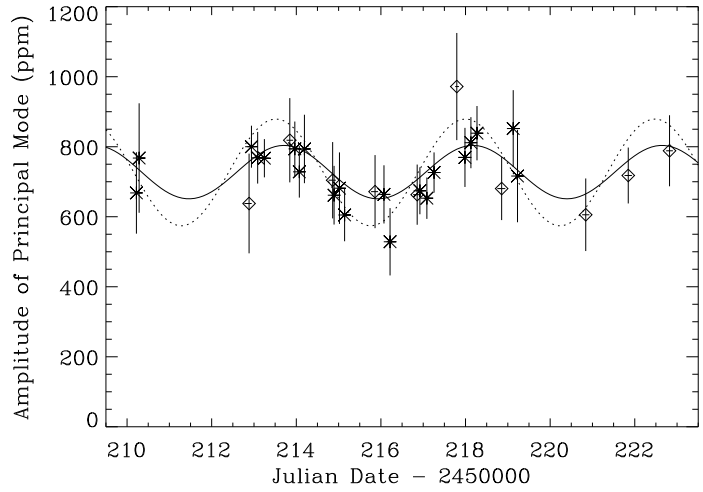

Figure 6.12 Amplitude (δR_{cw}) of the principal pulsation mode during separate time periods (each about 4 hours long). The asterisks represent the Stromlo data and the diamonds represent the La Silla data. The error bar for each amplitude measurement is the rms-noise level. See text for an explanation of the solid and dotted lines.

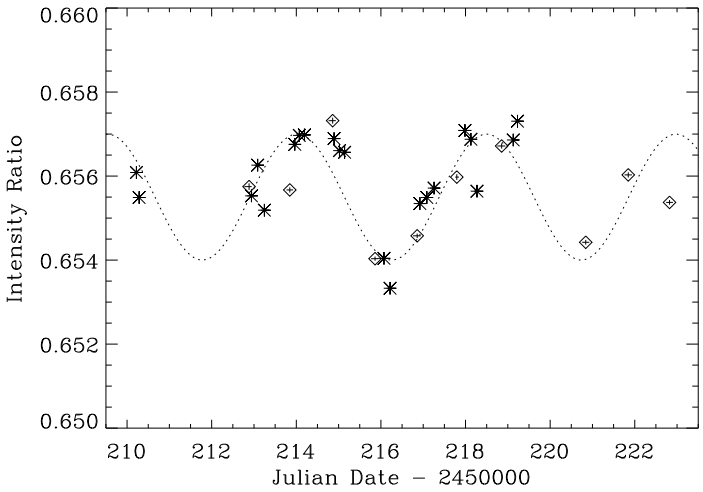

Figure 6.13 Average intensity ratio (R_{cw}) during separate time periods (each about 4 hours long). The asterisks represent the Stromlo data. The diamonds represent the La Silla data, which have been increased by 0.4 percent to match the Stromlo data. The dotted line shows a sine-wave with a period equal to the rotation period of the star.

The average value of R_{cw} itself in each time period varied slightly during the observation period and was slightly different between the Stromlo and La Silla data sets (see Fig. 6.13). The difference in the value between the two data sets was about 0.4 percent and was due to the inexact matching of the filters. The variation with time seen in Fig. 6.13 is probably caused by the rotation of the star, which is slightly inhomogeneous in surface brightness. This variation does not significantly affect the measurement of δR_{cw} at pulsation frequencies.

Variation of Balmer line profiles with rotation is common in Ap stars. For example, Musielok & Madej (1988) investigated 22 Ap stars of which 17 showed variation of the Hβ index with a typical amplitude of 0.02 mag (19000 ppm). Our observed δR_{cw} amplitude of about 1500 ppm at the rotation frequency in α Cir corresponds to a much smaller Balmer line variation than is typical of Ap stars, even if we allow for some difference between the Hβ index and R_{cw}. To test this, we calculated an intensity ratio using filters across Hα of similar widths to those used for the Hβ index (FWHMs $\sim$ 40Å and $\sim$ 150Å). The rotational amplitude of this intensity ratio was 1000–1500 ppm, which is more than a factor of ten smaller than the 0.02 mag found by Musielok & Madej in other Ap stars.

6.7 Conclusions

The existence of a radial standing wave node of the principal pulsation mode can explain the velocity phase reversal in the Hα line. However, there is only a 140° velocity phase shift between the Hα core and higher in the line. If we were seeing a pure standing wave in the atmosphere then we would expect a 180° phase shift. A travelling wave component, blending or the systematic effects described in Section 6.3.3 may cause the discrepancy. Additionally, many of the metal lines studied in Chapter 5 show phases that are neither in phase or in anti-phase with the majority of the lines. We proposed that some of the phases were anomalous and did not represent velocity phases due to blending effects. Therefore, in a time series of less blended (higher resolution) spectra, there should be a clearer distinction between those lines that are formed above and below the velocity node and fewer lines with anomalous phases.

Analysis of the Hα profile during the principal pulsation cycle, shows a large change in relative intensity of the core of the line. This means that the absolute flux of the core is pulsating in anti-phase with the continuum, possibly indicating a pulsational temperature node in the atmosphere, as suggested by Medupe & Kurtz (1998) on the basis of multi-colour photometry. However, Medupe et al. (1998) show that non-adiabatic effects can explain the photometric results without the need for a node. Perhaps, non-adiabatic effects have a significant effect on the Hα profile changes in α Cir.

The next stage in the analysis of the mode dynamics in the atmosphere could be the use of high resolution (R$\sim$50000) spectroscopy to study the velocities, bisectors and EW changes of unblended metal lines, combined with model atmospheres to calculate the formation height of the lines. This may allow us to decide whether there is travelling wave component, to relate the velocity changes to the temperature changes, to measure

any surface or vertical inhomogeneities in the distribution of certain elements, and to test non-adiabatic non-radial pulsation equations.

By defining an observable which detects the relative intensity changes in the core of the Hα line, R_{cw}, we detected some of the weaker modes in α Cir. This is probably the first detection, in roAp stars, of modes with photometric (B) amplitudes of less than 0.2 mmag, using a spectroscopic technique. The ratio between spectroscopic amplitudes and photometric amplitudes can be used to identify the ℓ value of different oscillations modes, as has been done recently by Viskum et al. (1998b, 1998c) for the δ Scuti star FG Vir. We do not have enough S/N to identify the modes in α Cir, but we show the potential for using this mode identification technique.

α Cir offers one of the best chances for theoreticians to model a star where magnetic fields are important both for its evolution and pulsation, because of the detailed information that can be gained from its oscillation modes using spectroscopy and photometry. Additionally, there is already a well determined luminosity using Hipparcos and, when angular diameter measurements are made, there will also be direct measurements of the effective temperature and radius of the star.

Chapter 7

The pulsation of the roAp star HR 3831

Some of the results presented in this chapter were published in paper Baldry et al. (1998c) in collaboration with Don Kurtz and Tim Bedding. I observed and reduced the spectroscopic data with the supervision of T. Bedding. D. Kurtz provided the analysis of the photometric data taken at the same time as the spectroscopic data. This chapter is a rewritten and extended version of the paper.

7.1 Introduction

The roAp stars pulsate in high-overtone non-radial p-modes. The oscillation spectra of many of these stars reveal frequency multiplets – usually triplets – with equal frequency separations of the components. The separations are equal to, or very nearly equal to, the rotation frequency (determined from the variation of spectrum and light as the star rotates).

One explanation of the observed triplets is that a set of rotationally perturbed m-modes is excited, e.g. $\ell = 1$ dipole modes with $m = -1$, 0, +1. The observed frequencies can be written as (Ledoux 1951)

$$\nu_m = \nu_0 - m(1 - C_{n\ell})\nu_{rot} \tag{7.1}$$

where $C_{n\ell}$ is a constant that depends on the structure of the star. For A-star models with the expected pulsation modes for roAp stars, Takata & Shibahashi (1995) found $C_{n\ell} \approx 0.003$–0.010. However, in the best-observed roAp star HR 3831, Kurtz et al. (1992) were able to show that $C_{n\ell} < 2 \times 10^{-5}$. This is two orders of magnitude less than the theoretically predicted values, and suggests that the frequency splitting is precisely the rotational frequency.

Another explanation for a frequency multiplet is that it is produced by a single pulsation mode (e.g., $\ell = 1$, $m = 0$) whose amplitude is modulated[1] by rotation. This naturally produces a frequency splitting that is precisely equal to the rotation frequency. In some roAp stars, the amplitude of the pulsation has been observed to modulate with rotation

[1] In this chapter, we use the verb *to modulate* and its derivatives to describe changes in amplitudes and phases with rotation, and the verb *to vary* for other types of changes.

in phase with the magnetic variation. To explain this phenomena, the oblique pulsator model was proposed by Kurtz (1982), and has been extensively developed by Shibahashi & Takata (1993; Takata & Shibahashi 1994, 1995). In this model, the magnetic and pulsation axes are aligned but are oblique to the rotation axis. The observed amplitude modulation is then due to the variation in the angle between the pulsation axis and the line of sight as the star rotates.

In an alternative model, the spotted pulsator model (Mathys 1985), the pulsation and rotation axes are aligned (or there are radial $\ell = 0$ modes), but the ratio of flux to radius variations varies over the surface because of differences in the flux and temperature caused by spots associated with the magnetic field. The observed radial velocity (RV) amplitude is then constant, but the photometric amplitude modulates as the star rotates. Therefore, the two models can be distinguished by RV observations. Matthews et al. (1988) found RV amplitude variation in HR 1217 which favoured the oblique pulsator model, but this star is multi-periodic, so the observed variation could have been caused by beating among pulsation frequencies. Kurtz et al. (1994a) proposed that the two models could easily be distinguished by RV measurements of HR 3831. This roAp star has one dominant pulsation mode with a period of 11.7 min, has a large photometric amplitude modulation including a phase reversal (Kurtz et al. 1994a, 1997) and is bright enough for accurate RV measurements ($V = 6.25$).

In this chapter, we look at RV changes and Hα profile changes in HR 3831. We find that the radial velocities are modulated with the rotation of the star. A frequency analysis of the Hα RV shows a frequency triplet with the same spacing and amplitude ratios as in contemporaneous photometric observations which we obtained at the South African Astronomical Observatory. This is expected in the oblique pulsator model, and in clear disagreement with the prediction of the spotted pulsator model.

We also studied this star using some of the other techniques that were used in Chapters 5–6. These include cross-correlations of different wavelength regions, line-shifts of the Hα bisector and intensity measurements across the Hα line. While the oblique pulsator explains most of the observed rotational modulations, aspects of the spotted pulsator model and perturbed m-modes may also have an influence on the pulsations in this star.

7.1.1 Basic data for HR 3831

HR 3831 (IM Vel, HD 83368, HIP 47145) has a binary companion with $V = 9.09$ with a separation of 3.29 arcsec. The brightness of HR 3831 is often quoted as $V = 6.17$ which is from the combined flux measurement (see Kurtz et al. 1994a). The parallax has been measured by the *Hipparcos* mission (ESA 1997) to give a distance of 72.5 ± 4 pc to the star. Using $V = 6.25$, this distance, an effective temperature of 8000 ± 200 K (Kurtz et al. 1994a) and a bolometric correction of -0.13 (Schmidt-Kaler 1982), we obtain $L = 13.4 \pm 1.5 L_\odot$ and $R = 1.9 \pm 0.2 R_\odot$.

The oscillation spectrum of HR 3831 has a well-known frequency septuplet around 1428 μHz, plus frequency multiplets at the harmonics (Kurtz et al. 1997). However, there are just four frequencies which have photometric (Johnson B) amplitudes above 0.3 mmag and that are detectable in our data. These include a triplet around the princi-

pal mode ($\nu_{-1} = 1423.95\,\mu$Hz, $\nu_0 = 1428.01\,\mu$Hz, $\nu_{+1} = 1432.07\,\mu$Hz) and the first harmonic ($2\nu_0 = 2856.02\,\mu$Hz). The splitting of the triplet is the rotation frequency ($\nu_{\rm rot} = 4.06\,\mu$Hz) giving $P_{\rm rot} = 2.851976$ d, under the assumption that the oblique pulsator model is correct. Unlike the triplet in α Cir, where the amplitudes of the two sidelobes are about 10 percent of the principal amplitude, the amplitudes of ν_{-1} and ν_{+1} are larger than the amplitude of the central frequency. This means, that during the rotation cycle of HR 3831, the amplitude measured at ν_0 goes through two maxima with two phase reversals. In terms of the oblique pulsator model, the star pulsates in an $\ell = 1$ dipole mode which is sufficiently oblique to the rotation axis that as the star rotates we see first one pole and then the other.

Kurtz et al. (1990; Kurtz 1990) describe a generalised oblique pulsator model in which the effects of both the magnetic field and rotation were taken into account (see also Dziembowski & Goode 1985, 1986). In this model, the perturbation to the star's eigenfrequencies by the magnetic field dominates, leading to the conclusion that the pulsation axis is locked to the magnetic axis. Two parameters related to the amplitude ratios in the frequency triplet were defined:

$$P_1 = \frac{A_{+1} + A_{-1}}{A_0} = \tan i \tan \beta \,, \tag{7.2}$$

where i is the inclination of the rotation axis to the line of sight, and β is the angle between the rotation axis and the pulsation axis; and

$$P_2 = \frac{A_{+1} - A_{-1}}{A_{+1} + A_{-1}} = \frac{C_{n\ell}\,\nu_{rot}}{\nu_1^{(1)mag} - \nu_0^{(1)mag}} \,, \tag{7.3}$$

where the perturbation to the eigenfrequencies (by the magnetic field) depends on $|m|$ such that $\nu = \nu^{(0)} + \nu_{|m|}^{(1)mag}$. From the photometric results for HR 3831 covering 1993 to 1996 (Kurtz et al. 1997), $P_1 = 8.6 \pm 0.2$ and $P_2 = -0.097 \pm 0.004$.

7.2 Observations

7.2.1 Spectroscopy

We have obtained intermediate-resolution spectra of HR 3831 using the coudé spectrograph (dispersion of 0.49 Å/pixel) on the 74-inch Telescope at Mt. Stromlo, Australia. We have a total of 1400 spectra from a one week period in 1997 March (Table 7.1), with each spectrum having a minimum of 60 000 photons/Å. The average number of photons/Å in each spectrum was 270 000. The exposure time was 100 seconds, with an over-head between exposures of 20 seconds.

All of the CCD images were reduced to spectra using the same procedures that were used on the Stromlo data in Chapter 5. Several observables were defined from the spectrum (velocities, intensities, bisector measurements), to produce a time series of measurements for each observable. For use in various measurements, a template spectrum was defined from 25 high-quality spectra (Figures B.1–B.2).

Table 7.1 Log of the spectroscopic observations of HR 3831

UT-date	No. of hours	No. of spectra	Julian dates −2 450 000
1997 Mar 10	1.37	26	517.88 – 517.94
1997 Mar 10	3.61	38	518.12 – 518.27
1997 Mar 11	10.03	203	518.88 – 519.29
1997 Mar 12	9.59	285	519.88 – 520.28
1997 Mar 13	2.22	59	520.88 – 520.97
1997 Mar 13	1.10	33	521.27 – 521.32
1997 Mar 14	10.57	319	521.87 – 522.31
1997 Mar 15	10.40	262	522.88 – 523.31
1997 Mar 16	9.40	158	523.87 – 524.27
1997 Mar 17	0.53	17	524.87 – 524.90

Table 7.2 Photometric (Johnson B) amplitudes and phases of the frequency triplet

frequency (μHz)	amplitude (mmag)	phase[a] (radians)	P_1	P_2
1423.95	1.91 ± 0.05	1.00 ± 0.03		
1428.01	0.52 ± 0.05	-1.16 ± 0.10	6.9 ± 0.7	-0.07 ± 0.02
1432.07	1.66 ± 0.05	1.03 ± 0.03		

[a] The phases are shifted compared to the those given in Baldry et al. (1998c) due to a different phase reference point (see Section 7.3).

7.2.2 Photometry

For the last five years, astronomers at the South African Astronomical Observatory (SAAO) and the University of Cape Town (UCT) have been monitoring the oscillations in HR 3831 using high-speed photometry (Kurtz et al. 1997). We have selected a subset of their data which is centred on the time of our spectroscopic observations. These data were obtained on 26 nights (one hour of high-speed photometry per night) spanning the dates JD 2 450 402 to 2 450 618.

The photometry was analysed to find the amplitudes and phases of the frequency triplet (see Table 7.2) in order to compare with our spectroscopic results. The amplitudes of the triplet are within 2σ of the amplitudes from Kurtz et al. (1997). For further details, in particular showing the pulsation amplitude and phase as a function of rotation phase, see Baldry et al. (1998c).

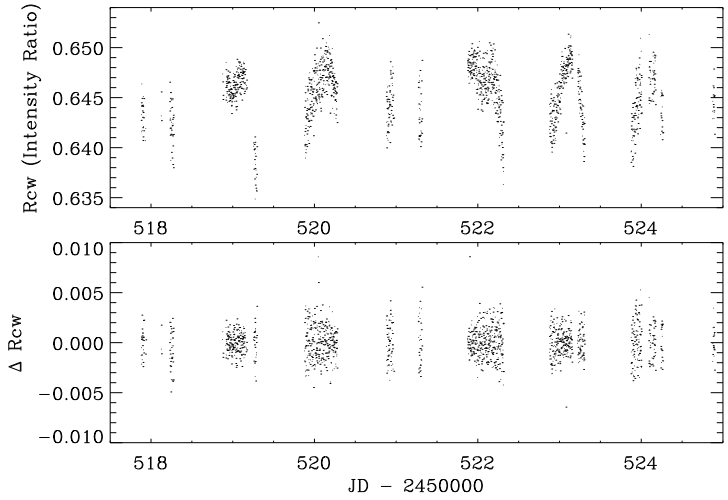

Figure 7.1 R_{cw} time series before and after high-pass filtering

7.3 Time-series analysis

To illustrate the various methods of analysing the time series for each spectroscopic observable, we look at an observable which has a high signal-to-noise ratio in the oscillation spectrum. This observable, called R_{cw}, is a ratio of the Hα core to wing intensity. In particular, we measured the intensity in a filter with FWHM$\sim$ 4Å divided by a filter with FWHM$\sim$ 31Å. This is similar to the R_{cw} measurements used in Chapter 6 and Baldry et al. (1998c) but using slightly narrower filters.

Each time series from the spectroscopic measurements was high-passed filtered and a few outlying points were removed. The R_{cw} time series before and after high-pass filtering is shown in Figure 7.1. There is a variation in the raw data of about 1 percent during the night. This is possibly due to varying contamination of the HR 3831 spectrum from its binary companion. As the pair of stars rotate in the coudé focal plane, there will be less contamination when the stars line up perpendicular to the slit and more contamination when the stars line up along the slit. Alternatively, the variation could be due to instrumental effects that are a function of elevation of the telescope. In either case, the change in the measured oscillation amplitude will be of the order of 1 percent over the night. This is not significant for our results, especially since there is no obvious systematic effect as a function of the rotation phase of HR 3831.

Next, a simultaneous fit of the frequency triplet and the first harmonic was made to the high-pass filtered data, using a weighted least-squares fitting routine. The amplitudes and phases were fitted, using the well-known frequencies (see Section 7.1.1), by the function $A\sin(2\pi\nu(t-t_0)+\phi)$ where $t_0 =$ JD 2 450 522.51746. Our phase reference point t_0 is equal to the reference point of Kurtz et al. (1997) plus 775 times $P_{\rm rot}$. This maintains the same relationship between the phases of the frequency triplet. The fit of the frequency triplet to the R_{cw} data is shown in Table 7.3 (the results for three sets of filters are shown).

Table 7.3 R_{cw} amplitudes and phases of the frequency triplet in HR 3831. The observable R_{cw} is the ratio between the mean intensity in a narrow filter with FWHM $F1$ and in a filter with FWHM $F2$ centred on Hα. For the three observables in this table, the average values are about 0.65 (see Figure 7.1 for the raw data in the second case).

$F1$ (Å)	$F2$ (Å)	frequency (μHz)	amplitude (ppm)	phase (radians)	P_1	P_2
2.9	23.5	1423.95	1340 ± 46	-0.82 ± 0.03	15.8 ± 4.7	$+0.02 \pm 0.02$
		1428.01	172 ± 45	-1.28 ± 0.27		
		1432.07	1386 ± 46	-0.78 ± 0.03		
3.9	31.4	1423.95	1334 ± 41	-0.71 ± 0.03	14.0 ± 3.5	-0.08 ± 0.02
		1428.01	177 ± 40	-1.58 ± 0.23		
		1432.07	1139 ± 41	-0.78 ± 0.04		
5.9[a]	45.1[a]	1423.95	1107 ± 41	-0.64 ± 0.04	12.4 ± 3.4	-0.10 ± 0.03
		1428.01	163 ± 41	-1.70 ± 0.25		
		1432.07	913 ± 41	-0.78 ± 0.05		

[a] This set of R_{cw} results uses the same filters as the R_{cw} results published in Baldry et al. (1998c). The results are slightly different due to a different weighting in the least-squares fitting routine, and there is also a change in phase reference point.

The R_{cw} oscillation amplitude spectrum is shown in Figures 7.2–7.3. Figure 7.3 shows that the frequency triplet is resolved, but with some aliasing or power shifting between the frequencies as can be seen from the spectral window. The amplitude of the spectral window at $\pm\nu_{rot}$ and at $\pm 2\nu_{rot}$ is about 20 percent. Also, the simultaneous fit gives amplitudes in ppm of 1330, 180 and 1140 for the triplet, whereas the amplitudes in the oscillation spectrum are 1100, 560 and 890 (note that ratio between A_{+1} and A_{-1} is about the same).

Another way to consider the aliasing is that the data have incomplete and biased sampling of the rotation phase of HR 3831. A good diagnostic of the data, and better for interpretation assuming that there is one mode that is amplitude modulated, is to plot the amplitude and phase of the pulsation (at ν_0) as a function of rotation phase. The data were divided into 20 separate time periods between 0.5 and 3.6 hours long and including between 17 and 107 spectra. For each time period, the amplitude and phase were measured at 1428.01 μHz. The R_{cw} results are shown in Figure 7.4. The two lines represent different fits to the data:

(i) The dashed line represents a modulation using the amplitudes and phases of the R_{cw} frequency triplet (from Table 7.3), which are from a six parameter fit to the complete time series. In other words, it shows the beating effect of the three close frequencies (ν_{-1}, ν_0, ν_{+1}). The good agreement between the modulation in amplitude and phase from the separate time periods and the modulation from the frequency triplet supports the accuracy of the simultaneous fit to the triplet.

(ii) The dotted line represents a fit which is obtained by scaling and phase shifting from

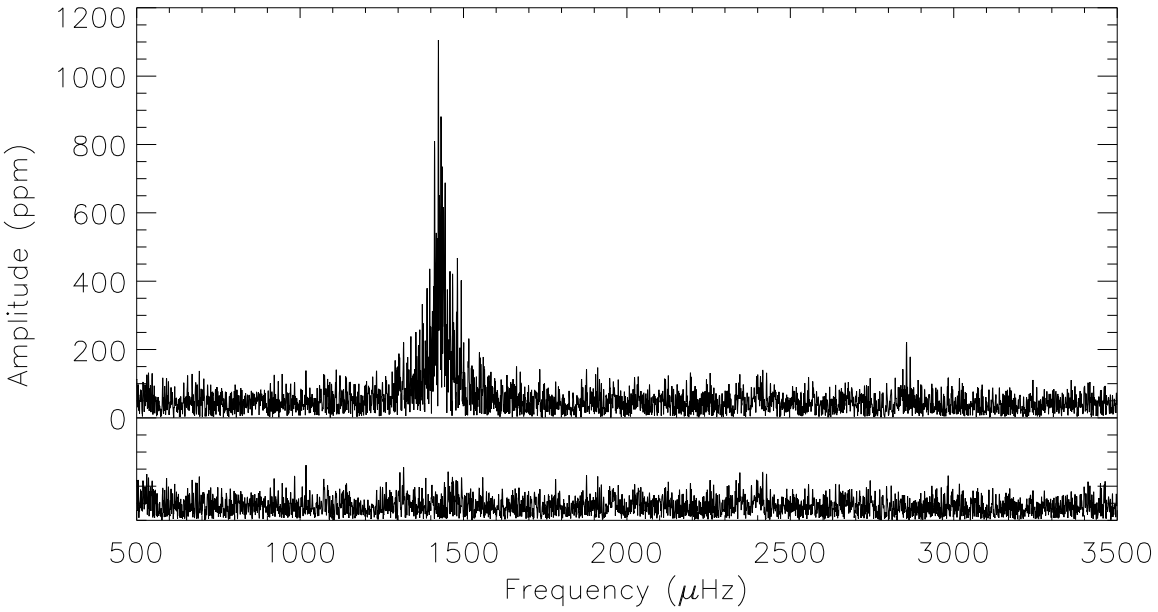

Figure 7.2 R_{cw} amplitude spectrum. The lower panel is the pre-whitened amplitude spectrum after subtracting a simultaneous fit of the frequency triplet and the harmonic.

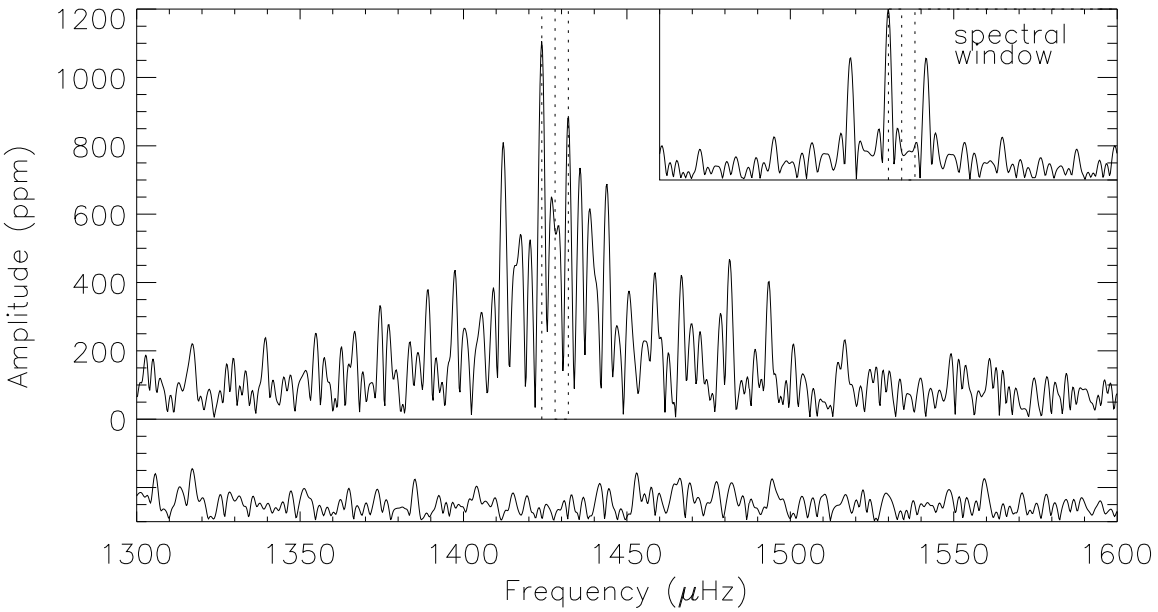

Figure 7.3 Close-up of Figure 7.2, with the dotted lines showing the frequencies of the triplet. The inset shows the amplitude spectrum of the window function on the same frequency scale, with the dotted lines having the same spacing as in the triplet.

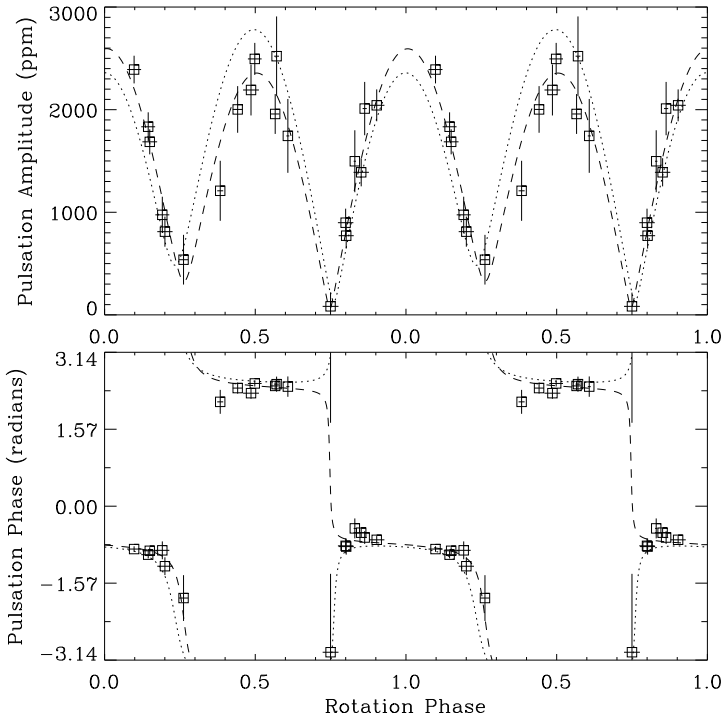

Figure 7.4 R_{cw} amplitude and phase of the central frequency as a function of rotation phase. The squares represent the data divided into 20 separate time periods between 0.5 and 3.6 hours long. The vertical lines are error bars, while the horizontal lines show the length of the time period. The dashed line represents a fit based on the measurement of the frequency triplet from the complete time series, and the dotted line represents a fit which is scaled and phase shifted from the photometric frequency triplet. Note that the data are plotted twice.

the photometric analysis of the triplet (from Table 7.2), in effect, a two parameter fit to the amplitudes and phases of the separate time periods. The shape of the amplitude and phase modulation is the same as the beating effect of the photometric triplet, while one parameter is the scaling of the amplitude and the other parameter is the shift of the pulsation phase. In this case, a reasonable fit is obtained to the R_{cw} data.

In conclusion, we have clearly detected the triplet in the equivalent-width of Hα (using R_{cw}) with the amplitudes of the three components in about the same ratio as seen in photometry. The R_{cw} measurement, as in α Cir, provides a high signal-to-noise spectral measurement of the pulsation.

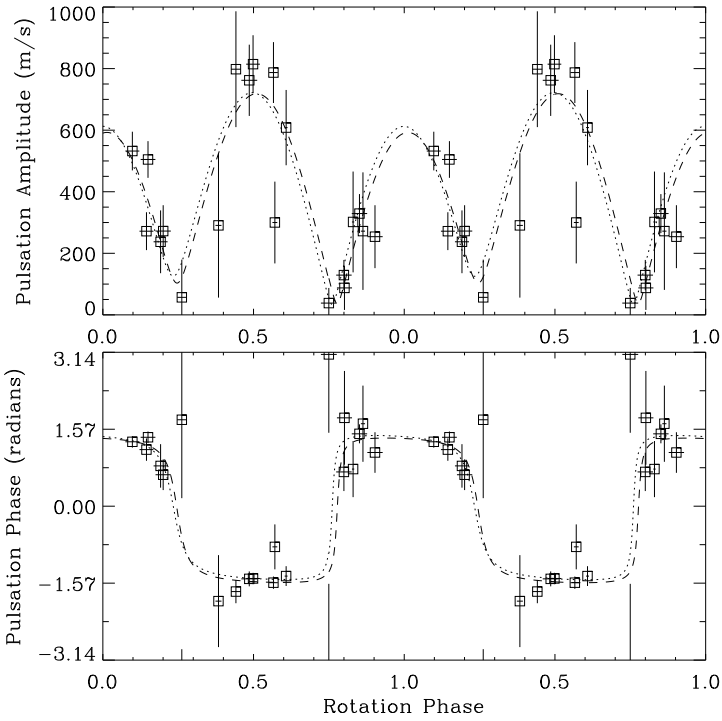

Figure 7.5 Hα velocity amplitude and phase of the central frequency as a function of rotation phase (band no. 87). The dashed line represents a fit based on the measurement of the frequency triplet from the complete time series, and the dotted line represents a fit scaled and phase shifted from the photometric frequency triplet. There is excellent agreement between the two fits, which supports the oblique pulsator model and rules out the spotted pulsator model.

7.4 Velocities of different wavelength bands

In this section, we look at the velocity amplitude and phase of different wavelength bands using a cross-correlation technique. The reduction method is the same as that used on α Cir (see Section 5.3.2), with a telluric band used as a velocity fiducial (Section 5.3.3). The spectrum of HR 3831 was divided into 90 bands, most having the same wavelength range as shown in Tables 5.3–5.4, the difference being that the spectrum of HR 3831 was taken from 6100Å to 7100Å, which is 100Å higher than the range used in the α Cir analysis. The results for 10 selected bands are shown in Table 7.4.

7.4.1 Hα velocity

First, we look at the Hα velocity as measured using the cross-correlation of band no. 87. This band should not be significantly affected by blending and has good signal-to-noise. The Hα velocity amplitude and phase as a function of rotation phase are shown in Figure 7.5. There is excellent agreement between the fit based on the measurement of the frequency triplet (Table 7.4) and the fit scaled and phase shifted from the photometric data

Table 7.4 Velocity amplitude and phases for selected wavelength bands using a cross-correlation technique. The bands selected were those having a combined signal-to-noise[a] ratio of greater than 9 for the frequency triplet, except only one band across the Hα line is included (band no. 87). A telluric band from 6864 to 6881Å is used as a velocity reference (band no. 80).

band[b] range (Å)	frequency (μHz)	amplitude ($m\,s^{-1}$)	phase (radians)	P_1[c]	P_2	Fig.
no. 13	1423.95	377 ± 51	0.82 ± 0.13			
	1428.01	92 ± 50	-0.67 ± 0.57	—	-0.18 ± 0.12	B.3
6140.6–6150.9	1432.07	260 ± 51	0.89 ± 0.20			
no. 14	1423.95	524 ± 61	2.45 ± 0.12			
	1428.01	26 ± 61	—	—	-0.32 ± 0.12	B.4
6152.9–6164.6	1432.07	273 ± 61	2.41 ± 0.23			
no. 18	1423.95	1108 ± 69	0.07 ± 0.06			
	1428.01	228 ± 68	-1.33 ± 0.30	6.6 ± 2.3	-0.48 ± 0.07	7.8
6194.0–6197.5	1432.07	392 ± 69	0.09 ± 0.18			
no. 33	1423.95	1140 ± 62	0.54 ± 0.05			
	1428.01	222 ± 62	-0.96 ± 0.28	7.6 ± 2.4	-0.34 ± 0.05	B.5
6325.8–6333.2	1432.07	556 ± 62	0.46 ± 0.11			
no. 42	1423.95	600 ± 64	1.26 ± 0.11			
	1428.01	118 ± 64	-0.77 ± 0.57	—	-0.13 ± 0.09	B.6
6414.0–6422.9	1432.07	458 ± 64	0.70 ± 0.14			
no. 54	1423.95	348 ± 60	1.64 ± 0.17			
	1428.01	88 ± 60	-0.44 ± 0.75	—	$+0.10 \pm 0.11$	B.8
6521.8–6528.2	1432.07	423 ± 60	1.62 ± 0.14			
no. 58	1423.95	1378 ± 132	2.36 ± 0.10			
	1428.01	131 ± 131	-0.47 ± 1.49	—	-0.60 ± 0.13	B.9
6596.3–6607.1	1432.07	346 ± 132	2.83 ± 0.39			
no. 81[d]	1423.95	63 ± 12	-2.59 ± 0.19			
	1428.01	16 ± 12	1.99 ± 0.80	—	$+0.03 \pm 0.13$	B.10
6881.5–6901.6	1432.07	68 ± 12	2.54 ± 0.18			
no. 87[e]	1423.95	343 ± 22	1.58 ± 0.06			
	1428.01	94 ± 22	-0.81 ± 0.24	6.9 ± 1.8	-0.05 ± 0.05	7.5
6545.4–6578.2	1432.07	309 ± 22	1.42 ± 0.07			
no. 90[f]	1423.95	743 ± 87	0.95 ± 0.12			
	1428.01	116 ± 87	-1.15 ± 0.84	—	-0.35 ± 0.12	B.12
7070.2–7079.5	1432.07	357 ± 87	1.28 ± 0.25			

[a] The rms-noise is about 1.38 times the formal 1σ error on the amplitude measurements.
[b] The band number relates to the bands used in Chapter 5.
[c] Only the bands where the central amplitude is higher than 2σ are included. For the other bands, the error in this parameter is large and significantly non-gaussian.
[d] This band contains a significant number of telluric lines, see discussion in Section 5.5.1.
[e] This band represents the velocity of the Hα line. These results are different to those published in Baldry et al. (1998c) because the band is wider and the telluric band used as a reference is different.
[f] This is a new band not included in Chapter 5.

(Table 7.2). This supports the oblique pulsator model and rules out the spotted pulsator model. In the latter model, the pulsation velocity amplitude and phase should be constant during the rotation of the star, which is clearly not the case.

The excellent agreement between the Hα velocity and photometry, in terms of the relative modulation as a function of rotation phase, is reflected in the fact that the parameters P_1 and P_2 are nearly the same between the two time series (compare Table 7.2 with band 87 from Table 7.4). Within the oblique pulsator model, these parameters are expected to be the same for different observables (see Section 7.1.1). If the frequency triplet were caused by three different modes, then the ratios between the amplitudes of the modes (quantified by P_1 and P_2) would be expected to vary depending on the observable. Therefore, this agreement between the Hα velocity and photometry argues in favour of the oblique pulsator model rather than for different modes. However, this is a weak argument because the amplitude ratios could be nearly the same even in the case of different modes. The main arguments against different modes come from the years of photometric analysis of HR 3831 (e.g, Kurtz et al. 1990, 1993, 1994a, 1997): (i) the frequency splitting is exactly or nearly exactly the rotation frequency (see Section 7.1), and (ii) the ratios between the amplitudes of the frequency triplet has remained nearly constant over time. For these reasons, it is considered unlikely that the observed frequency triplet in HR 3831 is caused by different modes, in particular rotationally perturbed m-modes.

In Baldry et al. (1998c), we noted a possible rotational phase lag between the radial velocity (RV) amplitude maximum and the photometric amplitude maximum, of about 0.06 rotation cycles. However, from the results shown in Figure 7.5, the RV maximum and photometric maximum are within 0.02 rotation cycles of each other. The change from the earlier results arises from the use of a different telluric reference wavelength region. In Baldry et al. (1998c), a large region from 6865 to 6931Å was used, which included band nos. 80, 81 and 82, in order to maximise the signal-to-noise ratio. In this chapter, we find a significant signal arising from the wavelength region of band 81 (see Table 7.4) and this is likely to be the cause of the phase lag noted in Baldry et al. (1998c). Band 80 is used as the telluric reference band in this chapter. The justification for using this band is that it has the lowest percentage (about 2%) of absorption that is attributable to lines from the star (see discussion in Section 5.5.1). To summarise, the Hα RV amplitude is better represented by the results in this chapter, whereas the results in Baldry et al. (1998c) are slightly contaminated by metal lines around band 81.

7.4.2 Metal lines

The velocity amplitude and phase in HR 3831 varied significantly between different wavelength bands, as was seen in α Cir (Chapter 5). Figures 7.6–7.7 show the amplitude versus phase for the 26 metal bands with the highest signal-to-noise ratios (plus one band across Hα) in HR 3831. The results measured at the frequencies ν_{-1} and ν_{+1} are plotted separately, while the amplitude and phase of ν_0 are not plotted because the signal-to-noise ratio is significantly lower at this frequency. There are two aspects to the results which we will consider: the modulation of the measured pulsation with rotation and the variation of the amplitude and phase between different wavelength bands. The first is characterised

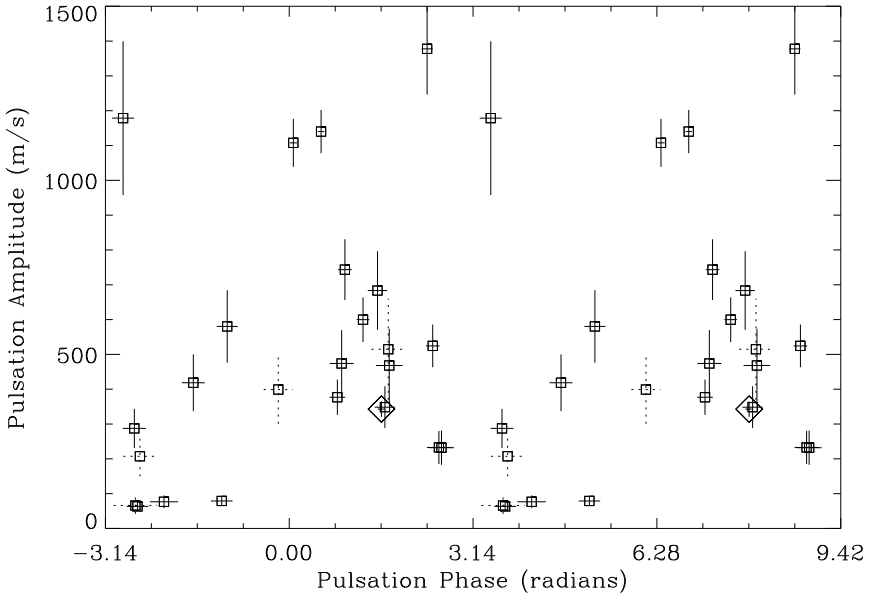

Figure 7.6 Velocity amplitudes and phases measured at the frequency ν_{-1} in HR 3831 for different wavelength bands. Bands with S/N greater than 3 are plotted with solid lines, those with lower S/N use dotted lines. The same 27 bands are plotted in Fig. 7.7, chosen so that the *combined* S/N is greater than 5. Only one band across Hα is included, which is shown using a diamond. Note that the data are plotted twice for clarity.

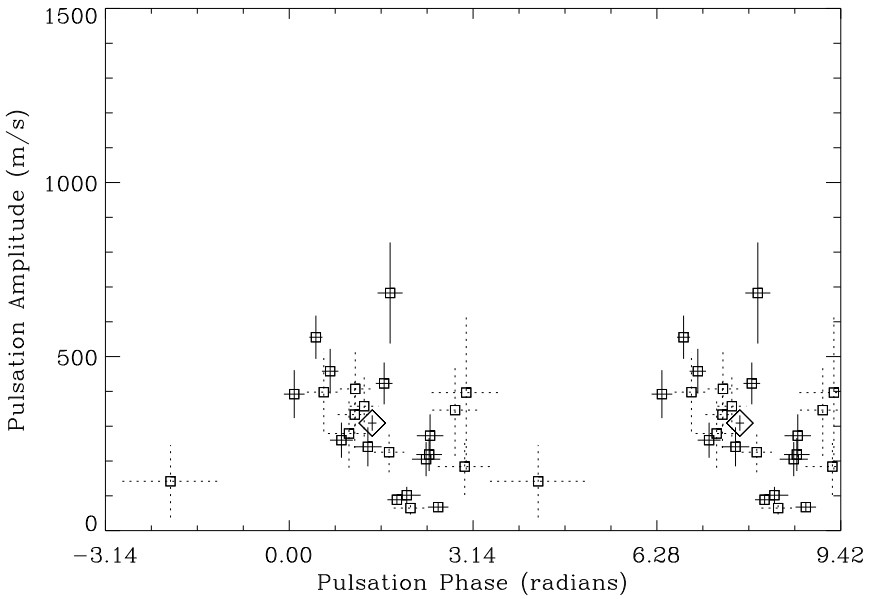

Figure 7.7 Same as Figure 7.6, but for the frequency ν_{+1}.

by the difference in amplitude and phase between ν_{-1} and ν_{+1}.

Rotational modulation

There is a significant difference between the results for ν_{-1} (Fig. 7.6) and ν_{+1} (Fig. 7.7). Firstly, the amplitudes vary between 0 and 1500 m s^{-1} for ν_{-1}, whereas the amplitudes for ν_{+1} are all below 800 m s^{-1}. Secondly, the phases range across 2π for ν_{-1}, while the phases for ν_{+1} range between 0 and π except for one low S/N band. This is not as expected from the oblique pulsator model. In this model, for each band, the phase of ν_{-1} and ν_{+1} should be the same and the amplitudes should be nearly the same ($A_{+1} \approx 0.87 \times A_{-1}$ from Table 7.2). Therefore, these results suggest that the two frequencies measured are separate modes, rather than rotational 'side lobes' of one principal mode. However, there is strong evidence for the oblique pulsator model as described in Section 7.4.1. Therefore, we need to consider another explanation within the framework of the oblique pulsator model. We first look at some selected bands, in terms of their modulation of amplitude and phase with rotation.

Recall that the oblique pulsator model involves parameters P_1 and P_2 (Eqs. 7.2 & 7.3). All the measured spectroscopic observables in this chapter produce values for P_1 that are within 3σ of the photometric value. There are large errors in this parameter because it depends critically on the amplitude measured at ν_0, which is typically less than two or three times the noise level in our data. The parameter P_2 does vary significantly between different observables. It can be measured with higher accuracy since it does not depend on the small central amplitude. From the measured velocity amplitudes, there are three spectral bands (18, 33 and 58) that have values of P_2 that are formally 4–5σ different from the photometric value (see Table 7.4). To test whether this is a significant change or just a product of aliasing, we looked at the modulation in velocity amplitude and phase as a function of rotation phase. Figure 7.8 shows this modulation for band 18. While the amplitude modulation could be fitted reasonably well by scaling from the photometry, the discrepancy is obvious with the phase modulation. There is a noticeable pulsation phase change from rotation phase 0.8 through 1.0 to 0.2, while the photometric phase is nearly constant. Similar effects are evident from bands 33 and 58 (see Figures B.5 and B.9).

As well as the parameters P_1 and P_2, which relate the amplitudes of the frequency triplet, there are also phase differences between the frequencies. For many bands, there is significant difference between the phases measured at ν_{+1} and ν_{-1}. In our measurements, the equality of phase ϕ_{+1} and ϕ_{-1} means that the amplitude maxima occur at rotation phases 0.0 and 0.5 with phase jumps in between. Therefore, any phase difference $\phi_{+1} - \phi_{-1}$ implies that there is a shift of the amplitude maxima. For example, there is a small shift in the amplitude maxima of band 42 (Figure B.6) and larger shifts, but with low signal-to-noise, of bands 48 and 82 (Figures B.7 and B.11).

These results are not sufficient evidence to discard the oblique pulsator model, because they could be explained by variations in the ratios between the metal lines in the bands, due to spots, as the star rotates. Alternatively, there is a possibility that there is an actual change in the pulsation phase and amplitude (as opposed to a pseudo-change caused by a variation in blending) associated with spots on the star. So while the spotted pulsator

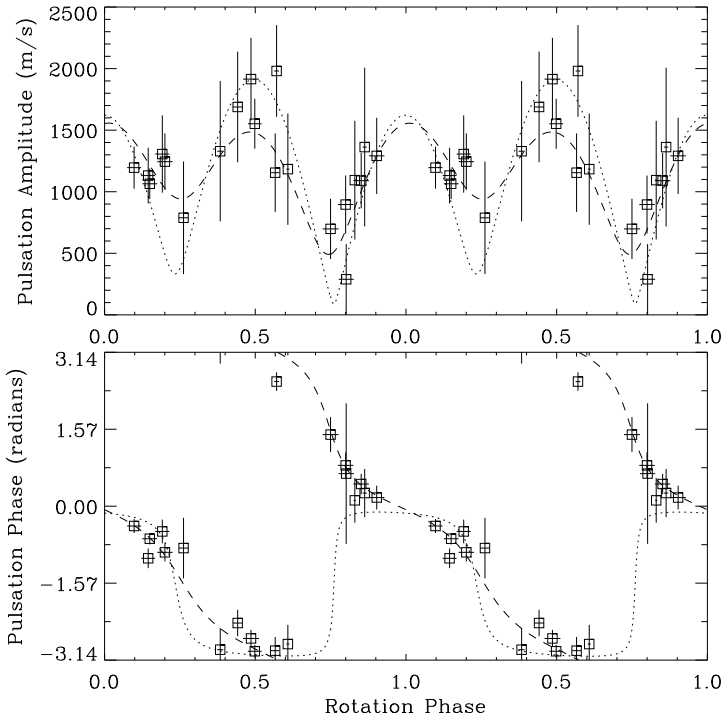

Figure 7.8 Velocity amplitude and phase of band no. 18 as a function of rotation phase. The dashed line represents a fit based on the measurement of the frequency triplet from the complete time series, and the dotted line represents a fit scaled and phase shifted from the photometric frequency triplet.

model is ruled out in its original form, spots may be having an influence on the pulsation.

Amplitude and phase variations between bands

In Chapter 5, it was suggested that the amplitude and phase variations between wavelength bands in α Cir could be explained by a radial node in the atmosphere. We see amplitude and phase variations in HR 3831 that are somewhat similar in the case of ν_{-1} (Fig. 7.6), and with smaller but still significant variations in the case of ν_{+1} (Fig. 7.7). However, there is no obvious division between two sets of bands that are pulsating in anti-phase with each other, as was seen in α Cir (Figure 5.8). If these HR 3831 results represent true velocity amplitudes and phases at various depths in the atmosphere, then an explanation that includes running waves is necessary. Alternative explanations could involve spots on the surface or blending, which causes the measured phase to deviate from the true velocity phase.

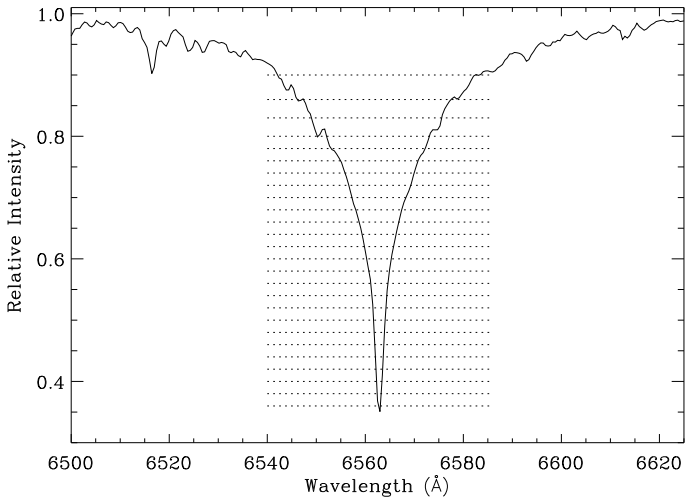

Figure 7.9 The Hα line in HR 3831. The dotted lines divide the 25 contiguous sections used in the bisector velocity and width analysis (Section 7.5).

7.5 Hα profile variations

The Hα line in each spectrum was divided into 25 contiguous horizontal sections, between relative intensities 0.35 and 0.9 (Figure 7.9). For each section, a bisector velocity (average position of the two sides) and a width were calculated. For the velocity measurements, a telluric band (no. 80) was used as a fiducial.

7.5.1 Bisector velocities

The velocity amplitude and phase of the pulsation as a function of relative intensity in the Hα line are shown in Figure 7.10, with measurements at frequencies ν_{-1} and ν_{+1}. The amplitudes and phases are in good agreement between the two frequencies, which means that the shape of the rotational modulation is similar for each velocity measurement. Figure B.13 shows the rotational modulation from the velocity at a height of 0.40. It is similar to the modulation from the cross-correlation velocity of Hα (Figure 7.5), but with about twice the amplitude. This is expected because the cross-correlation velocity is a weighted average of the bisector velocities and the velocity amplitude at 0.40 is higher than average.

The variation in amplitude and phase as a function of relative intensity (Fig. 7.10) is similar to that seen in α Cir (Fig. 6.2), particularly the drop in amplitude between heights 0.4 and 0.6 (a comparison is shown in Figure 8.2). However, assuming that the bisector line-shift represents the velocity at different heights in the atmosphere, we expect to see less relative variation in the bisector velocity amplitude in HR 3831 than α Cir. This is because the separation between radial nodes in the atmosphere is larger in HR 3831 due to the fact that it pulsates at a lower frequency and that the two stars have similar

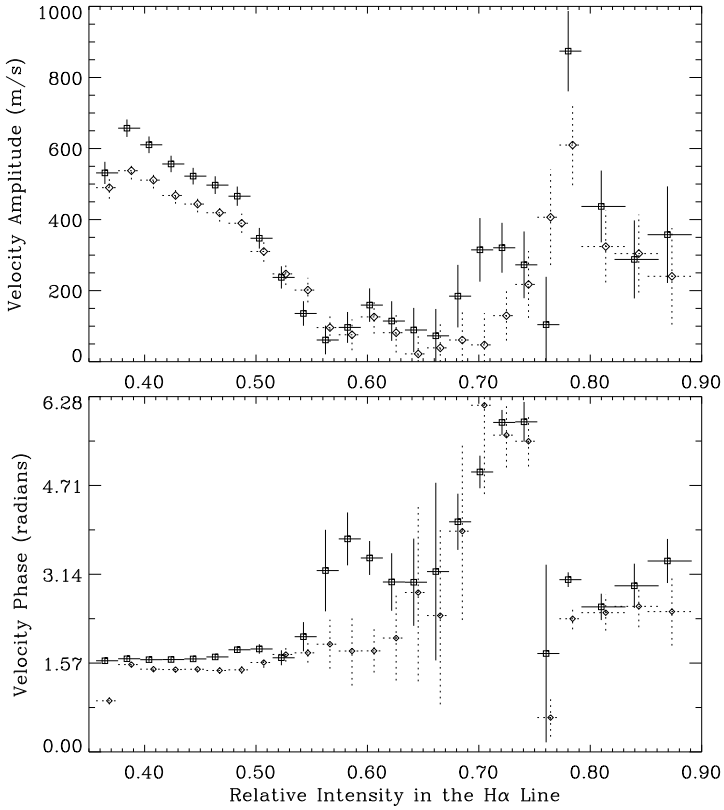

Figure 7.10 Amplitudes and phases of the pulsation for the bisector velocity at different heights in the Hα line. Squares with solid lines represent ν_{-1} and diamonds with dotted lines represent ν_{+1}. For each measurement, the vertical line is an error-bar while the horizontal line shows the extent of the section in the Hα line.

fundamental properties (see Sections 6.1.1 and 7.1.1). Two possible explanations are that: (i) the Hα line forming region in HR 3831 is more extended than in α Cir and coincidently the Hα bisector behaves in a similar way; (ii) the assumption that the bisector represents velocities at different heights is incorrect.

The variation in amplitude and phase is less similar to α Cir above a height of 0.7. For instance, there is a noticeable amplitude peak and phase reversal around 0.73 in the bisector of α Cir which is not evident in HR 3831. The bisector measurements above a height of 0.7 in α Cir are partially affected by blending (Section 6.3.2). Therefore, some of the differences in the bisector velocity results between the two stars are probably due to a difference in blending.

To summarise, there is no significant difference in the rotational modulation of the bisector velocity between various heights. For the measurements below a height of 0.7, the relative variation in amplitude and phase is very similar to that observed in α Cir, which is puzzling. At each height, the amplitudes at the two frequencies in HR 3831 are about twice the amplitude of the principal frequency in α Cir.

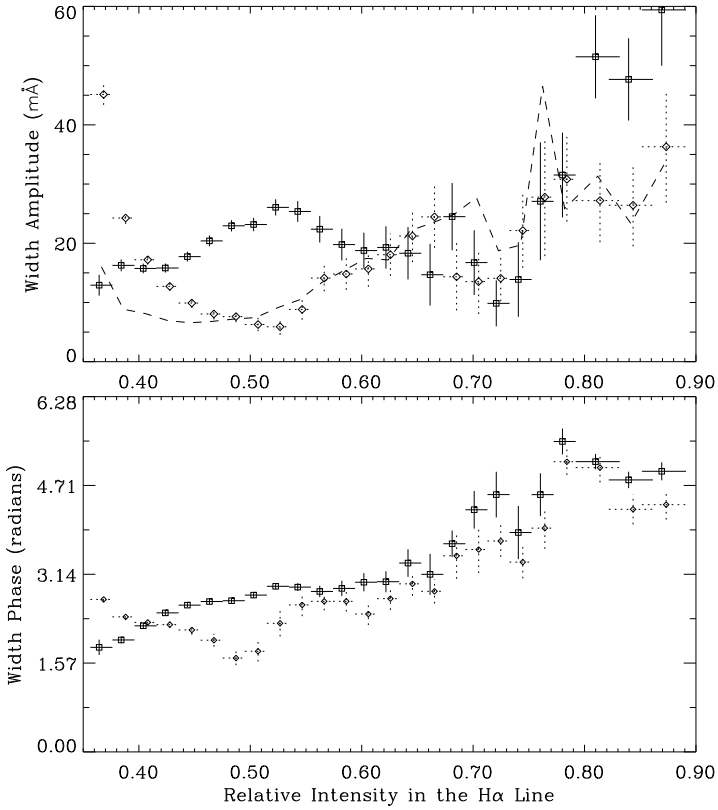

Figure 7.11 Amplitudes and phases of the pulsation for the width at different heights in the Hα line. Points with solid lines represent ν_{-1} and points with dotted lines represent the ν_{+1}. For each measurement, the vertical line is an error-bar while the horizontal line shows the extent of the section in the Hα line. The dashed line shows the effect on the width amplitude of an oscillation with an EW amplitude of 1000 ppm, with the profile variation described in Section 6.4.2. Note that 10 mÅ is equivalent to a dispersion of 457 m s^{-1} at Hα.

7.5.2 Widths

Changes in the width of the Hα line in HR 3831 at various heights are shown in Figure 7.11. The width amplitude and phase represent oscillations about a mean width, with measurements at two frequencies. These measurements are related to intensity and EW measurements, with the line resolved vertically rather than horizontally. The advantage of width measurements is that the width is naturally independent of the bisector velocity, i.e., the width is the difference in position between two sides of a line whereas the velocity is the average position. In order to compare with EW measurements, the dashed line shows the simulated width amplitudes for the profile variation described in Section 6.4.2 (see also Figure 6.6) with an EW amplitude of 1000 ppm (see Appendix A.3 for a width analysis of α Cir).

The most striking feature of Figure 7.11 is that there is such a difference in the measurements between the two frequencies. This means that, unlike for the bisector velocities,

the shape of the rotational modulation is varying between different heights. Three examples are shown to demonstrate the extremes (in terms of the parameter P_2) and the closest to the photometric modulation.

(i) Figure B.14 shows the modulation in width amplitude and phase at a height of 0.36. The pulsation width phase increases steadily during the rotation ($P_2 = 0.54 \pm 0.05$).

(ii) Figure B.15 shows the modulation at height 0.42. There is good agreement with the fit derived from the photometric triplet ($P_2 = -0.03 \pm 0.04$).

(iii) Figure B.16 shows the modulation at height 0.53. The width phase decreases steadily during the rotation ($P_2 = -0.63 \pm 0.07$).

To check the lowest measurement at height 0.36, which is sensitive to intensity changes in the core of the line, we took an intensity measurement using a filter with a full-width half-maximum of about 1Å. This measurement shows a similar rotational modulation with the parameter $P_2 = 0.33 \pm 0.03$ (Figure B.17). If we consider the two extremes, i.e., the width changes at heights 0.36 and 0.53: at rotation phases around 0.5 and 1.0 the width changes are in phase; whereas, at rotation phases around 0.25 and 0.75 they are in anti-phase. At both heights, the relative amplitude modulation (as defined by the dashed-line) is less than for other observables. Though we note that in the case of Figure B.14, the lowest data point deviates by 3–4σ deviation from the dashed-line.

If we look at Figure 7.11, the simple explanation is that we are seeing two modes that have different Hα profile variations. An alternative explanation — if HR 3831 is pulsating in an oblique mode — is that, as the star rotates, the profile variation modulates due to viewing different aspects of the same mode.

Chapter 8

RoAp stars: further discussion and conclusions

8.1 Velocity amplitudes and phases

8.1.1 Another case: γ Equ

Kanaan & Hatzes (1998) observed radial velocity variations in the roAp star γ Equ. Their observations consisted of high-resolution spectra in the range 5000–6000 Å, covering 3.5 h on 13 September 1994. There are four modes in the range 1330–1430 μHz (Martinez et al. 1996), which are unresolved in that data set. Kanaan & Hatzes fitted a sine curve of fixed frequency (1380 μHz), but variable amplitude and phase, to the velocity measurements of each individual line, effectively treating the modes as a single pulsation. They discovered that the velocity amplitude varied significantly from line to line (see Chapters 5 and 7 for similar results on α Cir and HR 3831).

We analysed some of these results on γ Equ from Table 1 of Kanaan & Hatzes (1998) in order to compare with the results on α Cir and HR 3831. From the table, which consisted of 70 metal lines, we took the amplitude A (m/s), σ_a (m/s) and the 'Time of Maximum' (JD). Note that the times of maximum quoted by Kanaan & Hatzes cover several pulsation cycles. We converted the times to phases using the pulsation period of 0.008387 d, and the phases were shifted so that a weighted mean was approximately zero. The phase error was taken to be the arcsin (σ_a/A). This phase error is in good agreement with the σ_b (days) quoted in their table for lines where A/σ_a is greater than 2. Fig. 8.1 shows amplitude versus phase for the 19 lines with the highest signal-to-noise ratio. The higher amplitude bands, plotted with solid lines, cover a range of 0.8 radians in pulsation phase (-0.26 to $+0.54$ in the figure). This is significantly less than the variation in phase seen in α Cir (Fig. 5.7) and HR 3831 (Fig. 7.6), where the bands cover virtually the whole range of phases (2π). Note that the rms-noise level in an oscillation spectrum is about $1.38\sigma_a$, therefore, $A/\sigma > 4$ is comparable to $A/\mathrm{noise} > 3$.

The difference between the results on γ Equ (Kanaan & Hatzes) and results on the other two roAp stars (this thesis), in terms of the variation in phase between different metal bands, could be due to: (i) wavelength region studied, 5000–6000 vs. 6000–7000,

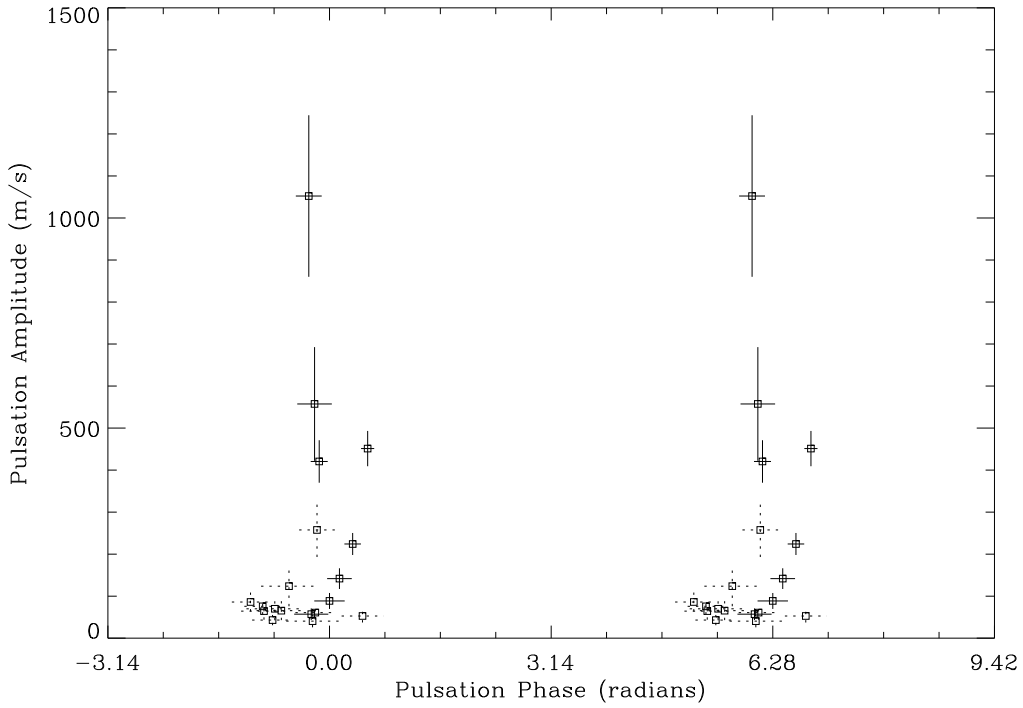

Figure 8.1 Amplitudes and phases of the pulsation in γ Equ for different metal lines, using results from Kanaan & Hatzes (1998). Lines with A/σ_a greater than 4 are plotted with solid lines, those with $2.5 < A/\sigma_a < 4$ are plotted with dotted lines. Note that the data are plotted twice for comparison with Figs. 5.7, 5.10, 7.6 and 7.7.

(ii) spectrograph resolution, 0.2Å vs. 1.5Å, (iii) pulsational characteristics of the star. Further high-resolution studies of these roAp stars will be able to distinguish among these causes.

8.1.2 Depth and surface effects

What are the causes of the velocity amplitude and phase variations, and of the Hα bisector variations?

The main hypothesis is that there is a significant change in pulsation amplitude and phase with geometric depth in the atmosphere of an roAp star, with a radial node of a standing wave situated in the observable atmosphere. Absorption lines are formed at different depths and therefore sample different parts of the standing wave. This can explain a complete range of observed amplitudes plus a phase reversal.

An alternative hypothesis for these variations is that the amplitude and phase of a non-radial pulsation mode will vary over the surface of a star, and that each spectroscopic observable is related to an integral over the surface. Therefore, if the integrals are sufficiently different between observables, the measured amplitude and phase may vary significantly. These variations could be related to limb-darkening and / or spots.

Neither hypothesis can fully explain the range of phases seen in α Cir and HR 3831. There may be blending effects that cause deviations from the true velocity phases on top of the atmospheric depth or surface effects. The argument for this is quite strong given that less phase variations are seen in the high-resolution results of γ Equ, but as pointed out above, there may be other causes. Blending can be considered as blurring the distinction between velocity and temperature changes in a star.

Surface effects would be a good explanation if roAp stars were pulsating in modes with $\ell \geq 3$ because, for these modes, there are several patches on the surface that have alternating phase. However, the frequency triplets in many roAp stars suggest that dipole modes are predominant ($\ell = 1$). For these modes, the measured velocity amplitude and phase is not expected to vary significantly between different observables (due to surface effects), e.g., for a dipole mode with an axis that is aligned near to our line-of-sight, the pulsation phase will be the same across most of the viewed surface.

The main arguments for depth effects being the principal cause of the amplitude and phase variations are (i) that a radial node is plausibly situated in the observable atmosphere (Gautschy et al. 1998, Appendix A.2), and (ii) that the bisector velocity varies with height in the Hα line. In Section 6.3.3, we discussed the possibility of systematic errors causing the bisector velocity variations. Here, we make a simple calculation to test the accuracy of these velocities below a relative intensity of 0.7 in the line.

For α Cir and HR 3831 (ν_{-1} and ν_{+1}), we averaged the bisector-velocity amplitudes below a height of 0.7 (giving half weight to the amplitudes between 0.6 and 0.7) in order to compare with the cross-correlation measurements. This is a plausible estimate for the cross-correlation because the slope of the Hα profile is steep and nearly constant between 0.4 and 0.6, and is less steep above 0.6. For α Cir, we obtained an estimate of $\sim$170 m s^{-1} while the actual cross-correlation measurements gave 168–182 m s^{-1} (depending on the band, nos. 85–88). For HR 3831, we obtained estimates of $\sim$340 and $\sim$290 m s^{-1} for the two frequencies while the actual measurements gave 338–361 and 296–318 m s^{-1} respectively. The good agreement, between the estimates obtained from the bisector analysis and the velocity amplitudes from the cross-correlation measurements (using four different bands), argues that the bisector velocities are accurate.

However, there is a similarity between the α Cir and HR 3831 bisector results (see Figure 8.2) that is possibly inconsistent with depth effects being the cause of the bisector variations. This is because the pulsations of these two stars have significantly different periods (7 and 12 minutes) and, therefore, have different vertical wavelengths, assuming that the sound speed is approximately the same between their atmospheres. If depth effects are causing the bulk of the observed bisector variations, the Hα line is formed over a larger vertical distance, and/or the sound speed is lower, in the atmosphere of HR 3831.

Again, surface effects could explain the bisector variation in α Cir and HR 3831 if they were pulsating in modes with $\ell \geq 3$ (see Hatzes 1996). Therefore, we are left with two relatively straightforward explanations for the amplitude and phase variations: (i) they pulsate in dipole modes and the variations are caused by depth effects, or (ii) they pulsate in $\ell = 3$ modes and the variations are caused by surface effects. A more complicated explanation could involve a combination of standing waves, running waves, surface effects, distorted modes and blending.

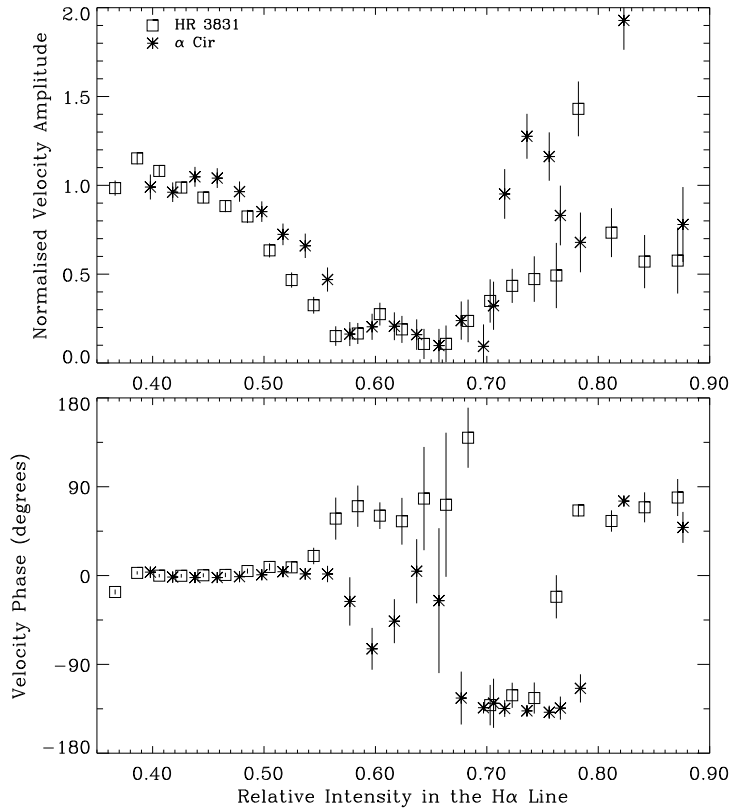

Figure 8.2 Comparison of the Hα bisector variations between HR 3831 and α Cir. This figure is essentially an overplot of Figures 7.10 and 6.2 except, for HR 3831 the measurements for ν_{-1} and ν_{+1} were averaged and, for α Cir the Stromlo and La Silla data were combined. Additionally, the amplitudes were normalised by dividing by an average taken between heights 0.40 and 0.45 (519 m s^{-1} for HR 3831 and 267 m s^{-1} for α Cir) and the phases were shifted.

8.2 Rotational modulation in HR 3831

There are many examples of rotational modulation shown in Chapter 7 and in Appendix B.2. The large variation in the shape of the modulation between different observables was an unexpected result. There are three possible explanations that we will describe here.

(i) The observed frequency triplet is caused by three different modes.

(ii) The oblique pulsator model is accurate and the variations are caused by 'systematic errors' in the measurements.

(iii) The oblique pulsator model is correct but needs to be modified to include effects due to spots or some other mechanism.

In the first case, the relative amplitude between different modes would be expected to vary for different observables. This is the natural explanation for the differences between ν_{-1} and ν_{+1} of the metal-line velocity amplitudes and phases (Figures 7.6 and 7.7) and of the Hα-width amplitudes and phases (Figure 7.11). However, it would require some rotational phase-locking process to account for the frequency separations being equal to the rotation frequency.

In the second case, no simple systematic error could explain the variation in the shape of the rotational modulation. Any such error would need to be varying with the rotation. For instance, a variation in blending could possibly account for the rotational modulation of the metal-line amplitudes and phases, but it could not account for the Hα-width variations.

For the third case, we consider the Hα line because it is the least affected by blending. First, note that the intensity modulation, using a filter with a FWHM of about 6Å, is fitted well by the rotational modulation derived from the photometric triplet (Figure B.18). This means that the *total intensity* variations below a height of about 0.62 are in agreement with the oblique pulsator model. The bisector velocities are also in agreement, so it is just the width variations below 0.62 that are not in agreement with the model. Perhaps this could be explained by hot spots in the upper atmosphere that cause temperature amplitude and phase differences and, as the star rotates, the effect on the Hα profile varies; i.e., a spotted oblique pulsator model.

8.3 Future work

It is clear that the high-resolution study (R$\gtrsim$40000) of different metal lines will be necessary to improve the understanding of the pulsation and the structure of the atmosphere in roAp stars, because of the problems associated with blending at lower resolution ($R \sim 5000$ in this thesis). It will then be possible to compare the velocity amplitudes and phases between different atoms and ionization states. Theoretical work needs to be done to calculate formation depths for individual lines, including the effects of diffusion and the magnetic field. The aim is to build up a coherent picture of the pulsation in the atmosphere.

Of the results on roAp stars in this thesis, the Hα profile measurements are least affected by blending and cannot easily be improved using high-resolution spectroscopy. The profile measurements require a good continuum fit across the Hα line, which is about 100Å wide in these A-stars. For this reason, a spectrum which is stable across at least 400Å is preferable. This is harder to obtain with high-resolution spectroscopy due to the blaze-pattern and the size of CCD detectors. Although improvement could be made on the results using intermediate-resolution spectroscopy ($R \sim$15000), modelling the formation of the Hα line is more important. Determining depth and surface effects on the Hα profile will complement high-resolution spectroscopic and theoretical studies of metal lines.

Photometric oscillation spectra could be considerably improved from observations of roAp stars using small space telescopes. Two such missions plan to include roAp stars as part of a project to measure oscillations in nearby stars (MONS, see Baldry 1998; and MOST, `http://www.astro.ubc.ca/MOST/`). If successful, it will result in the detection of new modes and improved asteroseismology of the brightest roAp stars.

The spectroscopic study of the pulsations in roAp stars has produced more questions than answers, due to the complexity of the observed spectral changes. For the same reason, the 'amount of information' obtainable is very large (e.g., variations in amplitudes and phases) compared to other pulsating stars. Therefore, roAp stars are prime stellar objects for testing diffusion, magnetic field and pulsation theories. In the future, the study of rapidly oscillating Ap stars may proceed rapidly, oscillating between theoretical and observational advances.

Appendix A

A.1 Spectra of α Cir

In May 1996, I observed α Cir using the coudé spectrograph on the 74-inch Telescope at Mt. Stromlo. During two weeks, 4900 spectra were obtained with a wavelength range of 6000–7000Å and with a resolution of about 1.5Å (see Chapters 5–6 for results based on these spectra).

The template spectrum is shown in Figures A.1 and A.2. The S/N in this spectrum is over 1000 per pixel, though the continuum level is only accurate to about 0.01 and is less accurate in the regions specified.

The medium-resolution spectra have very little real continuum especially redward of Hα. Therefore, Jaymie Matthews (private communication) suggested that blending could have a significant effect on the measurement of the Hα bisector in α Cir (see Section 6.3.2 for discussion). In March 1997, I took some high-resolution spectra of α Cir, using with the coudé echelle spectrograph on the 74-inch Telescope. In order to determine which metal lines could affect the Hα profile, I reduced the two orders including Hα. The dispersion was about 0.05Å/pixel with a resolution of about 0.2Å. Part of the spectrum is shown in Figure A.3. The identification of the twenty most significant features is given in Table A.1. Above a relative intensity of 0.8 in the Hα line (referring to the intensity in the reduced medium-resolution spectra), the features C, F, Q, S and T contain metal lines which affect the profile. Below 0.8, only one feature is identified with a metal line, feature O containing Fe I 6569.2Å (rest wavelength) and a telluric line. The centre of Hα was measured to be at 6562.5Å, giving a Doppler shift of $-14\,\mathrm{km\,s^{-1}}$ for α Cir.

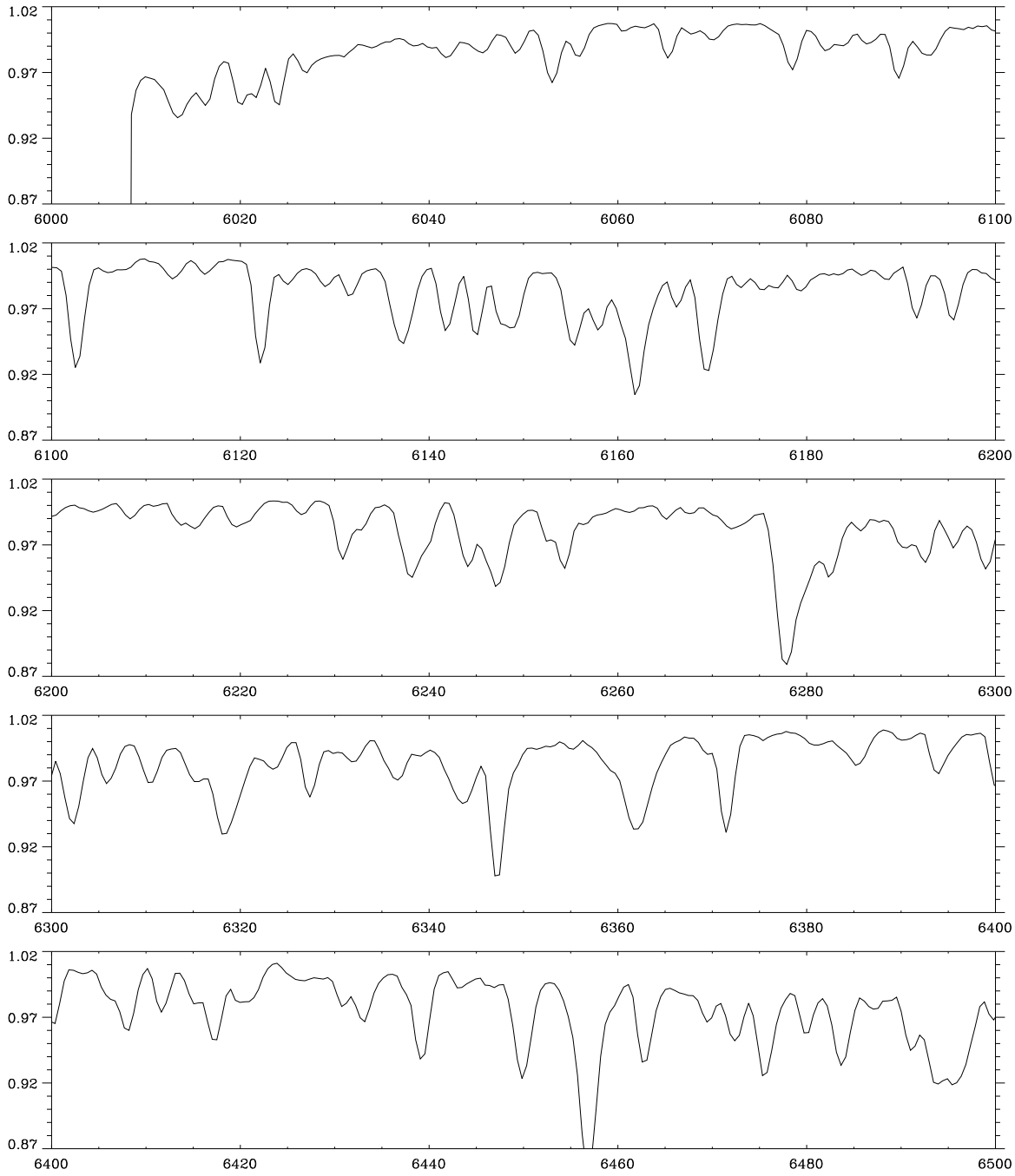

Figure A.1 Spectrum of α Cir from 6000 to 6500Å , taken with a medium resolution (~ 1.5Å) spectrograph at Mt. Stromlo. Note that the continuum fit is not accurate below 6050Å.

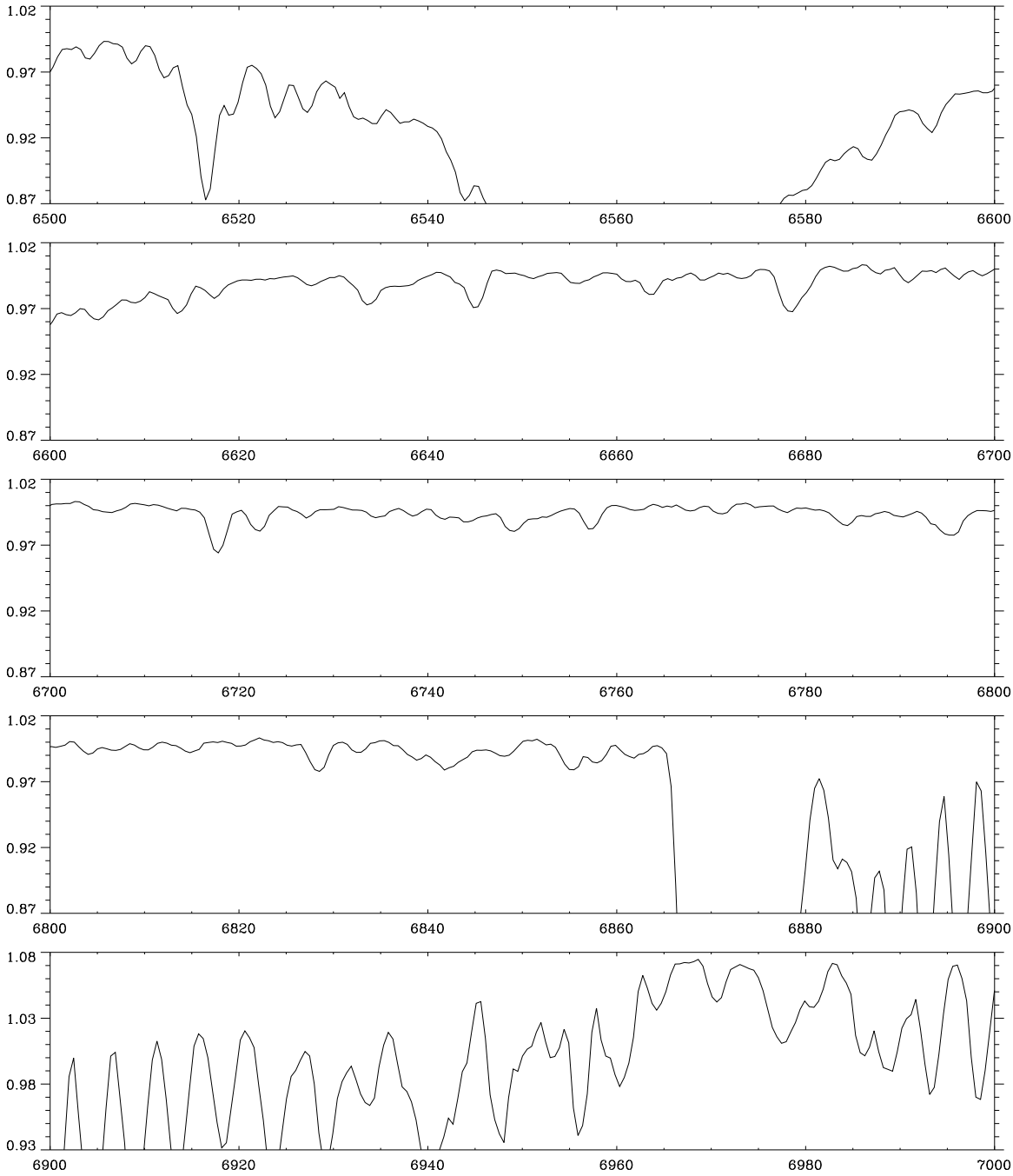

Figure A.2 Spectrum of α Cir from 6500 to 7000Å — continuation of Figure A.1. Note that the continuum fit is not accurate above 6900Å. The y-scale for this region is slightly shifted as a result.

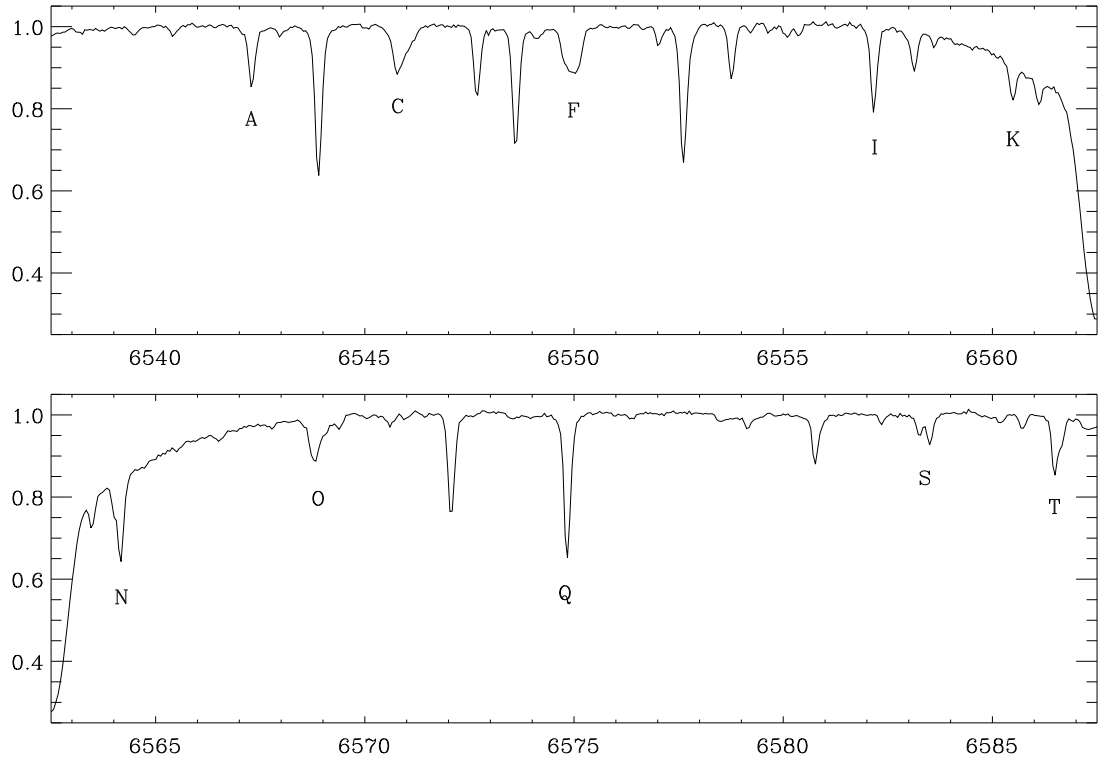

Figure A.3 Spectrum of α Cir within $\pm$25Å of the centre of Hα (6562.5Å), taken with a high resolution (~ 0.2Å) echelle spectrograph at Mt. Stromlo. The two panels are taken from different orders, with the intensity normalised by a fit made to the Hα wings below 6555 in the upper panel and above 6570 in the lower panel. Therefore, the intensities cannot be compared with the Hα line shown in other figures in this thesis, e.g. Figs. 6.1 and 6.3. This plot was used to identify the telluric and metal lines blending with Hα (see Section 6.3.2 and Table A.1). The letters A–T refer to the features in the Table.

Table A.1 Identification of absorption lines within the Hα profile of α Cir. For the twenty most significant features from the high resolution spectrum shown in Fig. A.3, the metal lines were identified using the synthetic spectrum calculated by Friedrich Kupka (private communication) and the telluric lines were identified using an atlas of the solar spectrum (Moore et al. 1966). Note that rest wavelengths are quoted and that the stellar spectrum of α Cir is shifted by about -0.3Å in this wavelength region.

feature	main line	other line
A	telluric 6542.31	
B	telluric 6543.91	
C	Fe I 6546.24	Mg II 6545.99
D	telluric 6547.70	
E	telluric 6548.62	
F	Sr I 6550.24	telluric 6550.28
G	telluric 6552.63	
H	telluric 6553.78	
I	telluric 6557.17	
J	telluric 6558.15	
K	telluric 6560.55	
L	telluric 6561.10	
M	telluric 6563.52	
N	telluric 6564.21	
O	Fe I 6569.22	telluric 6568.81
P	telluric 6572.09	
Q	telluric 6574.85	Fe I 6575.02
R	telluric 6580.78	
S	Si I 6583.71	telluric 6583.26
T	Fe II 6586.70	telluric 6586.51

A.2 Atmospheric model of α Cir

In this section, I analyse an atmospheric model of α Cir supplied by Friedrich Kupka (private communication). Even though the model is not accurate due to the complexity of Ap star atmospheres, it can be used to test the feasibility of radial nodes situated in the observable atmosphere (see Chapters 5–6 for observational results on α Cir).

Figures A.4–A.6 show various quantities versus geometric depth in the atmospheric model. The continuum emission is formed at around a depth of 4200 km from the defined 'surface' of the star (Fig. A.5).

The distance between nodes of a standing wave is equal to $v/2f$, where v is the sound speed and f is the frequency of the pulsation (2442 μHz for α Cir). I numerically integrated $1/v$ with respect to the geometrical depth (D) in order to find the positions of the radial nodes in the atmosphere.

$$N(D) = 0.5 + 2f \int_0^D \frac{1}{v(D')} \, \mathrm{d}\, D' \tag{A.1}$$

where integer values of N represent nodes and the surface of the star is assumed to be an anti-node ($N = 0.5$). Figure A.7 shows the positions of 3 nodes in the atmospheric model, of which one is at a depth of about 3400 km and probably in the line-forming region of the atmosphere. Even though this model is not an accurate description of an Ap star atmosphere, it shows that the hypothesis of radial nodes situated in the observable atmosphere is reasonable.

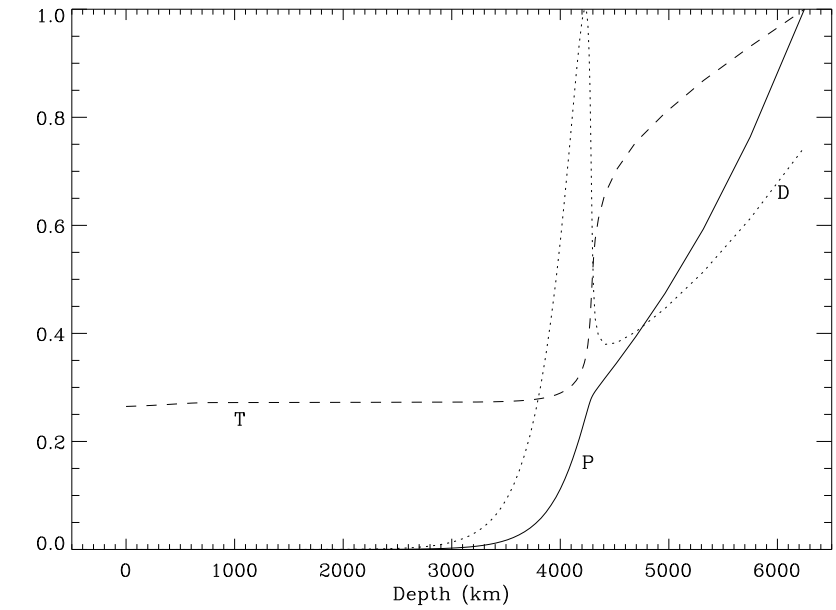

Figure A.4 Pressure, density and temperature in the atmospheric model of α Cir (supplied by F. Kupka, private communication). Each line has been normalized by dividing by the maximum value in the plotted region ($P/76000$, $D/3.4 \times 10^{-8}$, $T/23300$ in *cgs* units). Note that there is a problem with the model, in that the density has a local maximum around 4200 km.

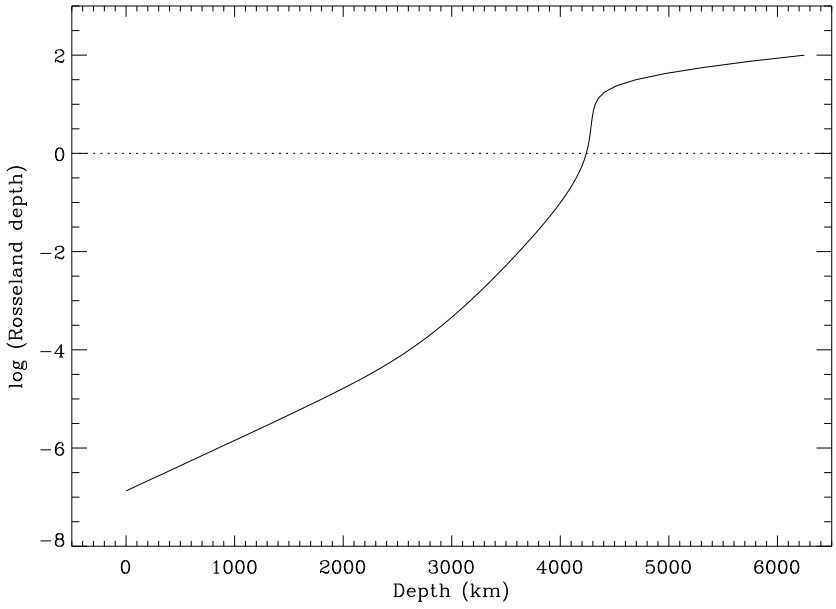

Figure A.5 Rosseland depth as a function of geometric depth in the atmospheric model. The observable region of the atmosphere is at geometric depths of less than 4300 km.

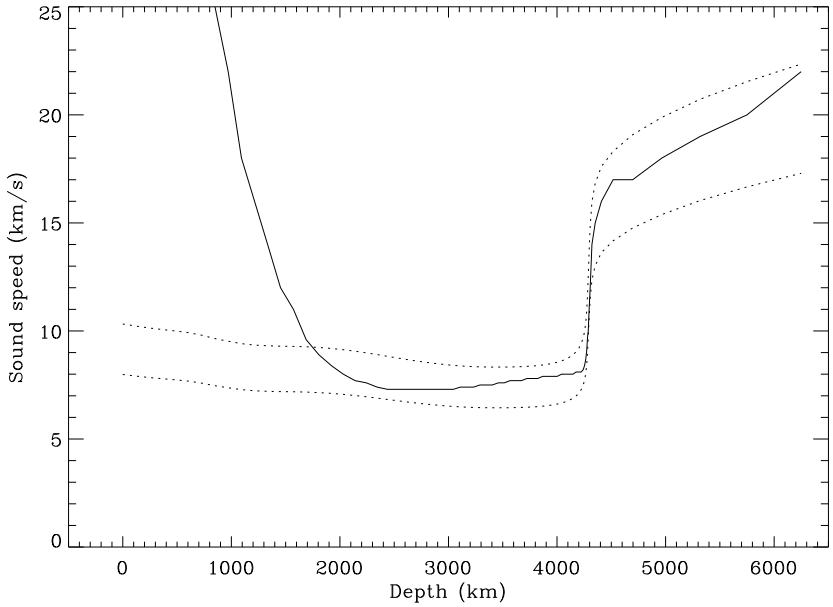

Figure A.6 Sound speed in the atmospheric model. The solid line is the calculated value in Kupka's model, while the dotted lines represent the sound speed from the adiabatic equation $v = \sqrt{\gamma P/D}$ with $\gamma = 1.0$ and 1.67.

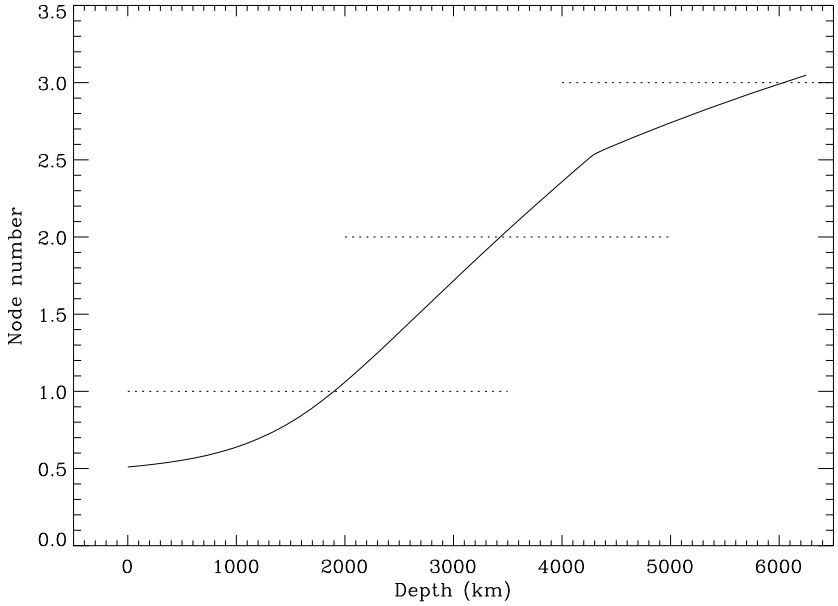

Figure A.7 Nodes in the atmospheric model. Integral numbers represent the node positions, with anti-nodes at the integer$+0.5$ values. The edge of the star is assumed to be an anti-node.

A.3 Variation of the width of Hα in α Cir

At the same time as measuring the bisector of the Hα line (Section 6.2.2), the width of the line at each height was measured. This is a similar analysis to measuring the intensity or equivalent-width changes. Measuring widths is a non-standard analysis but it has the advantage of isolating intensity changes at different heights in the Hα profile and the effect of the bisector variation is naturally removed from the measurements (see Chapters 6–7 for Hα profile variations in α Cir and HR 3831).

Fig. A.8 shows the amplitudes and phases of the principal mode as measured in variations in line width at different heights in the Hα profile (in α Cir). The phases of all the measurements lie between $-10°$ and $30°$, with the exception of section 20 (height 0.80–0.85), which is anomalous in both amplitude and phase. Since our phase reference point (t_0) coincides with maximum light (see Chapter 5), we conclude that the width of the Hα line is pulsating in phase with the luminosity. This is expected, since maximum width of the Hα line indicates maximum temperature in the stellar atmosphere.

The behaviour seen in Fig. A.8 can mostly be explained by changes in intensity in the line profile, which would affect the width by varying degrees, depending on the slope of the line profile. To quantify this, we have simulated a profile variation with an equivalent-width (EW) amplitude of 1000 ppm, where the change in intensity at each wavelength was chosen (somewhat arbitrarily) to be proportional to the depth of the absorption at that wavelength. The profile variation is shown greatly exaggerated in Fig. 6.6. The EW amplitude used in the simulation is same as the value predicted in Section 6.4.3. From the simulation, we measured the width amplitudes and compared it with our data (see dashed line in Fig. A.8). The agreement is good, although there are discrepancies near the core of the line and around a height of 0.75, where the width amplitude drops nearly to zero in the data but not in the simulation. Note this simulation is not based on model atmospheres but is only a description which fits the data reasonably well.

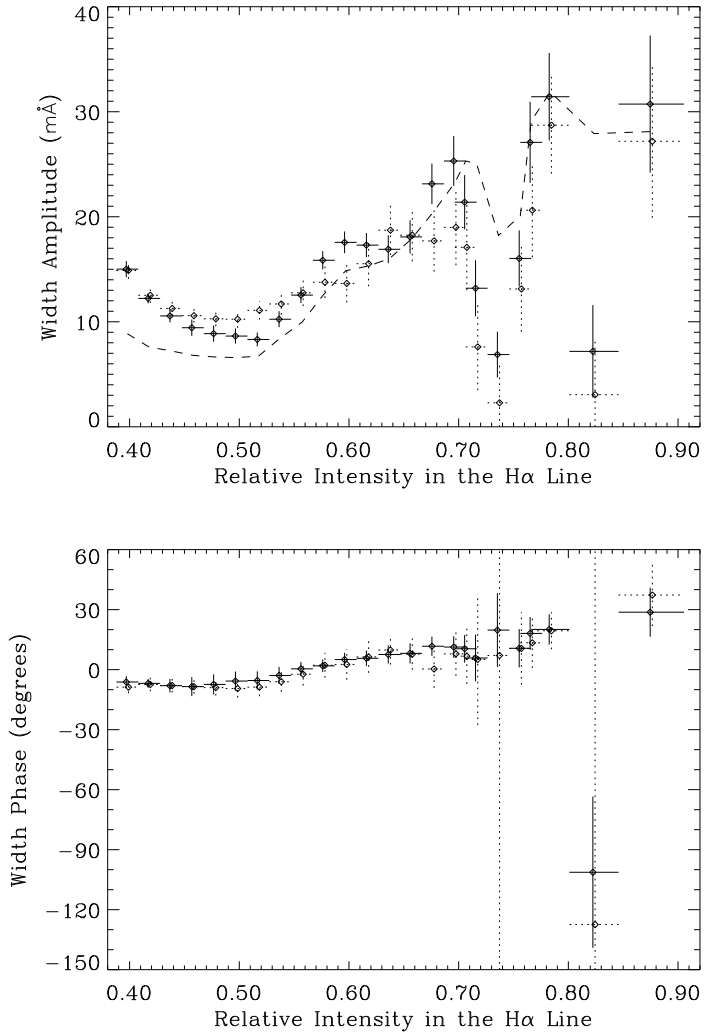

Figure A.8 Amplitudes and phases of the principal pulsation mode for the width at different heights in the Hα line (in α Cir). Points with solid lines represent the Stromlo data and points with dotted lines represent the La Silla data. For each measurement, the vertical line is an error-bar while the horizontal line shows the extent of the section in the Hα line. The dashed line shows the effect on the width amplitude of an oscillation with an EW amplitude of 1000 ppm.

Appendix B

B.1 Spectra of HR 3831

In March 1997, I observed HR 3831 using the coudé spectrograph on the 74-inch Telescope at Mt. Stromlo. During one week, 1400 spectra were obtained with a wavelength range of 6100–7100Å and with a resolution of about 1.5Å (see Chapter 7 for results based on these spectra).

The template spectrum of HR 3831 is shown in Figures B.1 and B.2. The S/N in this spectrum is about 1000 per pixel, though the continuum level is only accurate to about 0.01 between 6250Å and 6900Å and is less accurate outside this region.

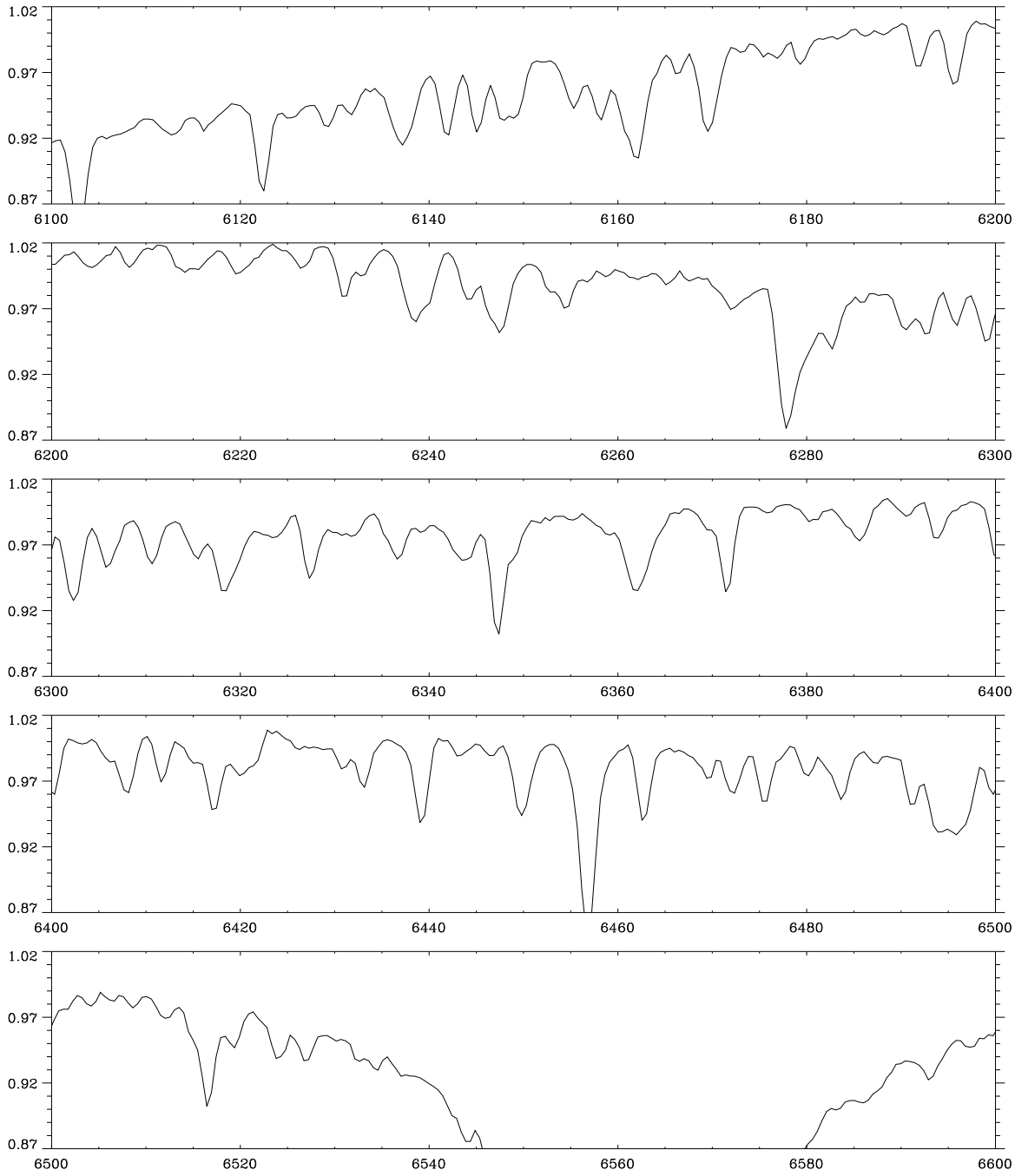

Figure B.1 Spectrum of HR 3831 from 6100 to 6600Å, taken with a medium resolution (~ 1.5Å) spectrograph at Mt. Stromlo. Note that the continuum fit is not accurate below 6250Å.

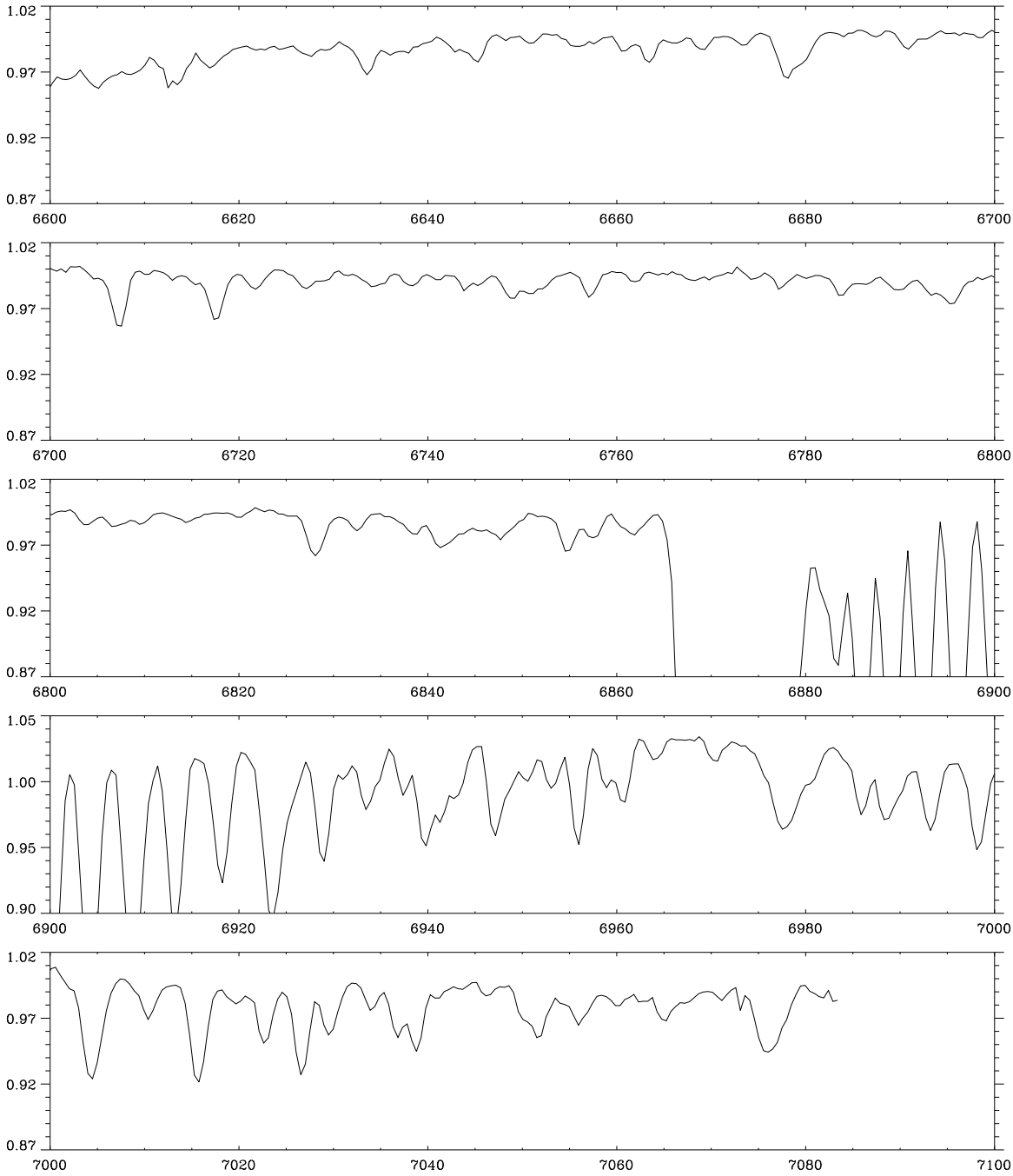

Figure B.2 Spectrum of HR 3831 from 6600 to 7100Å — continuation of Figure B.1. Note that the continuum fit is not accurate between 6900Å and 7000Å. The y-scale for this region is slightly shifted as a result.

B.2 Extra figures of rotational modulation in HR 3831

If oblique pulsator model is correct, HR 3831 pulsates in a dipole mode with an axis that is oblique to the rotation axis. Different aspects of the mode are seen as the star rotates and therefore, the measured amplitude and phase of the pulsation modulates with the rotation (see Chapter 7 for details).

Several observables were defined from the spectra of HR 3831. For each observable, a time series of measurements was analysed to determine the amplitudes and phases of the frequency triplet. Additionally, the data for each observable were divided into 20 separate time periods, and the amplitude and phase of the pulsation were measured for each period (see Section 7.3 for details).

Plots of the modulation in the amplitude and phase of various observables are shown in Figures B.3–B.18, 7.4, 7.5 and 7.8. The figures show the amplitude and phase of the central frequency as a function of rotation phase. The squares represent the data divided into 20 separate time periods between 0.5 and 3.6 hours long. The vertical lines are error bars, while the horizontal lines show the length of the time period. The dashed line represents a fit based on the measurement of the frequency triplet from the complete time series, and the dotted line represents a fit which is scaled and phase shifted from the photometric frequency triplet (Table 7.2). Note that the data are plotted twice.

Figs. B.3–B.12, 7.5 and 7.8 show observables based on the cross-correlation measurements of various wavelength bands. Figs. B.13–B.16 show bisector velocity and width measurements of the Hα line. Figs. B.17–B.18 and 7.4 show direct intensity measurements of the Hα core and an R_{cw} intensity ratio measurement.

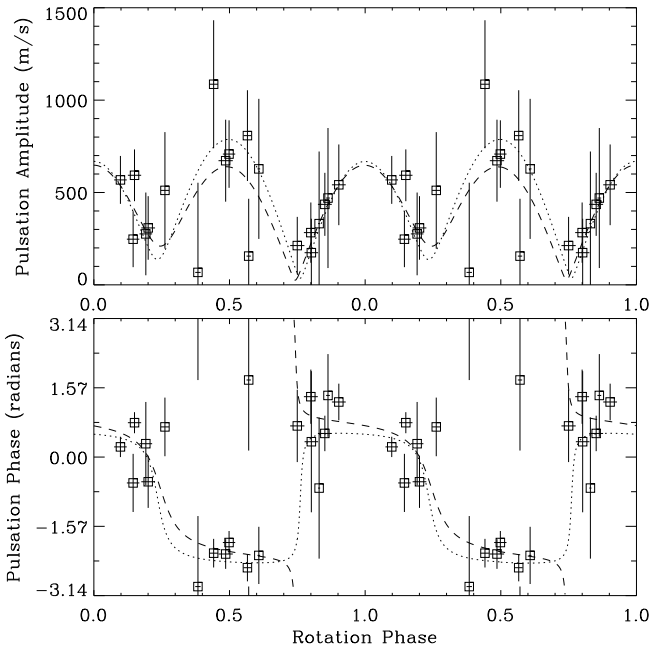

Figure B.3 Velocity amplitude and phase of band no. 13

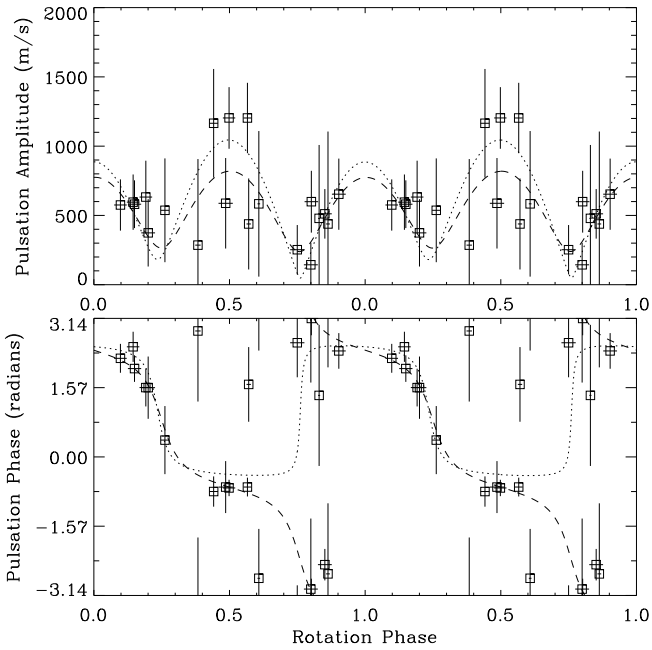

Figure B.4 Velocity amplitude and phase of band no. 14

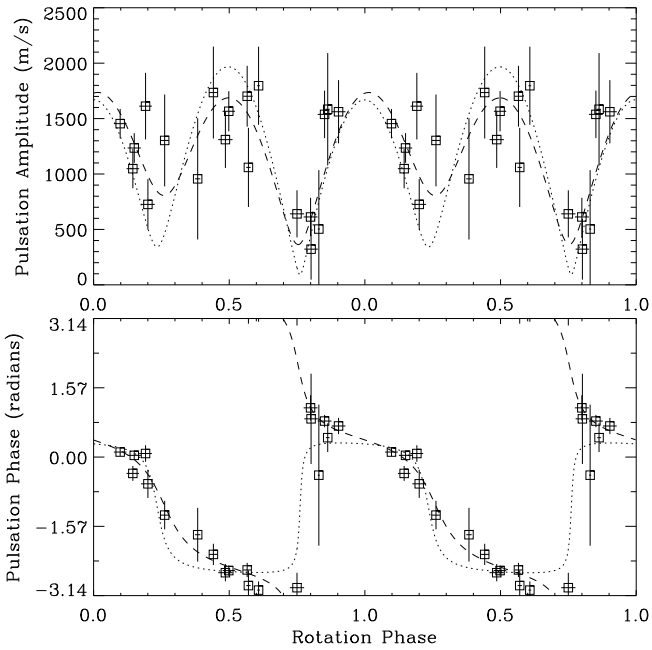

Figure B.5 Velocity amplitude and phase of band no. 33

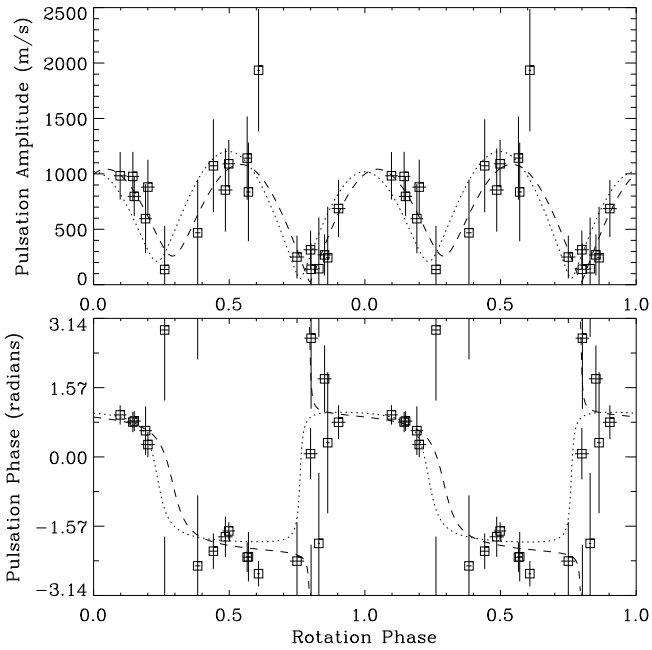

Figure B.6 Velocity amplitude and phase of band no. 42

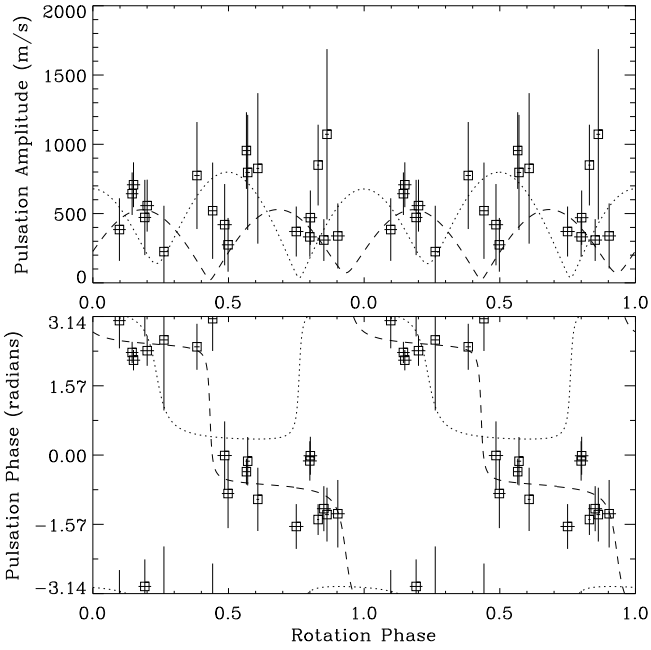

Figure B.7 Velocity amplitude and phase of band no. 48

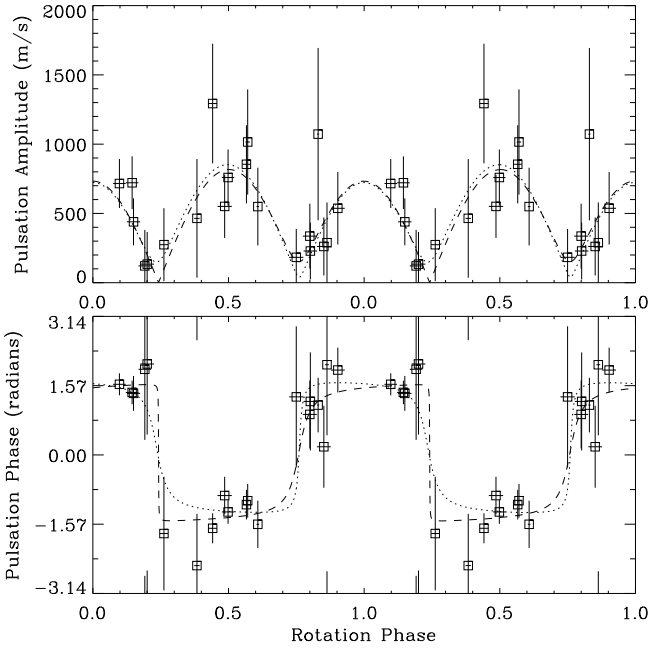

Figure B.8 Velocity amplitude and phase of band no. 54

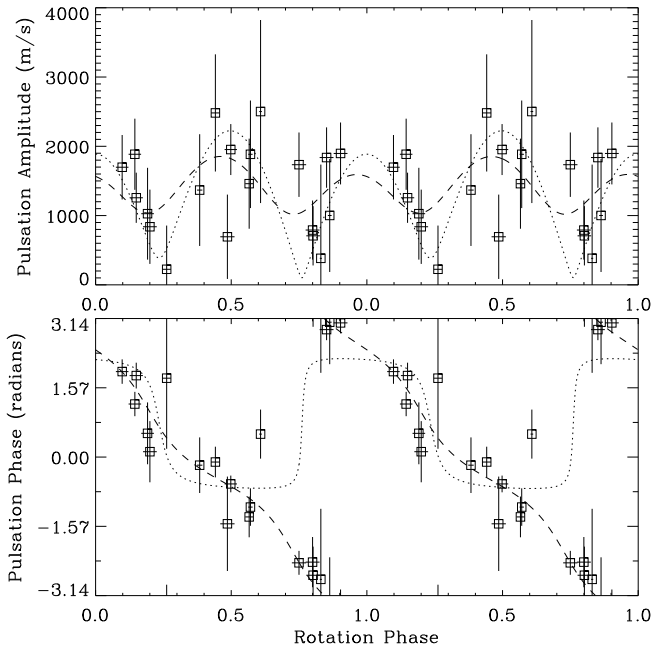

Figure B.9 Velocity amplitude and phase of band no. 58

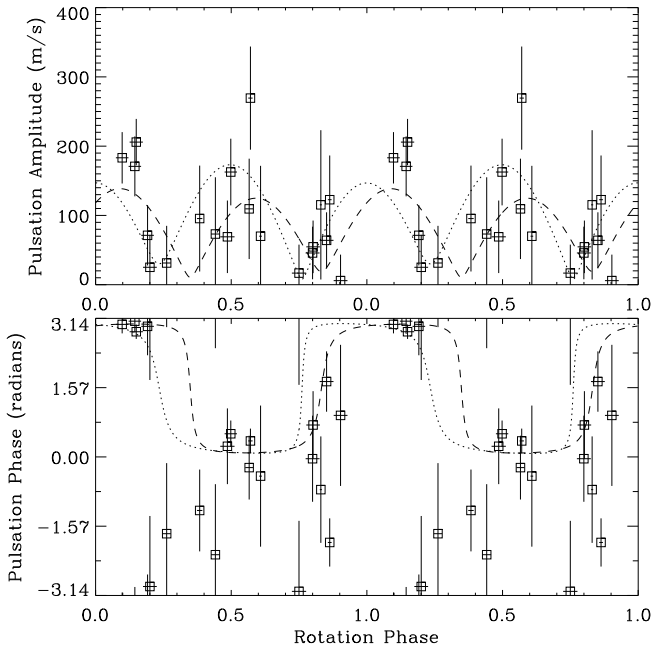

Figure B.10 Velocity amplitude and phase of band no. 81

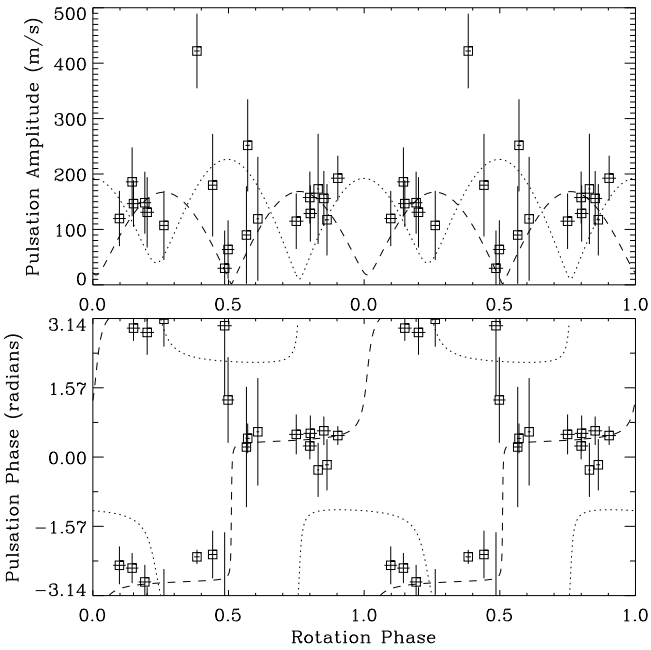

Figure B.11 Velocity amplitude and phase of band no. 82

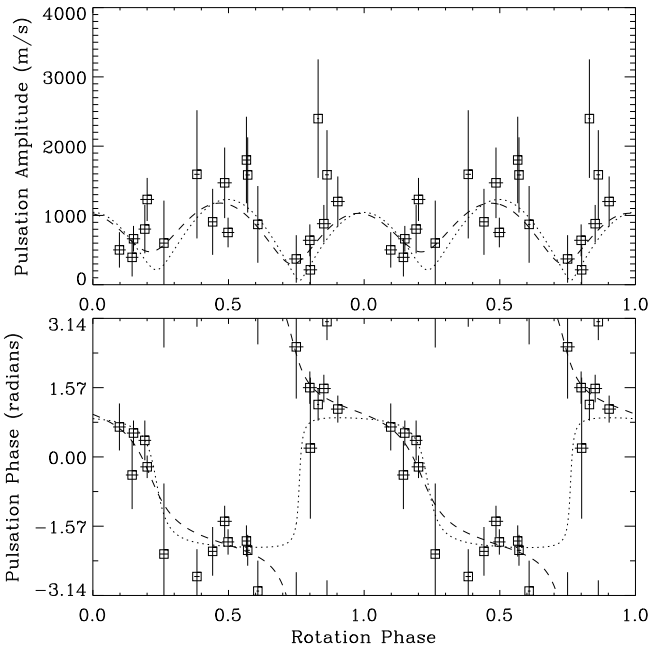

Figure B.12 Velocity amplitude and phase of band no. 90

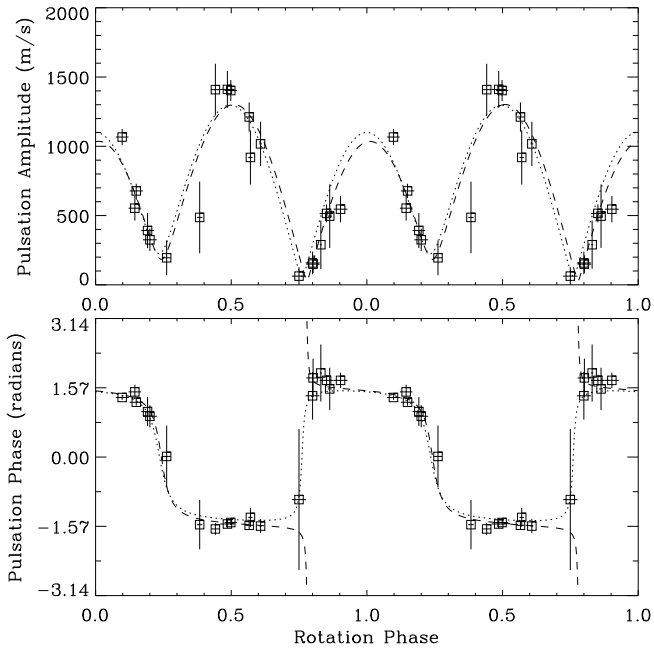

Figure B.13 Velocity amplitude and phase of the Hα bisector at height 0.40

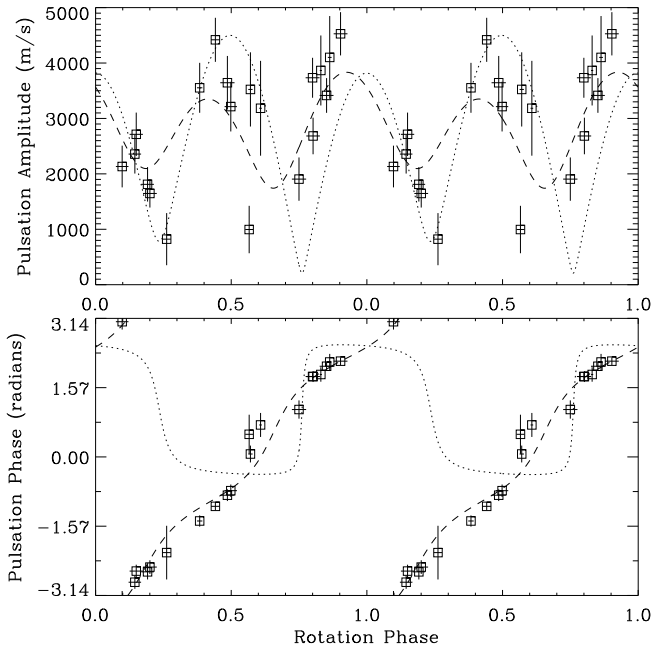

Figure B.14 Width amplitude and phase of the Hα line at height 0.36

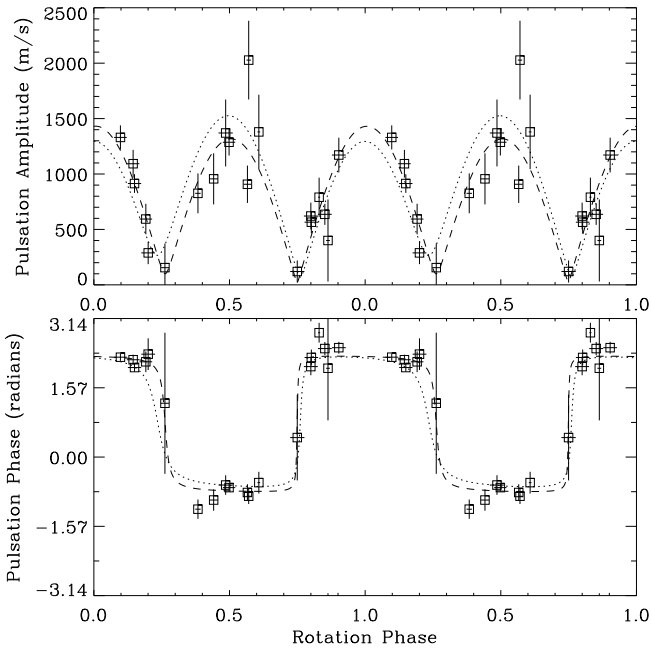

Figure B.15 Width amplitude and phase of the Hα line at height 0.42

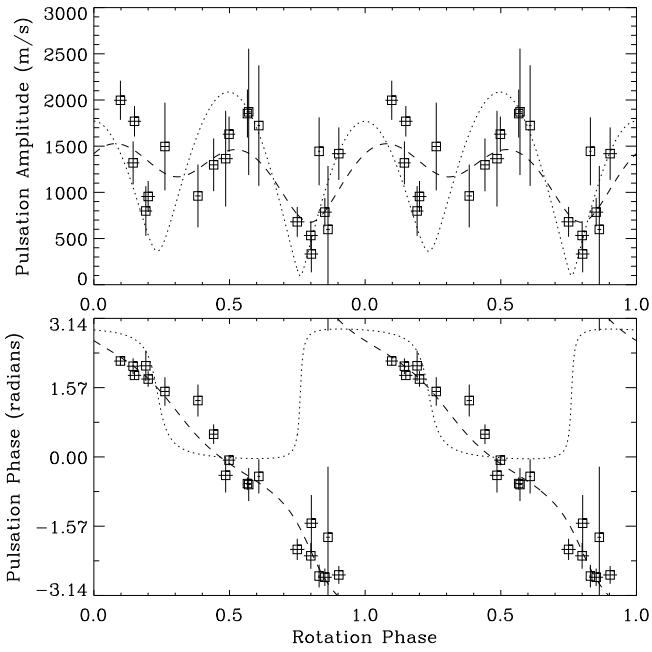

Figure B.16 Width amplitude and phase of the Hα line at height 0.53

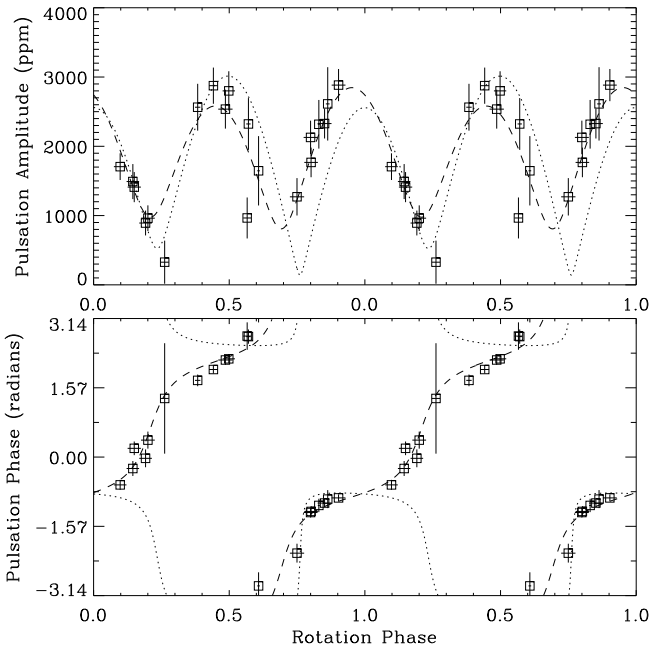

Figure B.17 Intensity amplitude and phase of the Hα core, using a filter with FWHM$\sim$1.0Å

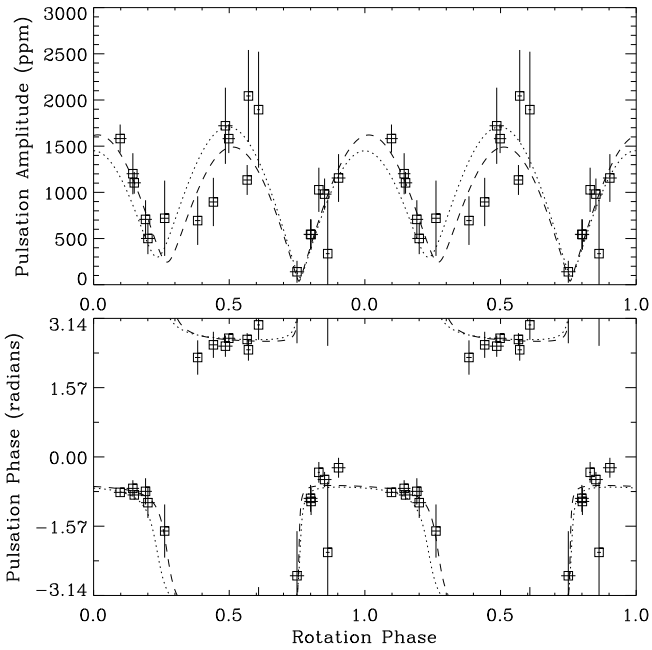

Figure B.18 Intensity amplitude and phase of the Hα core, using a filter with FWHM$\sim$5.9Å

References

Albrow M. D., Cottrell P. L., 1994, Line profiles of Cepheid variables – projection factors and metallic line asymmetries, in **MNRAS, 267,** p. 548–556.

Audard N., Kupka F., Morel P., Provost J., Weiss W. W., 1998, The acoustic cut-off frequency of roAp stars, in **A&A, 335,** p. 954–958.

Baldry I. K., Bock D. C., Bureau M. G. et al., 1996, Winter ASA, in **Publ. Astron. Soc. Australia, 13,** p. 309.

Baldry I. K., Taylor M. M., Bedding T. R., Booth A. J., 1997, Hα profile variations in the long-period Cepheid ℓ Car, in **MNRAS, 289,** p. 979–985.

Baldry I. K., Bedding T. R., Viskum M., Kjeldsen H., Frandsen S., 1998a, Bisector velocities of Hα in the roAp star α Cir, in **Proc. IAU Symp. 185, New Eyes to See Inside the Sun and Stars,** ed. by Deubner F.-L., Christensen-Dalsgaard J., Kurtz D. W., publ. by Kluwer, Dordrecht, p. 309–310.

Baldry I. K., Bedding T. R., Viskum M., Kjeldsen H., Frandsen S., 1998b, Spectroscopy of the roAp star α Cir – I, in **MNRAS, 295,** p. 33–42.

Baldry I. K., Kurtz D. W., Bedding T. R., 1998c, Confirmation of the oblique pulsator model for the rapidly oscillating Ap star HR 3831, in **MNRAS, 300,** p. L39–L42.

Baldry I. K., Viskum M., Bedding T. R., Kjeldsen H., Frandsen S., 1999, Spectroscopy of the roAp star α Cir – II, in **MNRAS, 302,** p. 381–390.

Baldry I. K., 1998, The roAp star α Cir: a target for MONS?, in **Proc. First MONS Workshop, Science with a Small Space Telescope,** ed. by Kjeldsen H., Bedding T. R., publ. by Univ. Aarhus, p. 135–140.

Balona L. A., Krisciunas K., Cousins A. W. J., 1994, γ Doradus – evidence for a new class of pulsating star, in **MNRAS, 270,** p. 905–913.

Barrell S. L., 1978, Hα emission in beat Cepheids, in **ApJ, 226,** p. L141–L143.

Barrell S. L., 1981, Beat Cepheid studies – I, in **MNRAS, 196,** p. 357–369.

Becker S. A., 1998, The variable star menagerie, in **ASP Conf. Ser. Vol. 135, A Half Century of Stellar Pulsation Interpretations,** ed. by Bradley P. A., Guzik J. A., publ. by Astron. Soc. Pacific, San Francisco, p. 12–21.

Bedding T. R., Kjeldsen H., Reetz J., Barbuy B., 1996, Measuring stellar oscillations using equivalent widths of absorption lines, in **MNRAS, 280,** p. 1155–1161.

Bedding T. R., Zijlstra A. A., Jones A., Foster G., 1998, Mode switching in the nearby Mira-like variable R Doradus, in **MNRAS, 301,** p. 1073–1082.

Bell R. A., Rodgers A. W., 1967, The atmosphere of β Dor, in **MNRAS, 135,** p. 121–129.

Belmonte J. A., Bell C. R., Leeper M., Palle P. L., Pietraszewski K. A. R. B., Renton R. E., Cortes T. R., 1989, Search for radial velocity variations in rapidly oscillating Ap stars, in **A&A, 221,** p. 41–48.

Böhm-Vitense E., Love S. G., 1994, Emission lines in the long-period Cepheid ℓ Car, in **ApJ, 420,** p. 401–414.

Booth A. J., Davis J., Shobbrook R. R., 1995, SUSI's potential for Cepheid studies, in **ASP Conf. Ser. Vol. 83, Astrophysical Applications of Stellar Pulsation,** ed. by Stobie R. S., Whitelock P. A., publ. by Astron. Soc. Pacific, San Francisco, p. 281–282.

Bradley P. A., Guzik J. A., editors, 1998, **ASP Conf. Ser. Vol. 135, A Half Century of Stellar Pulsation Interpretations,** publ. by Astron. Soc. Pacific, San Francisco.

Bradley P. A., 1995, White dwarf data tables, in **Baltic Astron., 4,** p. 536–546.

Breger M., 1979, Delta Scuti and related stars, in **PASP, 91,** p. 5–26.

Brown T. M., Gilliland R. L., 1994, Asteroseismology, in **ARA&A, 32,** p. 37–82.

Chagnon F., Matthews J. M., 1998, Dynamics of pulsating Ap stars: measuring velocity variations at the few m/s level, in **JRASC, 92,** p. 27–28.

Christensen-Dalsgaard J., 1988, A Hertzsprung-Russell diagram for stellar oscillations, in **Proc. IAU Symp. 123, Advances in Helio- and Asteroseismology,** ed. by Christensen-Dalsgaard J., Frandsen S., publ. by D. Reidel Publ. Co., Dordrecht, p. 295–298.

Christensen-Dalsgaard J., 1998, **Lecture Notes on Stellar Oscillations,** publ. by Univ. Aarhus, URL `http://www.obs.aau.dk/~jcd/oscilnotes/`.

Cox J. P., 1980, **Theory of Stellar Pulsation,** publ. by Princeton Univ., New Jersey.

Deasy H. P., 1988, Observational evidence for mass loss from classical Cepheids, in **MNRAS, 231,** p. 673–694.

Deubner F.-L., Waldschik T., Steffens S., 1996, Dynamics of the solar atmosphere – VI. Resonant oscillations of an atmospheric cavity, in **A&A, 307,** p. 936–946.

Deubner F.-L., Christensen-Dalsgaard J., Kurtz D., editors, 1998, **Proc. IAU Symp. 185, New Eyes to See Inside the Sun and Stars,** publ. by Kluwer, Dordrecht.

Dziembowski W. A., Goode P. R., 1985, Frequency splitting in Ap stars, in **ApJ, 296,** p. L27–L30.

Dziembowski W. A., Goode P. R., 1986, Asteroseismology for certain Ap stars, in **Seismology of the Sun and the Distant Stars,** ed. by Gough D. O., publ. by D. Reidel Publ. Co., Dordrecht, p. 441–451.

Dziembowski W. A., Goode P. R., 1996, Magnetic effects on oscillations in roAp stars, in **ApJ, 458,** p. 338–346.

ESA, 1997, **The Hipparcos and Tycho Catalogues, ESA SP-1200,** publ. by European Space Agency Publ. Division, c/o ESTEC, Noordwijk,
URL `http://astro.estec.esa.nl/Hipparcos/catalog.html`.

Feast M. W., 1992, Stars, pulsating, overview, in **The Astronomy and Astrophysics Encyclopedia,** ed. by Marin S. P., publ. by Van Nostrand Reinhold, New York, p. 772–774.

Fokin A. B., Gillet D., 1994, The shock wave propagation effects in BL Herculis – II, in **A&A, 290,** p. 875–884.

Fontaine G., Charpinet S., Brassard P., Chayer P., Rogers F. J., Iglesias C. A., Dorman B., 1998, EC14026 stars – theoretical considerations, in **Proc. IAU Symp. 185, New Eyes to See Inside the Sun and Stars,** ed. by Deubner F.-L., Christensen-Dalsgaard J., Kurtz D. W., publ. by Kluwer, Dordrecht, p. 367–374.

Gautschy A., Saio H., 1995, Stellar pulsations across the HR diagram: part 1, in **ARA&A, 33,** p. 75–114.

Gautschy A., Saio H., 1996, Stellar pulsations across the HR diagram: part 2, in **ARA&A, 34,** p. 551–606.

Gautschy A., Saio H., Harzenmoser H., 1998, How to drive roAp stars, in **MNRAS, 301,** p. 31–41.

Gillet D., Burki G., Chatel A., Duquennoy A., Lebre A., 1994, The shock wave propagation effects in BL Herculis – I, in **A&A, 286,** p. 508–514.

Gilliland R. L., Brown T. M., Kjeldsen H. et al., 1993, A search for solar-like oscillations in the stars of M67 with CCD ensemble photometry, in **AJ, 106,** p. 2441–2476.

Grenfell T. C., Wallerstein G., 1969, Atmospheric depth effects during rising light of the 45-day Cepheid SV Vul, in **PASP, 81,** p. 732–740.

Hatzes A. P., Kürster M., 1994, A search for rapid radial velocity variations in α Circini, in **A&A, 285,** p. 454–458.

Hatzes A. P., 1996, Simulations of stellar radial velocity and spectral line bisector variations, in **PASP, 108,** p. 839–843.

Jacobsen T. S., Wallerstein G., 1982, The radial velocity of the ten-day Cepheid ζ Geminorum, in **PASP, 94,** p. 471–474.

Kanaan A., Hatzes A. P., 1998, Pulsations and radial velocity variations in pulsating Ap stars – I. Analysis of γ Equulei, in **ApJ, 503,** p. 848–856.

Keller C. U., Harvey J. W., Barden S. C., Giampapa M. S., Hill F., Pilachowski C. A., 1998, Asteroseismology from equivalent widths: a test of the sun, in **Proc. IAU Symp. 185, New Eyes to See Inside the Sun and Stars,** ed. by Deubner F.-L., Christensen-Dalsgaard J., Kurtz D. W., publ. by Kluwer, Dordrecht, p. 375–378.

Kholopov P. N., Samus N. N., Frolov M. S. et al., 1998, **The Combined Table of General Catalogue of Variable Stars Volumes I–III,** publ. by Sternberg Astron. Inst., Moscow,
URL `http://www.sai.msu.su/groups/cluster/gcvs/gcvs/`.

Kjeldsen H., Bedding T. R., 1995, Amplitudes of stellar oscillations, in **A&A, 293,** p. 87–106.

Kjeldsen H., Bedding T. R., Viskum M., Frandsen S., 1995, Solarlike oscillations in η Boo, in **AJ, 109,** p. 1313–1319.

Kupka F., Ryabchikova T. A., Weiss W. W., Kuschnig R., Rogl J., Mathys G., 1996, Abundance analysis of roAp stars – I. α Circini, in **A&A, 308,** p. 886–894.

Kurtz D. W., Martinez P., 1993, Determination of luminosity, atmospheric structure and magnetic geometry from studies of the pulsation in roAp stars, in **ASP Conf. Ser. Vol. 44, Peculiar versus Normal Phenomena in A-type and Related Stars,** ed. by Dworetsky M. M., Castelli F., Faraggiana R., publ. by Astron. Soc. Pacific, San Francisco, p. 561–576.

Kurtz D. W., Matthews J. M., Martinez P. et al., 1989, The high-overtone p-mode spectrum of the rapidly oscillating Ap star HR 1217, in **MNRAS, 240,** p. 881–915.

Kurtz D. W., Shibahashi H., Goode P. R., 1990, A frequency analysis with 20–350 pHz accuracy of five years of observations of the non-linear dipole oscillation in the rapidly oscillating Ap star HR 3831, in **MNRAS, 247,** p. 558–572.

Kurtz D. W., Kanaan A., Martinez P., Tripe P., 1992, A refinement of the rotation period of the roAp star HR 3831 and the discovery of a significant phase lag between the times of pulsation and magnetic extrema and the time of mean-light extremum, in **MNRAS, 255,** p. 289–294.

Kurtz D. W., Kanaan A., Martinez P., 1993, Phase instability and non-linearity in the distorted dipole pulsation mode of the rapidly oscillating Ap star HR 3831, in **MNRAS, 260,** p. 343–364.

Kurtz D. W., Martinez P., van Wyk F., Marang F., Roberts G., 1994a, Cyclic frequency variability in the rapidly oscillating Ap star HR 3831, in **MNRAS, 268,** p. 641–653.

Kurtz D. W., Sullivan D. J., Martinez P., Tripe P., 1994b, The pure dipole pulsation mode of the rapidly oscillating Ap star α Circini, in **MNRAS, 270,** p. 674–686, abbrev. KSMT.

Kurtz D. W., van Wyk F., Roberts G., Marang F., Handler G., Medupe R., Kilkenny D., 1997, Frequency variability in the rapidly oscillating Ap star HR 3831, in **MNRAS, 287,** p. 69–78.

Kurtz D. W., 1982, Rapidly oscillating Ap stars, in **MNRAS, 200,** p. 807–859.

Kurtz D. W., 1990, Rapidly oscillating Ap stars, in **ARA&A, 28,** p. 607–655.

Kurucz R. L., 1979, Model atmospheres for G, F, A, B, and O stars, in **ApJS, 40,** p. 1–31.

Ledoux P., 1951, The non-radial oscillations of gaseous stars and the problem of β CMa, in **ApJ, 114,** p. 373–384.

Libbrecht K. G., 1988, Radial velocity observations reveal multimode oscillations in γ Equulei, in **ApJ, 330,** p. L51–L53.

Mallik S. V., 1993, CCD observations of the Hα line in late G and K supergiants, in **ApJ, 402,** p. 303–310.

Marin S. P., editor, 1992, **The Astronomy and Astrophysics Encyclopedia,** publ. by Van Nostrand Reinhold, New York.

Martinez P., Kurtz D. W., 1995a, Observations of pulsating Ap stars in South Africa, in **Ap&SS, 230,** p. 29–39.

Martinez P., Kurtz D. W., 1995b, Rapid pulsations in Ap stars, in **ASP Conf. Ser. Vol. 83, Astrophysical Applications of Stellar Pulsation,** ed. by Stobie R. S., Whitelock P. A., publ. by Astron. Soc. Pacific, San Francisco, p. 58–69.

Martinez P., Weiss W. W., Nelson M. J. et al., 1996, The p-mode spectrum of γ Equ, in **MNRAS, 282,** p. 243–251.

Mathys G., Kharchenko N., Hubrig S., 1996, A kinematical study of rapidly oscillating Ap stars, in **A&A, 311,** p. 901–910.

Mathys G., 1985, The influence of surface inhomogeneities on the rapid light variations of Ap stars, in **A&A, 151,** p. 315–321.

Matthews J. M., Wehlau W. H., Walker G. A. H., Yang S., 1988, Detection of radial velocity variations in the rapidly oscillating Ap star HR 1217, in **ApJ, 324,** p. 1099–1105.

Matthews J. M., Walker G. A. H., Wehlau W. H., 1990, Rapid infrared photometry of pulsating Ap stars: a measurement of stellar limb darkening, in **ApJ, 365,** p. L81–L84.

Matthews J. M., Wehlau W. H., Rice J., Walker G. A. H., 1996, Opening a new window on Ap star atmospheres, in **ApJ, 459,** p. 278–287.

Matthews J. M., 1991, Stellar seismology and the pulsating Ap stars, in **PASP, 103,** p. 5–19.

Matthews J. M., 1997, Probing the interior of roAp stars, in **Proc. IAU Symp. 181, Sounding Solar and Stellar Interiors,** ed. by Provost J., Schmider F. X., publ. by Kluwer, Dordrecht, p. 387–394.

Matthews J. M., 1998, Replacing colour blindness with depth perception, in **Proc. IAU Symp. 185, New Eyes to See Inside the Sun and Stars,** ed. by Deubner F.-L., Christensen-Dalsgaard J., Kurtz D. W., publ. by Kluwer, Dordrecht, p. 269–276.

Medupe R., Kurtz D. W., 1998, Determining temperature amplitude as a function of depth in the atmospheres of rapidly oscillating Ap stars, in **MNRAS, 299,** p. 371–378.

Medupe R., Kurtz D. W., Christensen-Dalsgaard J., 1998, The problem of mode identification in roAp stars, in **ASP Conf. Ser. Vol. 135, A Half Century of Stellar Pulsation Interpretations,** ed. by Bradley P. A., Guzik J. A., publ. by Astron. Soc. Pacific, San Francisco, p. 197–198.

Moore C. E., Minnaert M. G. J., Houtgast J., 1966, **The Solar Spectrum 2935Å to 8770Å,** publ. by U. S. Government Printing Office, Washington.

Moskalik P., 1995, New results on pulsating OB stars, in **ASP Conf. Ser. Vol. 83, Astrophysical Applications of Stellar Pulsation,** ed. by Stobie R. S., Whitelock P. A., publ. by Astron. Soc. Pacific, San Francisco, p. 44–55.

Musielok B., Madej J., 1988, Variability of Balmer lines in Ap stars, in **A&A, 202,** p. 143–152.

Perryman M. A. C., Lindegren L., Kovalevsky J. et al., 1997, The Hipparcos Catalogue, in **A&A, 323,** p. L49–L52.

Provost J., Schmider F. X., editors, 1997, **Proc. IAU Symp. 181, Sounding Solar and Stellar Interiors,** publ. by Kluwer, Dordrecht.

Rice J. B., Wehlau W. H., 1991, The range of abundances of iron, chromium and silicon over the surfaces of the CP stars ϵ Ursae Majoris and θ Aurigae, in **A&A, 246,** p. 195–198.

Rodgers A. W., Bell R. A., 1968, The atmosphere of the long period Cepheid ℓ Car, in **MNRAS, 138,** p. 23–50.

Ronan R. S., Harvey J. W., Duvall T. L. J., 1991, Wavelength variation of p-mode intensity fluctuations, in **ApJ, 369,** p. 549–556.

Sasselov D. D., Lester J. B., 1994, The chromospheric structure of classical Cepheids, in **ApJ, 423,** p. 795–805.

Schmidt-Kaler T., 1982, Physical parameters of the stars: effective temperatures, bolometric corrections and luminosities, in **Landolt-Börnstein, Group VI, Vol. 2b,** ed. by Schaifers K., Voigt H. H., publ. by Springer-Verlag, Berlin, p. 451–456.

Schmidt E. G., 1970, Hα as a temperature indicator in Cepheids, in **ApJ, 162,** p. 871–881.

Schneider H., Weiss W. W., 1989, Pulsating CP2 stars – I. α Circini, in **A&A, 210,** p. 147–154.

Shibahashi H., Takata M., 1993, Theory for the distorted dipole modes of the rapidly oscillating Ap stars, in **PASJ, 45,** p. 617–641.

Shibahashi H., 1991, Theoretical aspects of asteroseismology of the rapidly oscillating Ap stars, in **Lecture Notes in Physics 388, Challenges to Theories of the Structure of Moderate-Mass Stars,** ed. by Gough D., Toomre J., publ. by Springer-Verlag, Berlin, p. 393–410.

Shobbrook R. R., 1992, UBV(RI)$_c$ observations for 13 bright Cepheids, in **MNRAS, 255,** p. 486–494.

Shortridge K., 1993, The evolution of the Figaro data reduction system, in **ASP Conf. Ser. Vol. 52, Astronomical Data Analysis Software and Systems II,** ed. by Hanisch R. J., Brissenden R. J., Barnes J., publ. by Astron. Soc. Pacific, San Francisco, p. 219–223.

Sowell J. R., 1990, A survey of Balmer-line profiles and IRAS fluxes in forty yellow supergiants, in **AJ, 100,** p. 834–848.

Stobie R. S., Whitelock P. A., editors, 1995, **ASP Conf. Ser. Vol. 83, Astrophysical Applications of Stellar Pulsation,** publ. by Astron. Soc. Pacific, San Francisco.

Sullivan D. J., 1998, Frequency stability of the DAV white dwarf L19-2, in **ASP Conf. Ser. Vol. 135, A Half Century of Stellar Pulsation Interpretations,** ed. by Bradley P. A., Guzik J. A., publ. by Astron. Soc. Pacific, San Francisco, p. 62–66.

Takata M., Shibahashi H., 1994, Selection rules for perturbations to the eigenfunctions of the pulsations of stars due to the rotation and magnetic field, in **PASJ, 46,** p. 301–314.

Takata M., Shibahashi H., 1995, Effects of the quadrupole component of magnetic fields on the rapid oscillations of Ap stars, in **PASJ, 47,** p. 219–231.

Taylor M. M., Booth A. J., 1998, The bright southern Cepheid β Doradus, in **MNRAS, 298,** p. 594–600.

Taylor M. M., Albrow M. D., Booth A. J., Cottrell P. L., 1997, The bright southern Cepheid ℓ Car, in **MNRAS, 292,** p. 662–672.

Tinney C., 1996, **The AAO CCD Imaging Manual,** publ. by Anglo-Australian Obser., URL `http://www.aao.gov.au/local/www/cgt/ccdimguide/`.

Unno W., Osaki Y., Ando H., Saio H., Shibahashi H., 1989, **Nonradial Oscillations of Stars,** publ. by Univ. Tokyo Press.

Viskum M., Baldry I. K., Kjeldsen H., Frandsen S., Bedding T. R., 1998a, New radial velocity curves of roAp and δ Scuti stars, in **Poster Proc. IAU Symp. 181, Sounding Solar and Stellar Interiors,** ed. by Provost J., Schmider F. X., publ. by Univ. Nice, p. 285–287.

Viskum M., Dall T., Bruntt H., Frandsen S., Kjeldsen H., Baldry I. K., Bedding T. R., 1998b, New techniques for oscillation mode identification in the δ Scuti star FG Virginis, in **ASP Conf. Ser. Vol. 135, A Half Century of Stellar Pulsation Interpretations,** ed. by Bradley P. A., Guzik J. A., publ. by Astron. Soc. Pacific, San Francisco, p. 465–469.

Viskum M., Kjeldsen H., Bedding T. R., Dall T. H., Baldry I. K., Bruntt H., Frandsen S., 1998c, Oscillation mode identifications and models for the δ Scuti star FG Virginis, in **A&A, 335,** p. 549–560.

Waelkens C., 1996, The slowly pulsating B stars HD 34798 and HD 45284, in **A&A, 311,** p. 873–878.

Wallerstein G., Jacobsen T. S., Cottrell P. L., Clark M., Albrow M., 1992, Metallic-line and Hα radial velocities of seven southern Cepheids, in **MNRAS, 259,** p. 474–488.

Wallerstein G., 1972, Motions in the outer layers of the 27-day Cepheid T Mon, in **PASP, 84,** p. 656–663.

Wallerstein G., 1979, The behavior of Hα in δ Cephei, in **PASP, 91,** p. 772–774.

Wallerstein G., 1983, The behavior of Hα in the 16-day Cepheid X Cygni, in **PASP, 95,** p. 422–426.

Weiss W. W., Kuschnig R., Schneider H., Bouchet P., 1991, Pulsation of α Circini: contemporaneous photometry in the infrared and visible, in **A&A, 245,** p. 145–149.

Whitelock P. A., 1990, Pulsating red variables, in **ASP Conf. Ser. Vol. 11, Confrontation Between Stellar Pulsation and Evolution,** ed. by Cacciari C., Clementini G., publ. by Astron. Soc. Pacific, San Francisco, p. 365–378.

Wood P. R., 1995, Mira variables: theory versus observation, in **ASP Conf. Ser. Vol. 83, Astrophysical Applications of Stellar Pulsation,** ed. by Stobie R. S., Whitelock P. A., publ. by Astron. Soc. Pacific, San Francisco, p. 127–138.

Abbreviations for journals

A&A	Astronomy and Astrophysics
A&AS	Astronomy and Astrophysics Supplement Series
AJ	Astronomical Journal
ApJ	Astrophysical Journal
ApJS	Astrophysical Journal Supplement
Ap&SS	Astrophysics and Space Science
ARA&A	Annual Review of Astronomy and Astrophysics
JRASC	Journal of the Royal Astronomical Society of Canada
MNRAS	Monthly Notices of the Royal Astronomical Society
PASJ	Publications of the Astronomical Society of Japan
PASP	Publications of the Astronomical Society of the Pacific